THE UNIVERSITY *of* EDINBURGH

This thesis has been submitted in fulfilment of the requirements for a postgraduate degree (e.g. PhD, MPhil, DClinPsychol) at the University of Edinburgh. Please note the following terms and conditions of use:

This work is protected by copyright and other intellectual property rights, which are retained by the thesis author, unless otherwise stated.
A copy can be downloaded for personal non-commercial research or study, without prior permission or charge.
This thesis cannot be reproduced or quoted extensively from without first obtaining permission in writing from the author.
The content must not be changed in any way or sold commercially in any format or medium without the formal permission of the author.
When referring to this work, full bibliographic details including the author, title, awarding institution and date of the thesis must be given.

A Fast Timing Hodoscope for CLAS12 and the First Measurement of the $\gamma p \to \omega\pi\pi p$ Decay Channel

Simon Matthew Hughes

Doctor of Philosophy
The University of Edinburgh
May 2017

Declaration

I declare that this thesis was composed by myself, that the work contained herein is my own except where explicitly stated otherwise in the text, and that this work has not been submitted for any other degree or professional qualification except as specified.

(*Simon Matthew Hughes, May 2017*)

Acknowledgements

First of all, I would like to thank my primary supervisor, Prof. D. P. Watts. You are the person that truly inspired me to pursue a PhD, after our research together into Compton Imaging. Your support, encouragement and insight have been invaluable. It has been a pleasure to learn from you as a student, and to work with you as a colleague.

Next, to my second supervisor Dr. L. Zana. I would like to thank you for your support and seemingly endless patience in helping me with computational problems over the years. You have also provided me with many wise thoughts and perspectives, both in physics and in dealing with Chinese in-laws!

Both of my supervisors have supported me through some very difficult periods during my PhD and for this I cannot thank them enough.

During this PhD, I have been lucky enough to work in several international collaborations, having the opportunity to travel, and to discuss physics with many inspiring people who are passionate about the field. In particular I'd like to thank Dr. D. Glazier and Prof. M. Battaglieri for their insights and enthusiasm for the subject; I have learnt so much from both of them.

Aside from those I have worked with during this PhD, I would like to thank my parents for their support and belief in me throughout this process. They are also responsible for diligently proofreading this thesis, despite not having a background in physics, sticking resolutely to the structure of the prose.

Finally, I'd like to thank my wonderful wife, Stella, for her constant, unwavering support over the last four years. You have brought fresh perspectives to many of the problems I have faced and your infectious enthusiasm for life has helped to keep me motivated throughout the process. I'm not sure that I would have made it to this point without your support; for that I will always be grateful.

Abstract

Meson spectroscopy aims to study the masses and decay processes of mesons to better understand the mechanics of Quantum Chromo Dynamics in the strong coupling (non peturbative) regime. The Edinburgh group are spokespersons on a major new proposal at the Thomas Jefferson National Laboratory called MesonEx. This experiment will make use of the newly upgraded 12 GeV electron beam and detector systems to produce and measure the properties of mesons of interest for study. Edinburgh also leads the development of a fast timing Hodoscope, part of the new Forward Tagger detector system that will be essential to the success of this experiment. The primary focus of this thesis is the development process of the Foward Tagger Hodoscope, from its inception up to its installation at Jefferson Lab. The second part of the document will discuss the first measurement of the $\gamma p \rightarrow \omega\pi\pi p$ decay channel, with data from the g11a run of the CLAS (CEBAF Large Acceptance Spectrometer) in Hall B of Jefferson Lab. The analysis presents evidence for resonant contributions to the dataset decaying directly to $\omega\pi\pi$, via $b_1(1235)\pi$ or via $\omega\rho$. These include $a_2(1320)$, $\pi_1(1600)$, $\omega_3(1670)$ and $\pi_2(1670)$.

Lay Summary

Stable atoms can be thought of as a dense, positively charged nucleus, surrounded by a cloud of negatively charged electrons. The nucleus is formed from one or more nucleons: positively charged protons, and neutrons which have no overall charge. Positively charged objects repel each other due to the electromagnetic force between them, however in the nucleus, the protons (along with the neutrons) are held together by the aptly named Strong Nuclear Force, which is much more powerful than the other fundamental forces observed in nature, gravity, the electromagnetic and weak nuclear forces. However, the range of the strong force is short, not much greater than the size of a typical nucleus, limiting its area of influence. Despite this, the strong force's power is such that it is responsible for the generation of greater than 99% of the mass in the visible universe. Probing deeper, both protons and neutrons can be thought of as being formed from three quarks, which scientists currently believe to be fundamental particles, indivisible and one of the basic elements of matter. Quarks are also held together by the strong force, bound by a continuous exchange of appropriately named gluons which hold the quarks together.

Despite its strength, the mechanisms which govern the strong force are poorly understood by modern science. To gain new insight into its complexities, scientists need a tool to probe the subatomic structure of the nucleus. This is typically done by using high energy beams composed of particles, such as photons or electrons, which strike a dense simple target, such as liquid hydrogen. Reducing the complexity of reactions through the selection of the type of beam and target, allows the complex nature of strong interactions to be probed with precision. The aim of these experiments is to 'excite' the proton target into unstable states, and to measure the decays from these states with great precision. The results from these decays give great insight into the mechanics underlying the strong force and the fundamental structure of the world around us.

The first part of this thesis describes the development of a next generation detector system which will be integral to the success of new experiments designed to probe deeper into the structure of nucleons by using a higher energy electron or photon beam. The detector will be installed into The Thomas Jefferson National Accelerator Facility, one of the leading laboratories in America. It is designed to detect high energy particles which are produced from beam collisions, and to discriminate between them with a timing accuracy better than a billionth of a second.

The second topic of this thesis is an analysis of an experiment at Jefferson Lab, which used a beam of photons to strike a target composed of liquid hydrogen, cooled to less than -253℃. The experiment aimed to learn more about the structure of protons by studying particles which are produced when the high energy beam collides with the dense liquid hydrogen target. The analysis presents evidence for rare particles which exist only for a tiny fraction of a second before decaying. Information about these unusual states provides new insight into the underlying mechanics of the strong force. This analysis contributes to an ongoing worldwide effort to characterise the fundamental properties of the strong nuclear force, one of the great challenges of modern physics.

Contents

List of Figures

List of Tables

Part I

Searching for Exotic Mesons at Jefferson Lab

Chapter 1

Introduction

Ever since I began to study science, I have been fascinated by the fundamental forces which govern the mechanics of the universe. This thesis focuses on the study of the strong nuclear force, the most powerful and arguably least well understood of all the currently accepted forces in physics. The theory of Quantum Chromo Dynamics (QCD) provides a model to describe its mechanics and allows the results of interactions to be derived from first principles. However, currently QCD can only be resolved in the high energy limit, where perturbative approaches can be used. To gain insight into the true complexity of strong force interactions in the energy range that we experience, where quarks form bound states such as protons and neutrons, new approaches must be tested to gather more information and constrain the mechanics of Quantum Chromo Dynamics. This is the central aim of the work carried out during this PhD and the work presented in this thesis.

The thesis is divided into 3 parts. Part I gives context to the experimental and analytical work, by outlining some of the background theory which motivated the pursuit of the project. It also covers an introduction to the Thomas Jefferson National Laboratory and the CLAS detector, which are central both to the experimental work done in Part II of this thesis and to the data analysis presented in Part III.

Part II describes the design, development and construction of a fast timing Hodoscope for the new Forward Tagger detector to be installed as part of the CLAS12 upgrade of the Thomas Jefferson National Laboratory. This project formed the majority of the work undertaken during the PhD, developing the detector system from its early prototypes, and finally delivering the optimised

state it is today, performing well beyond its design brief. The detector system will be integral to the success of the Meson Ex project and other experiments in CLAS12, probing the spectrum of mesons between 1 and 3 GeV/c_2 and searching for exotic states, such as hybrid mesons, which are predicted to exist by QCD, but have never been experimentally observed.

Part III describes the first analysis of the $\gamma p \to \omega\pi\pi p$ decay channel, with data collected from the g11a photoproduction run at Jefferson Lab. This analysis was done as an investigatory study, in order to develop a new framework for use in an upgraded CLAS12 facility, and also to improve our understanding of a channel that has never been observed with an electromagnetic beam. Decays to $\omega\pi\pi$, in the energy range available in the CLAS6 dataset, include a number of meson resonances for which there is little experimental data. This channel has been identified by theorists as a 'golden channel' in searches for hybrid mesons with CLAS12, and the work described in Part III of this thesis has helped to prepare the ground for future exploration of this area.

1.1 Quantum Chromo Dynamics

In the 1960s, quarks were first proposed by Gell-Mann and Zweig [1, 2], and then discovered through deep inelastic scattering experiments at the Stanford Linear Accelerator (SLAC) [3, 4]. Since then, we have known that protons and neutrons, which form the basis of atomic nuclei, are not fundamental particles. Each one is composed of 3 quarks, between which are split the properties of each nucleon (proton or neutron). This has led to further questions about the internal structure of these nucleons: how are they formed from their constituent quarks? and how do they interact with each other? During the 1970s, a theory called Quantum Chromo Dynamics (QCD) was developed to explain, at a fundamental level, the phenomena associated with these interactions.

QCD describes the interactions between quarks via the strong nuclear force in Hadronic (multi-quark) particles, mediated by force-carrying gluons. There are 6 different types (or flavours) of quarks, each with a corresponding antiparticle. The properties of these are shown in Table 1.1.

QCD can be considered analogous to the well determined theory of Quantum Electrodynamics (QED), which describes the interactions that occur between

Quark	Symbol	Charge (e)	Mass (MeV/c^2)
Up	u	+2/3	2.3 ± 0.5
Down	d	-1/3	4.7 ± 0.5
Strange	s	+2/3	94 ± 6
Charm	c	-1/3	1270 ± 30
Bottom	b	+2/3	4180 ± 40
Top	t	-1/3	173210 ± 710

Table 1.1 *Properties of the 6 flavours of quarks [5].*

charged particles via the exchange of photons, the force carrier of QED. The equivalent of electric charge in QCD is colour charge, of which there are 3 types, red, blue and green. Each quark carries a colour charge in addition to its electric charge. Antiquarks carry corresponding anti-colours known as antired, antiblue and antigreen. In actuality, the notion of colour is purely for descriptive purposes; there is no equivalence between this and the colours we see [6].

In QCD, both quarks and the force-mediating gluons carry colour charge. This is quite different to the situation in QED, where photons carry no charge and simply mediate the force between other particles. Gluons can be considered to carry a mixture of colour and anti-colour that results in 8 independent types of gluon and a 9th colour singlet state, which only interacts with other singlet states. The number of gluons is due to the mathematics of the superposition of possible gluon states. The colour charge-carrying property of gluons means they actively participate in the strong interactions, rather than simply mediating the force [6].

This property greatly increases the complexity of interactions in QCD, in comparison to QED, making them impossible to evaluate analytically. It also creates the opportunity for alternative types of interaction, such as self interaction between gluons, leaving open the possibility of hypothesised hybrid states,(composed of quarks an excited gluonic field), or purely gluonic states, such as the glueball [7]. This feature of self interaction leads to two other important properties of QCD: colour confinement and asymptotic freedom.

Colour confinement describes the observation that quarks are always found in colour-neutral states, phenomenologically similar to the way that a combination of red, green and blue light produces white light. Examples of this include a

combination of red+blue+green, such as found in 3-quark states called baryons, or in 2-quark states called mesons, formed from a quark anti-quark pair. The same properties apply to gluons, which require them to exist only in combination with other quarks or in multi-gluon states such as a glueball.

To use an analogy, take two quarks held in a bound state, such as a meson, held together by the binding of the strong interaction through shared gluons. If energy is added to the system to force the quarks further apart, the strength of the bond between them rises, just like tension being added to a rubber band. However, at a certain point of extension, there is so much energy in the system that is it more energetically favourable to create a quark anti-quark pair out of the vacuum than to continue to extend the bond between the original pair. Thus, all quarks will continue to remain confined. This phenomenon is called Hadronisation and is regularly observed after high energy particle collisions, where jets of mesons are produced along narrow vectors [8]. A schematic diagram of the process is shown in Figure 1.1. For this reason, the combinations of quarks which make up hadrons need to be net colourless.

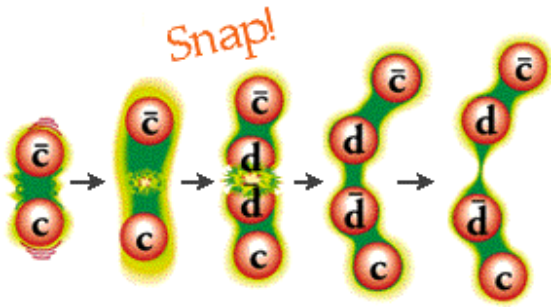

Figure 1.1 *The process of hadronisation occurring as 2 quarks are separated from one another. [9]*

Asymptotic freedom describes the phenomenon that at high energies and therefore short interaction distances, the strength of the strong interaction decreases. At infinitely small distances Quarks behave as if they are free, unaffected by other strongly interacting particles, forming a quark-gluon plasma [10, 11]. This property allows QCD to be calculated perturbatively at high energies. This is because the coupling constant is small enough to allow the infinite series of QCD interaction terms to converge. The converse of this situation is also true; as interaction energies decrease and the distance between interactions rises, the strength of interactions increases. This variation in the strength of interaction is described by the coupling constant of QCD, α_s,shown in Figure 1.2, often referred to as the 'running coupling constant', due to its changing value with distance of

interaction. At low energies, the strength of the coupling constant is far too large for perturbative calculations to converge, so alternative methods must be used to evaluate the strong interaction.

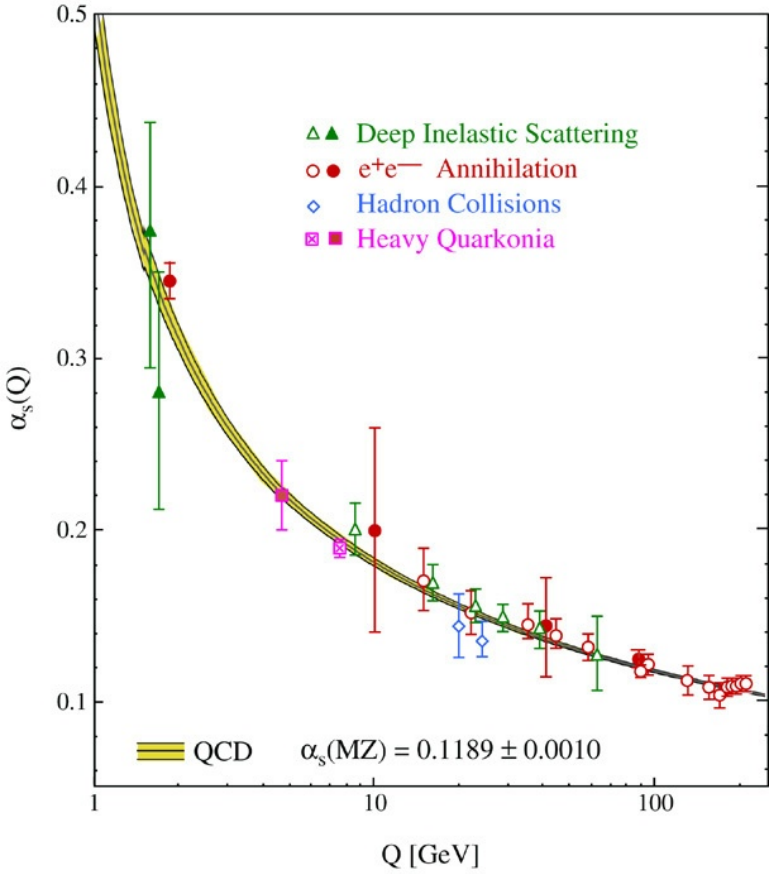

Figure 1.2 *The strength of the running coupling constant of QCD α_s is shown for a range of values of momentum transfer (Q). α_s varies with interaction energy and at lower energies the strength of the coupling constant rises rapidly, greatly increasing the complexity of low energy interactions [12].*

To understand QCD at low energies where, α_s is larger, two main approaches have been taken:

- Phenomenological models: These attempt to reproduce significant results while simplifying aspects of QCD, allowing the results to be solved analytically. These approaches are discussed further in Section 1.3.1.
- Numerical methods. These utilise computational power to simulate QCD under special conditions. The most successful of these is called Lattice QCD (LQCD) which is discussed in more detail in Section 1.3.2.

In order to constrain these models and allow a greater understanding of the nature of QCD, further experimental evidence is required. Mapping out the range of hadronic states and their properties provides additional information to allow the underlying mechanisms of QCD to be understood and predictions to be verified. This process is called Hadron Spectroscopy and is discussed in the following section.

1.2 Hadron Spectroscopy

Spectroscopy, or the study of the interaction between electromagnetic radiation and matter, is an approach that has its origins in the 17th century, most famously through Newton's study of the spectrum of light using prisms. In the early 20th century, atomic spectroscopy was used to study the absorption and emission spectra of elements. This allowed us to map out the quantised energy levels available for electron transitions and led to Bohr's quantised model for the structure of the atom which helped to constrain the early development of quantum mechanics [13]. Based on the success of this approach, Hadron Spectroscopy utilises a similar model to study the spectrum of hadronic states.

- Excite the subject of interest to a higher energy state
- Measure the decay (protons, neutrons, π's, ω's, photons, ...)
- Map out the spectra

Attempts to determine the spectrum of lower energy hadronic states identified a number of symmetries between states, along with a series of quantum numbers which are maintained within each group. An early example of this was that after the neutron was discovered, it was postulated that the proton and the neutron were two different states of the same particle, because of their nearly identical mass [6].

To provide further structure to this description, consider the quantum number hypercharge (Y):

$$Y = B + S + C + \tilde{B} \tag{1.1}$$

Where B, S, C, and $\tilde{B}$ are defined as baryon number, strangeness, charm and beauty. Each of these is associated with the particular quark composition of a hadron.

To differentiate between hadrons with the same quark composition but a different charge, a further quantum number is required, called isospin projection I_3. This can be defined in terms of hypercharge and electric charge (Q) as:

$$I_3 = Q - \frac{Y}{2} \tag{1.2}$$

Within a nucleon only B=1 is non-zero and hence the values for a proton and neutron are I_3 = +1/2 and I_3 = -1/2 respectively.

The same principles can be applied to other hadrons, based on the number of differently charged states available. For example, for pions all contributions to Y are 0 and there are 3 different states, π^+, π^- and π^0. Therefore the I_3 numbers of these pions are +1, -1 and 0 respectively.

These groupings can also be extended in hypercharge space, for example extending nucleons to include other baryons with a differing combination of quarks, including strange quarks, whilst maintaining the same total spin and parity, often written J^P. This is shown in Figure 1.3 forming an octet.

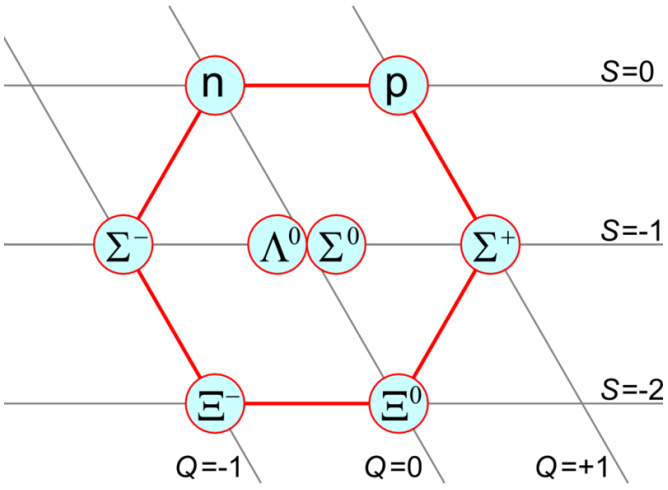

Figure 1.3 *A octet of baryons with each each having same total spin and parity. Each baryon is formed from combinations of u,d and s quarks, with lines determined by the respective charge and strangeness of each baryon [14].*

A grouping including the lightest mesons, pions, for $J^P = 0^-$ can also be

Parity and Charge	Isospin = 0	Isospin = 1
$--$	ω_J	ρ_J
$++$	f_J	a_J
$+-$	h_J	b_J
$-+$	η_J	π_J

Table 1.2 *Typical naming conventions for light unflavoured mesons. The total angular momentum index, J, is often omitted for states with $J = 0, 1$.*

represented in a similar manner as shown in Figure 1.4. This group is referred to as pseudoscaler mesons.

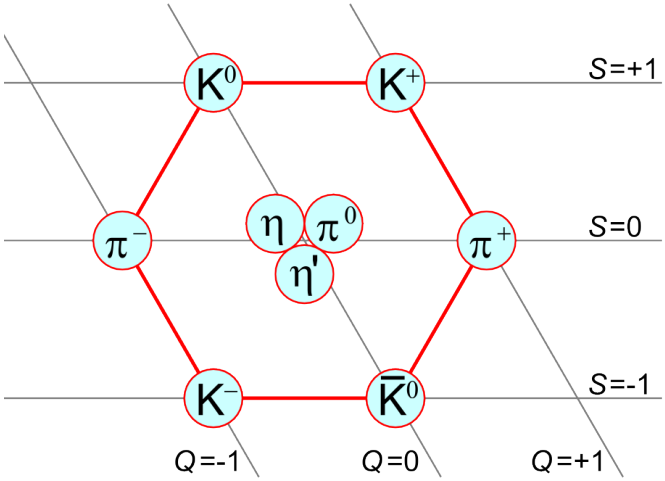

Figure 1.4 *The pseudoscaler $J^P = 0^-$ meson nonet. Each meson is formed from combinations of u,d and s quarks, with lines defined by the respective charge and strangeness of each meson [15].*

To describe the spectrum of possible states two additional quantum numbers are required which are both conserved in strong interactions. First the total Isospin (I), which accompanies the directional I_3 to describe the Isospin of a particle. Secondly G-parity (G), which is an generalisation of parity to allow it to apply to particle multiplets such as π^+, π^- and π^0. Quantum numbers of hadronic states are typically described using the notation $I^G(J^{PC})$, and these properties are used to define the naming conventions in hadronic physics. Particles with the same parity, charge and Isospin can be grouped together for example those used for mesons are shown in Table 1.2.

1.2.1 Hadronic Resonances

Decays from excited nucleon states proceed predominantly via the strong interaction. Because of the magnitude of the strong interaction, decays tend to occur over very short times and therefore can produce very broad mass resonances, as expected from the uncertainty principle.

$$\Delta E \Delta t \geq \frac{\hbar}{2} \tag{1.3}$$

For example, a ρ meson with a lifetime of 4.41×10^{-24} s has a resonant width of 149.1 MeV/c^2 [5]. The width of these resonances is often much greater than the energy difference between them, resulting in overlapping peaks, which makes them much more complex to isolate than typical resonances in atomic spectroscopy. A mass spectrum alone is rarely enough to isolate any but the most well known decays, so higher level analysis techniques are required. An example of this is gaining additional information from polarisation observables by considering the scatter distributions of particles which are dependent on the particle properties, beam and target polarisations. Another example is partial wave analysis, where all contributions to a reaction are considered as an interacting sum of partial waves based on their angular momentum contributions. Considering the different possible contributions to a reaction, resonant structures can be reconstructed by finding the most likely resolution of these partial waves. This can potentially extract overlapping signals from one another and reconstruct resonant structures previously hidden behind other contributions.

Focusing on investigating the spectrum of mesons, the simplest bound quark state, reduces the number of degrees of freedom for interaction, making it easier to understand the characteristics of QCD. Many of the lower energy meson states are well constrained, with extensive experimental data collected on their properties [5]. However, beyond this there is often limited experimental data, with masses, widths and cross-sections of decays poorly determined; consequently there is lower confidence in the results. However, with the advance of technology and access to higher energy and more intense beams, these states can be probed with greater precision allowing extraction of the resonance properties.

Higher order states containing more than 3 quarks are also predicted by QCD. Some of these more exotic states are predicted to contain either further quarks

such as 4-quark tetraquarks ($q\bar{q}q\bar{q}$) or 5-quark pentaquarks ($qqqq\bar{q}$) [16, 17]. Others are expected to include gluonic degrees of freedom such as hybrid mesons (qqg) or glueballs (gg) [7, 18]. Early models used a flux tube to model a gluonic component to hadrons [19, 20]. However, recent developments in theory allow these to be modelled directly from QCD [21]. A clear signature of these exotic states would be particles detected with previously forbidden quantum numbers, that could be accessed only by particles with additional degrees of freedom not available to standard hadrons. The search for these is one of the primary aims of the new Forward Tagger for CLAS12 [22]. This forms the focus of the second part of this thesis.

Calculations from Lattice QCD predict the lightest of these exotic states to be found as low as 1.8 GeV/c^2, with others accessible just a few hundred MeV higher [23–25]. This energy range is accessible through the beam energies available in CLAS12 and photoproduction is the ideal tool to investigate this exotic spectrum. This is because a quark interaction involving spin-1 photon, rather than a spin-0 pion, does not require a further spin flip of one of the quarks in the produced meson to produce a meson with exotic quantum numbers. Therefore a major factor suppressing the production of exotic states is removed. Some literature even predicts that the rate of production of hybrid mesons should be comparable to normal mesons through photoproduction [26]. This is quite unlike the production mechanisms in pion beam experiments, which currently represent the vast majority of experimental datasets.

There is a growing amount of experimental evidence for the existence of some of these exotic states; however many of the results are strongly disputed and require independent measurement in multiple decay channels before any discovery can be confirmed [27, 28].

1.3 Theoretical Models of QCD

There are many different models that aim to reproduce the mechanics and behaviour of strong force interactions. Some of these begin from the underlying QCD Lagrangian while others seek to reproduce phenomenological features through models.

1.3.1 Phenomelogical Models

Constituent Quark Model

In the constituent quark model, a nucleon is modelled as being composed of three valence quarks, each accounting for a third of the mass of the nucleon. These quarks provide all the degrees of freedom of the system and the gluonic field is not excited [29]. There are variations of this model, though all require some approximations to allow them to work; but even with these, they can accurately predict many of the masses, orderings and spacings of current experimentally determined excited hadronic states. Significantly though, these models predict many more states than have currently been observed experimentally; a typical ratio would be 4:1 predicted to detected. Whether or not this discrepancy is due to lack of experimental sensitivity or flaws in the construction of the model is still to be resolved. However recent Lattice QCD simulations have predicted a similar quantity of states, if not all located in the same locations. This is discussed further in Section 1.3.2.

Diquark Model

The diquark model attempts to address the difference in the number of predicted and observed states. It achieves this by considering a nucleon as a system of a tightly bound diquark pair and a separate valence quark, as shown in Figure 1.5. This restriction reduces the number of degrees of freedom in the system, leading to a reduction of the number of states predicted [30]. This model has had some success in mapping the structure of hadronic states [31]. However there is currently no evidence from deep inelastic scattering of any point-like diquark structure in the nucleon; LQCD simulations have also observed little contribution from diquarks [32]. The existence of a diquark structure in nucleons is still an unresolved area in physics.

Figure 1.5 *A simplified representation of the diquark model with a bound diquark pair and a valence quark [33].*

Bag model

Bag models attempt to address the problem of confinement in a phenomenological way. They model nucleons as if they are a part of a hadronic phase generated by a concentration of energy that creates a 'bubble' in which quarks and gluons can propagate. However, gluons are confined within the boundaries of the system and 'drag' the quarks along with them. The volume which is maintained is a balance between the vacuum pressure of the energy contained within the system and the surface tension of the 'bubble' that surrounds it. Within these boundary conditions, perturbative QCD can be resolved and predictions made for the hadronic spectra generated by it [34]. Several variations of the Bag model have been developed, including the MIT Bag Model[35], the Soliton Bag model [36] and the Cloudy Bag Model [37]. Bag models have had some success in predicting the lower mass hadronic spectra, as shown in Figure 1.6.

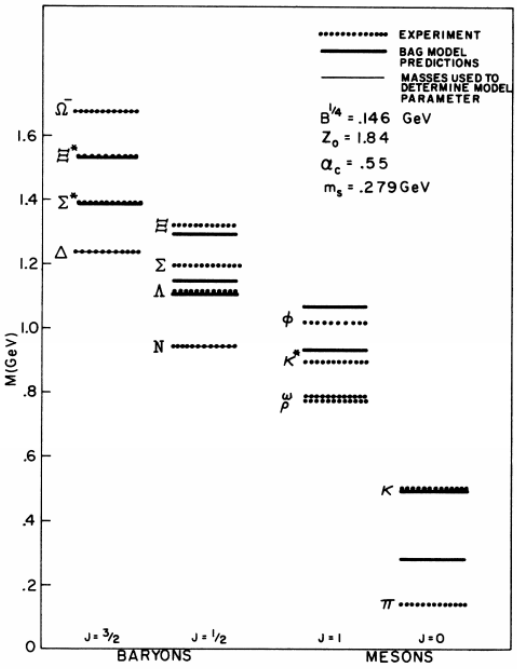

Figure 1.6 *Mass spectrum predictions using the MIT Bag Model. Experimental values of the states are also included, marked with dotted lines [38].*

1.3.2 Lattice QCD

Lattice QCD is a non-perturbative method for resolving QCD calculations by formulating them on a discrete Euclidean space-time grid. The description places

quarks and gluons as the primary degrees of freedom within strong interactions; fields representing quarks are defined on lattice sites and gluonic fields act between neighbouring points. At finite values of lattice spacing (a), there are no infinities and each site can be resolved separately to one another. In addition as $a \to 0$, and the size of the lattice tends to infinity, continuum QCD is recovered [39].

In principle, a lattice framework could also be used to perform perturbative QCD calculations; however, this would be much more complex than using standard continuum methods. Its real benefits come from its suitability for calculations to be split up and run simultaneously, using powerful parallel computational methods. The calculations involved are extremely computationally intensive and this is one of the main limiting factors to the continued development of QCD calculations. A major part of international efforts in the area is devoted to developing more efficient algorithms to process the calculations.

Numerical simulations of LQCD are calculated utilising Monte Carlo simulations of Euclidean path integrals. This introduces statistical errors along with the systematic errors inherent from the lattice spacing. Minimising these errors and properly understanding them is a critical part of utilising the method. This adds again to the computational loads involved in calculations [39].

Apart from the parameters of the lattice, the only other variables used in LQCD are the strength of the coupling constant, α_s, and the quark masses. Setting these parameters based on experimental results allows the system to predict the spectrum of other hadronic states. Alternatively, adjusting the strength of α_s allows the correlation between quark masses and the running coupling constant to be investigated. It should be noted that, with current theory and computational resources, it is necessary to calculate LQCD results with quark masses much higher than is experimentally observed, as it reduces the complexity of the simulation. The results are then extrapolated to experimentally observed pion masses using phenomenological models based from QCD.

There is rapid progress towards lowering the simulated quark masses and reducing the spacing of lattice sites in order to improve the quality of simulations. However, even with these limitations, recent developments in the technique have allowed predictions for the masses of the lowest mass hadronic state to within 1% of experimental values [40].

In comparison to the results of more phenomenological methods, QCD predicts a diverse variety of hadronic states, similar in quantity to the predictions of the

constituent quark model and far more than the diquark model. It also predicts the existence of exotic states that have additional dynamic degrees of freedom.

1.4 Summary

QCD describes the complex mechanics of the strong interaction between quarks and gluons. The self-interacting property of the gluons which act as mediators for the force, greatly increases the complexity of interactions, in comparison to QED. Currently QCD can be solved analytically only in the high energy limit, where the coupling constant of the interaction, α_s, is small. At lower energies, phenomenological models have been proposed that can predict, with some accuracy, many of the experimentally determined properties. A numerical method, LQCD, that models QCD as a space-time grid in Euclidean space, has provided a formulation to model non-perturbative QCD, without compromising the fundamental principles behind the theory. However, the method is extremely computationally intensive and only in recent years has technological advancement allowed the method to make sufficiently accurate predictions for the hadronic spectra.

In order to constrain the theoretical models of QCD, Hadron Spectroscopy is required to study the mass spectra of hadrons in a similar manner to the way in which atomic spectra have been studied in the past. There is extensive experimental data for the lower mass regions of the hadronic spectrum; however, outside this there is great uncertainty, leaving little information to constrain the mechanics behind QCD. With the upgrade of JLAB to a 12 GeV, CLAS12 will gain access to this higher energy regime in which LQCD predicts a wide variety of new hadronic states, including exotic mesons, some of which have quantum numbers forbidden to normal hadronic states. In order to study this higher energy regime, new hardware is required with performance surpassing anything previously developed, to create the resolution needed to detect these exotic decays. Chapter 2 will provide some background on JLAB and the wide acceptance CLAS detector situated in Hall B. Part II of this thesis will go on to discuss the new forward tagger, and the hodoscope system within it, which has been the main focus of this PhD. Finally, Part III will cover the investigation of the $\gamma p \to \omega\pi\pi$ channel from CLAS data. This is intended to prepare the ground for the search for exotics in the same channel in CLAS12.

Chapter 2

Jefferson Lab and CLAS

2.1 Background

The Thomas Jefferson National Accelerator Facility, more commonly known as Jefferson Lab or JLab, is a U.S. national laboratory located in Newport News, Virginia, U.S.A Its physics program is designed to probe the structure of hadrons in order to better understand the fundamental properties of nuclear matter.

The research program at the laboratory is based around the Continuous Electron Beam Accelerator Facility (CEBAF), a superconducting radiofrequency based accelerator employing two anti-parallel linacs, linked by 9 recirculation beam lines that allow up to 5 passes through the system. The facility produces a continuous wave electron beam with energies exceeding 6 GeV and luminosities of up to 10^{38} $cm^{-2}s^{-1}$. Luminosity describes the intensity of the beam, in this case the number of electrons incident on a target per second, per cm squared. For further information on CEBAF see [41].

The primary beam is separable and the facility is capable of delivering them concurrently to three different experimental halls for simultaneous experiments. The experimental halls at JLab are designed to be complementary, providing different facilities to address a broad range of physics goals.

In June 2010 construction began on an $338 million development to Jefferson Lab, upgrading the beamline to a maximum energy of 12 GeV and adding a fourth experimental hall to the facility (Hall D). The investment also includes upgrades

for the existing experiments in Halls A, B and C. This presents new challenges, but also new opportunities for the working groups.

Hall A is equipped with a pair of identical high resolution spectrometers capable of processing luminosities of 10^{38} $cm^{-2}s^{-1}$. Its research program includes work on nucleon structure functions and nucleon form factors [42].

Hall B houses the CEBAF Large Acceptance Spectrometer (CLAS), a wide acceptance detector designed to study electron and photon induced nuclear and hadronic reactions. The detector requires efficient detection of both charged and neutral reaction products in order to be able to study exclusive reactions, where all reaction products are detected [43].

In Hall C, the main focus is a pair of high momentum spectrometers;like hall A, it can also utilise the full luminosity of CEBAF. The working group studies topics including Separated Longitudinal and Transverse Structure Functions and the weak charge of the proton [44, 45].

The research in the newly constructed Hall D is based around a hermetic detector utilising a solenoidal magnetic field which has been specifically designed to study the gluonic field inside mesons, by studying the spectrum of exotic mesons [46].

The work presented in this thesis is focused around physics undertaken in Hall B at JLab and the CLAS detector situated within it.

2.2 CLAS

CLAS, which is situated in Hall B at JLab, is a wide acceptance detector utilising a toroidal magnetic field. Its primary design aims are to measure the momentum of charged particles with high resolution, covering a wide geometric area, and to keep a magnetic-field-free region around the target; this allows the use of dynamically polarised targets.

The magnetic field in CLAS is generated by six superconducting coils that are arranged symmetrically around the beamline. These produce a field primarily orientated in the ϕ-direction, perpendicular to the beamline.

The detector makes use of drift chambers to determine the trajectories of particles [48]. It uses gas Cherenkov detectors to differentiate between electrons and

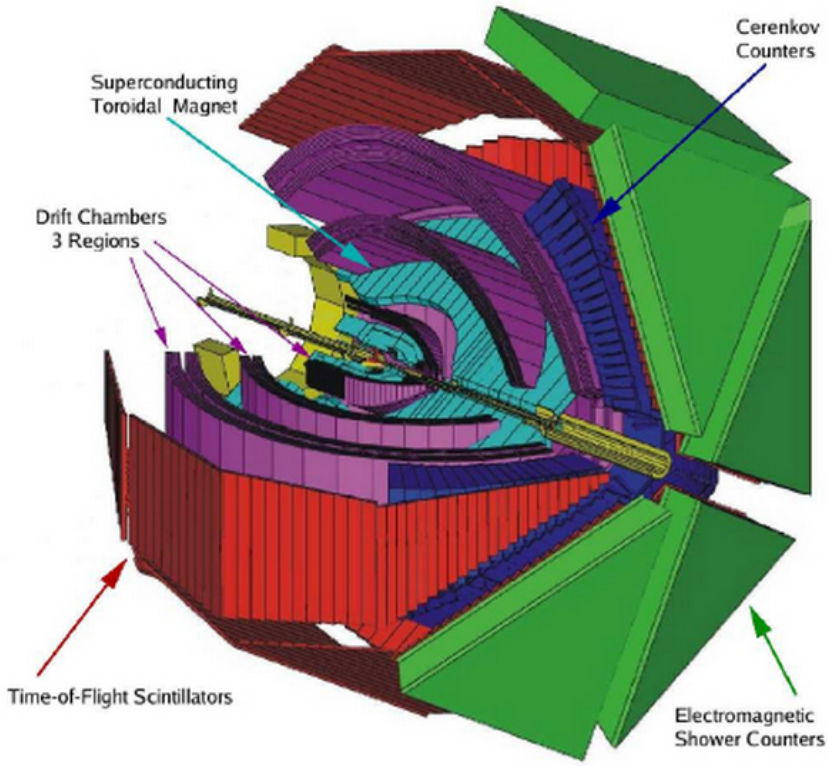

Figure 2.1 *A schematic diagram showing an overview of the CLAS detector with the different subsystems highlighted in separate colours. The beamline enters from the left of the picture, with the target region inside the innermost of the 3 drift chamber regions (Marked in Purple). The properties of particles propagating out from the target, are measured by a series of specialised detector systems [47].*

pions in the detector [49] and scintillation counters for measuring the time of flight (ToF) of particles through the detector [50]. Finally, there are two types of electromagnetic calorimeters (Forward and Large Angle) to determine the characteristics of particle showers and measure the energy deposited [51, 52]. A diagram showing the different sub-systems of CLAS, and their orientation in relation to one another, is shown in Figure 2.1.

The design means the detector is essentially composed of six independent magnetic spectrometers working in unison, with each sharing a common target, trigger and readout mechanism. The detector is designed to be suitable for both electron and photon beam experiments, but adjustments are made for different beam conditions. When an electron beam is in use, a 'mini-torus' is added around the target to shield the innermost drift chambers from electrons produced through Møller scattering in the target. For photon beams, a start counter is added inside the inner drift chambers, to provide precision timing for reactions [53].

2.2.1 Tagged-Bremsstrahlung

In CLAS, photon beams are produced by passing the CEBAF electron beam through a thin target (the 'radiator') positioned just upstream of a magnetic spectrometer (the 'tagger'). The system uses electron Bremsstrahlung reactions, during which an incident electron of energy E_0 is scattered by the electromagnetic field of a nucleus, causing an energetic photon to be released. The energy transferred to the nucleus during the reaction is negligibly small, so the energy conservation reaction can be written as:

$$E_\gamma = E_0 - E_e \tag{2.1}$$

E_γ is the energy of the photon and E_e is the energy of the post-reaction electron. If the energy of the electron beam is known, then the energy of the photon can be resolved from determining the energy of the scattered electron in a magnetic spectrometer [54].

The production angle of the photon is dependent on beam energy, and at energies greater than a few MeV, the photon and electron emerge at angles little deviated from the beam direction. The scatter angle of the photon, θ_γ, is also dependent

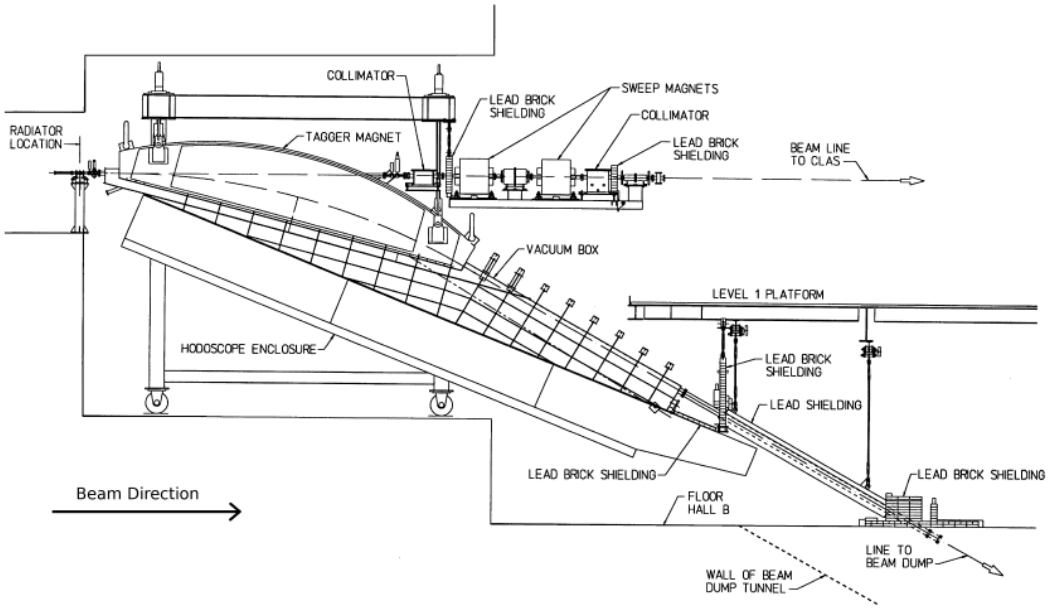

Figure 2.2 *Diagram of the layout of the photon tagger in CLAS, with the electron beam entering from the top left in the figure, incident on a thin target. The system uses electron Bremsstrahlung reactions, during which an incident electron of energy E_0 is scattered by the electromagnetic field of a nucleus, causing an energetic photon to be released. The unscattered electrons are channelled by the magnetic field of the tagger magnet, directly to the beam dump (bottom right of figure). Scattered electrons are bent towards the hodoscope, that measures their energy, allowing the energy of the energetic photons to be deduced. These are unaffected by the magnetic field and pass through a series of collimators, to produce a photon beam incident on the target in CLAS [54].*

on the rest mass of the electron m_e and follows the relation:

$$\theta_\gamma = m_e c^2 / E_0 \tag{2.2}$$

The corresponding scatter angle of the electron, θ_e, is given by:

$$\theta_e = \theta_\gamma E_\gamma / E_e \tag{2.3}$$

At the energies utilised at Jefferson Lab, both of these angles are of the order of one mrad or smaller. As a first approximation, it can be taken that the photon and electron travel in the same direction as the original beam. The photons pass through the field produced by the tagger magnet and continue on towards the beam target. These are further constrained by a series of collimators placed just downstream of the tagger. Details of this arrangement and the structure of the tagger are shown in Figures 2.3 and 2.2.

The strength of the tagger magnet is adjusted depending on the beam energy, to ensure those electrons that do not radiate will follow an arc directly into a shielded beam dump. Those that do will follow a tighter arc, with a spread dependent on the percentage of incident energy transferred to the photon and the strength of the tagger field. A flat plane segmented scintillator hodoscope is positioned to cover the arc of electrons, covering an energy range of 20% to 95% of the electron beam energy. This requires sufficient segmentation to provide adequate energy resolution and fast enough timing resolution to be able to separate the 2ns separated beam bunches. In order to minimise the effects of re-scattering, the electrons are passed through a thin exit window (made of aluminised Mylar), just after interacting with the radiator, into a vacuum chamber, until they reach the scintillators [54].

2.2.2 Torus Magnet

The magnetic field required for momentum analysis within CLAS is generated by six superconducting coils, arranged in a toroidal shape around the beamline. The combined arrangement forms a system of ∼5m in length and and 5m in diameter. The symmetric design produces a magnetic field which is primarily focused in the ϕ-direction, around the beamline, with some deviation close to

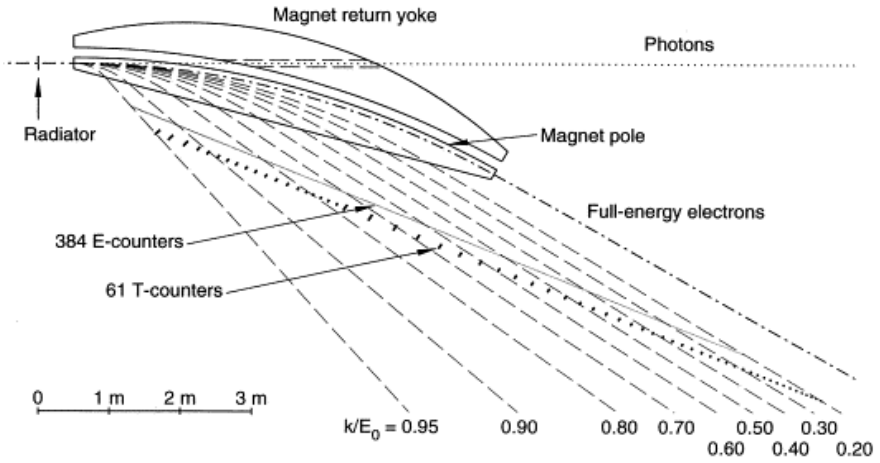

Figure 2.3 *Diagram of the Bremsstrahlung production mechanism and the spread of electron trajectories for different energies, which allows the energy of the photon beam to be resolved [54].*

each of the magnetic coils. This also maintains a largely field-free region in the centre of the detector, allowing for the operation of a polarized target. Figure 2.4 shows the vectors of the magnetic field from a viewpoint along the beamline. The length of the vectors is proportional to the strength of the magnetic field at each point [55].

Each of these coils that form the system is kidney shaped, producing a field which more strongly affects particles scattered at forward angles (with typically higher momentum), with more limited effects at wider scatter angles. At the maximum design current of 3860 A, the integral of the field strength of forward angles reaches 2.5 T, dropping to 0.6 T at a scatter angle of 90°. Field lines of equal strength are shown in Figure 2.5 from a perspective between two of the superconducting coils [56].

2.2.3 Drift Chambers

The magnetic field generated by the coils bends charged particles either away or towards the beamline, with minimal effect in the azimuthal direction. The particles' trajectories are measured by a 6-way symmetric arrangement of 18 drift chambers split into 3 'regions' (R1, R2 and R3), matching the natural geometry arising from the arrangement of the 6 superconducting coils. The R1 drift chambers are positioned just outside the target area in a region of low magnetic field [57]. The R2 drift chambers are positioned between the magnetic coils in an area of high magnetic field [58]. The R3 chambers are positioned

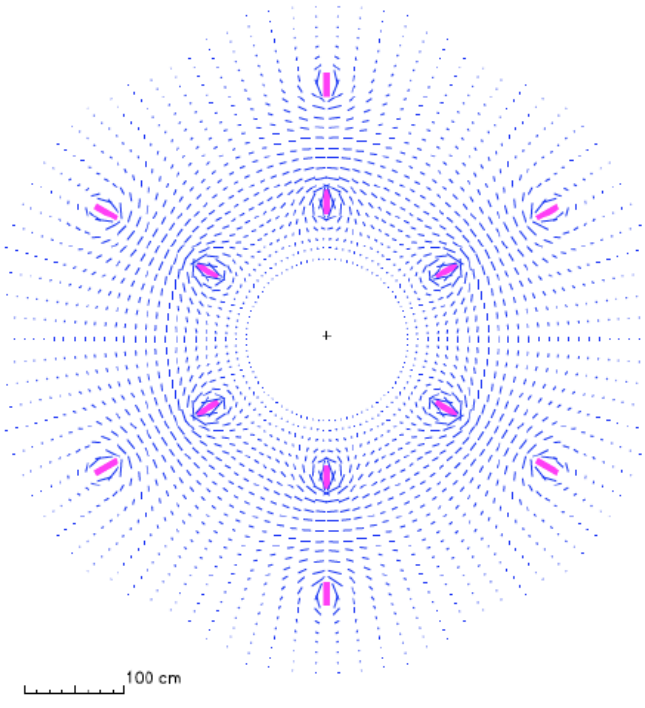

Figure 2.4 *The vectors of the magnetic field lines in CLAS, from a viewpoint along the beamline. The strength of the field at each point is proportional to the length of the field lines [47].*

outside the magnetic coils in a region of lower magnetic field. Their relative positions and orientations are shown in Figure 2.6.

For optimal coverage and maximum sensitivity to the radius of curvature, the drift chambers are positioned between each of the magnetic coils at 60° intervals, approximately perpendicular to the bend plane. The chambers fill the wedge shape detector volumes with field and sensing wires, spaced to form a series of 'layers' of concentric partial circles, with wires in each layer positioned half a wire diameter along from the next.This forms an arrangement similar in geometry to hexagonal close packing throughout the detector volume. The size of the hexagonal structures increases in proportion to the distance from the centre of the detector [48].

For improved tracking and azimuthal information, each drift chamber is split into two 'superlayers', one axial to the magnetic field and the other with a 6° tilt to provide stereo azimuthal information. An exception to this is R1; due to space limitations it has only a single axial layer.

For safety and detector longevity reasons, the wire chambers are filled with a $88\% - 12\%$ mix of argon and CO_2 which is controlled by an active feedback

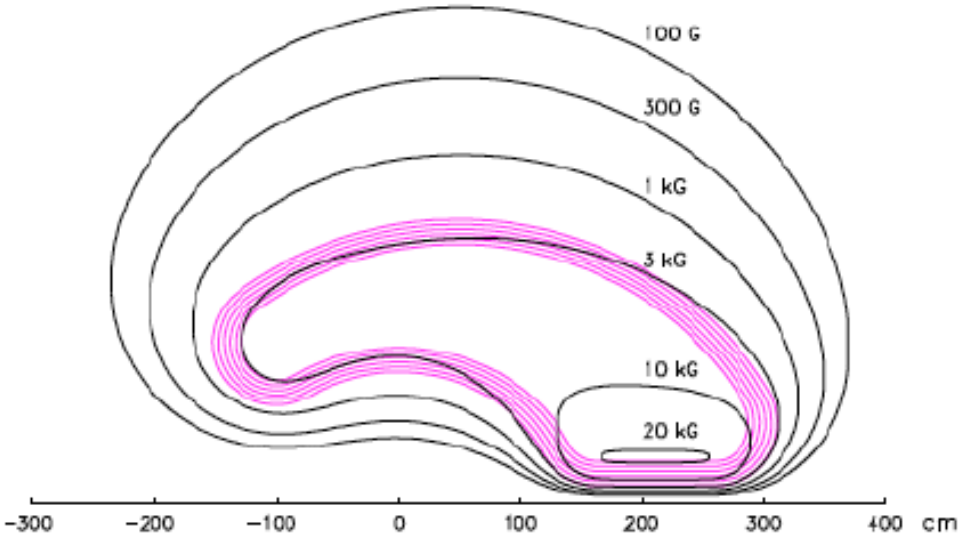

Figure 2.5 *Field lines of equal strength are mapped for one of the kidney shaped toroidal coils from a perspective between two of the superconducting coils. The length axis is marked with the nominal target position at zero and the direction of the beam in the positive direction. The strength of the magnetic field is biased towards lower scatter angles where the most energetic particles are produced. The dimensions of the coil are highlighted in pink, one of six surrounding the beamline [47].*

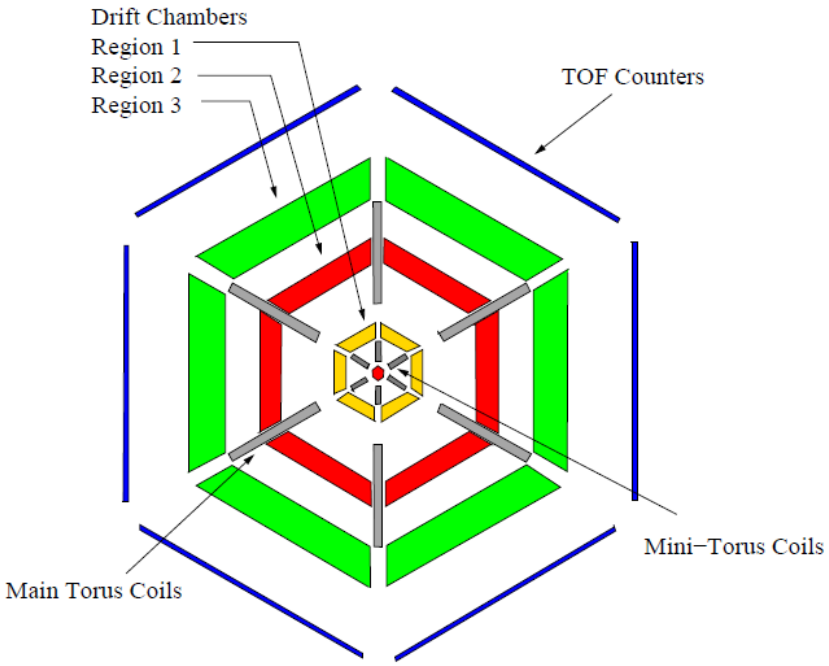

Figure 2.6 *From a perspective along the beamline, the Drift Chambers positions are highlighted in relation to the magnetic coils and Time of Flight (TOF) counters in CLAS. The mini-torus included in this figure is in place for experiments using electron beams. This system is replaced with a start counter for photon beam experiments [47].*

system which maintains constant conditions, adjusting for any changes in the surrounding environment.

The detector resolution is dependent on single wire resolution, along with uncertainties from multiple scattering in the material, the true value of the magnetic field strength and misalignments in the geometry of the detector system. Single wire resolution is dependent on where within the cell a track passes. There is increasing uncertainty when close to either the sensing or field wires and improved resolution towards the middle of each cell. This is due to ion-pair production near the sensing wire and divergence of the magnetic field and time walk effects near the field wires in a cell. The resolution for a track pathing in the mid region of a cell is 200-250 μm, with a whole cell average of 310, 315 and 380 μm for R1, R2 and R3 respectively [43].

2.2.4 Cerenkov Counters

The Cerenkov counters serve the dual purpose of differentiating between electrons and pions and providing a trigger on electrons. They are designed to maximise the solid angle coverage in each of the six sectors up to $\theta = 45°$, whilst using the minimum amount of material, to limit its effect on energy resolution. This is achieved by placing the photomultiplier tubes and light collection cones in regions in ϕ which are already shadowed by the structure of the toroidal magnets, and covering as much of the solid angle as possible with mirrors.

Coverage of θ in each of the six sectors of CLAS is divided into 18 regions and each of these is further subdivided into two modules bisecting the centre of each of the 6 sectors. This results in a total of 12 identical subsectors about the ϕ-axis for each of the 18 sections in θ, for a total of 216 Cerenkov modules [49].

2.2.5 Time of Flight Counters

This detector system covers the angle from the beamline, θ, between 8° and 142° and works in conjunction with the start counter, when using photon beams, to determine the time of flight (ToF) of particles within CLAS. Particles propagating radially outwards from the target will, after passing through the drift chambers, reach the ToF counters, and also the Cerenkov counters (but only if travelling at forward angles).

The detectors are composed of Bicron-408, a fast-responding plastic scintillator, in sections 5.08cm thick, designed to produce signals of large amplitude from minimum ionising particles passing through the detector. Each scintillator block is positioned to be perpendicular to the mean propagation direction of reaction products, covering $\sim 1.5^\circ\,\theta$. The forward angle counters ($\theta < 45^\circ$) are 15 cm wide, and those at wider scattering angles are 22 cm wide in the $\Delta\theta$ direction. The forward angle counters are between 32 and 376 cm in length and the wide angle detectors are 371 to 445 cm in length, with timing resolutions of $\sigma = 90 - 160$ ps. For scintillators of these dimensions, the dominant contribution to timing resolution is the varying path length of photons produced in the materials on their way to the PMTs. For further information on the ToF counters see [50].

2.2.6 Electromagnetic Calorimeters

CLAS utilises a Forward Electromagnetic Calorimeter (FC) that covers its full acceptance range in ϕ and up to $\theta = 45^\circ$ and an additional Large Angle Electromagnetic Calorimeter (LAC) that covers 2 of the 6 sectors of CLAS in the range $\theta = 45^\circ$-75°. This section will focus on the main FC but the LAC has a similar design. Additional detail can be found in [52]. The main functions of the FC detector system are identification and triggering of electrons above 0.5 GeV, detection of photons above 0.2 GeV (for reconstruction of π^0 and η), and neutron detection. It covers a range up to $\theta = 45^\circ$ and is constructed from alternating layers of lead and scintillator in a 0.24 ratio.

The system is split into 6 sectors positioned between the coils of the torus, forming a shape approximating an equilateral triangle. There are 39 layers in the detector system, composed of 10 mm of scintillator, followed by 2.4 mm of lead. These layers follow a 'projective' geometry directed towards the nominal target position, with each subsequent layer progressing radially outwards, covering a linearly increasing area. Each layer is composed of 36 strips rotated through 120° with respect to the previous layer and readout at one of the three edges of each sector. Depending on their orientation, the 39 layers are split into 3 groups (U,V and W) to provide stereo information on the location of the energy deposited. These groups are further subdivided into an inner (5 layers) and outer (8 layers) stack for greater longitudinal information in order to improve hadron and electron separation.

Hit reconstruction requires a hit in U,V and W layers of the detector in either the

inner or outer portions of a sector. Positions are calculated by reconstructing the intersection points of strips triggered above threshold, weighting appropriately for the timing of an energy response depending on the position of the hit in the detector system. Hits recorded within 10 cm of the edge of the detector volume are discarded, in order to ensure the full electromagnetic shower is contained within the sensitive region of the detector. Using electrons as an example for the performance of the detector, for those above 3 GeV, the sampling fraction of the system is ~ 0.3. Below this, the rate decreases, falling to 0.25 for electrons of 0.5 GeV. For electron showers that deposit more than 0.5 GeV in the scintillator, the rms position resolution is $\sim$ 2.3 cm. Finally, the timing resolution for electrons averages 200 ps across the detector system. For further information on the forward electromagnetic calorimeter see [51].

2.3 The upgrade to CLAS12

The last experiments utilising CLAS were finished in 2012 before the laboratory closed in order to allow the upgrade of the beamline to 12 GeV. To deal with the increase in energy, the equipment in each of the experimental halls has been upgraded. In Hall B the upgraded CLAS12 detector has retained many of the features of the previous design, with some systems upgrades and some entirely new ones added. The new design will provide increased resolution, kinematic coverage and improved particle identification over the previous detector. The detector will also be capable of operating at a luminosity of 10^{35} $cm^{-2}sec^{-1}$, an order of magnitude improvement over CLAS [59].

Some of the significant upgrades and additions to CLAS12 will be covered in the following section, before going on to cover in greater detail the new Forward Tagger in Part II of this thesis, which has been the major focus of my PhD. CLAS12 can be broken down into two major areas, the forward detector and the central detector.

2.3.1 The Forward Detector

The forward detector generally covers the range between 5° and 40° and is based around the same 6 fold symmetry as CLAS. The system is structured around a new set of 6 superconducting toroidal magnets, effectively splitting the detector

into 6 identical spectrometers, arranged at 60° intervals around the beamline. A cross-section of the layout of the forward detector is shown in Figure 2.7, and the major subsystems include:

- High Threshold Cherenkov Counter (HTCC)
- Forward Drift Chambers (FDC)
- Forward Time of Flight Counters (FTOF)
- Pre-shower Calorimeter (PCal)
- Ring Imaging Cherenkov Counter (RICH)
- Forward Electromagnetic Calorimeter (FEC)
- Forward Tagger (FT)

The CLAS12 forward detector maintains a similar configuration to CLAS with the FDC, Low Theshold Cherenkov Counter (LTCC), FTOF and FEC for momentum resolution and particle identification, with some upgrades to each. However there are also a number of significant additions to the detector systems. The new HTCC is positioned between the central detector and the first set of drift chambers, in front of the toroidal magnets, and allows greatly improved electron-pion separation with pion momentums up to 4.9 GeV/c. The detector is composed of low mass composite materials to minimise the contribution of multiple scattering to momentum resolution [59]. A RICH replaces the LTCC used in CLAS, allowing greater momentum resolution and extending the kinematic range of the detector system for particles momenta up to 8 GeV/c [60]. PCal is an additional calorimeter placed in front of the existing forward calorimeter from CLAS. It will provide additional granularity, improving the spatial resolution by a factor of 2.5 to allow the separation of high energy photons up to 10 GeV/c from $\pi^0 \rightarrow \gamma\gamma$ background. Finally, the Forward Tagger acts as a replacement to the existing photon tagger, covering the region between 2° and 4.5° from the beamline. This subsystem is covered in much greater detail in Part II of this thesis.

2.3.2 The Central Detector

The central detector is based around a superconducting solenoidal magnetic field with a maximum field strength of 5 T. The detector system surrounds the target

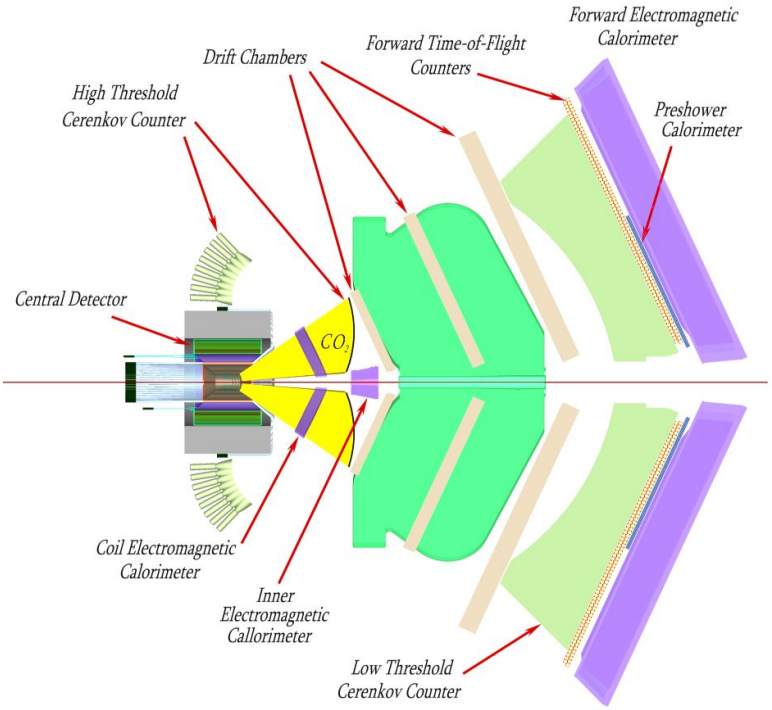

Figure 2.7 *CLAS12 cross-section focusing on the forward detector, showing the relative positioning of the different components. From the perspective of the diagram, the beamline enters from the left passing through the different elements of the detector. The new RICH is highlighted in bright green in the centre of the figure [47].*

volume symmetrically and its strong magnetic field allows the system to shield the tracking detectors from background Möller electrons, which are produced as the beam interacts with the target, and channels them down the beamline. It can also act as a polarising field for dynamically polarised solid state target. To allow this, the field needs to be very uniform with $\Delta B/B < 10^{-4}$ [59]. Other than these, the detector systems main purpose is to provide momentum tracking and particle identification, for particles scattered at more than 35° from the beamline. The systems used in the Central Detector include:

- Silicon Vertex Tracker (SVT)
- Central Time of Flight (CTOF)
- Central Neutron Detector (CND)

In the limited space available, very high magnetic fields and position resolution are required for momentum resolution and particle identification. At more forward angles, between 5° and 35°, the detectors systems work in conjunction with those from the forward detector to greatly improve on the resolution available to CLAS. The SVT is a combination between a barrel strip detector (BST), which covers azimuthal angles uniformly with a momentum resolution of better than 5%, and a forward strip detector which covers polar angles from 5° to 35°, working in conjunction with the forward detector. The CTOF is composed of 50 fast scintillator strips providing complete coverage in the azimuthal angle and provide timing resolution of 60 ps. The CND is placed just outside the CTOF and provides neutron detection using a series of scintillator strips with 10% efficiency and a momentum resolution of 5% [61].

2.4 Summary

Jefferson Lab's (JLAB) research program places it at the forefront of experimental research into the fundamental properties of QCD. The focal point of the experimental facility is the Continuous Electron Beam Accelerator Facility (CEBAF), that simultaneously delivers electron beams with energies up to 6 GeV to the 3 experimental halls of the laboratory. Situated in Hall B, the CEBAF Large Acceptance Spectrometer (CLAS) is designed to study reactions with both electron and photon beams (via a radiator). Its strong toroidal magnetic field

and wide acceptance in both the azimuthal and polar angular directions allow it to resolve hadronic reactions with varied reaction products. It achieves this using a combination of drift chambers, time of flight counters, Cherenkov counters and electromagnetic calorimeters, to gain nearly complete information on the products of a reaction.

In order to probe the spectrum of hadronic states at higher energies, the electron beam at JLAB is being upgraded from a maximum energy of 6 GeV to 12 GeV. To accommodate the new energy range, the experimental facilities in each of the halls are being upgraded. In Hall B, the CLAS detector is undergoing a major redesign (CLAS12), upgrading the maximum luminosity it can accept, and improving the resolution, kinematic range and particle identification capabilities of the detector. Utilising the new experimental facilities, it is hoped that exotic hadronic states will be discovered which are predicted by LQCD but have yet to be experimentally confirmed.

The new Forward Tagger for CLAS12 plays an integral role in the new physics plan for CLAS12 and the search for exotic states. A detailed description of the detector system and its constituent elements is covered in Part II of this thesis.

Part II

A Fast Timing Hodoscope for CLAS12

Chapter 3

The Forward Tagger

After the upgrade of the beamline, CLAS12 will receive electron beams with energies up to 11 GeV (only Hall D will receive the full 12 GeV beam). For photo-production experiments, the previous method of producing real Bremsstrahlung photons, tagged by a magnetic calorimeter, would require either significantly more space or a much stronger magnetic field to work with higher momentum electrons. Instead, an innovative redesign of the electron tagging system will be used, scattering electrons at very small angles to produce quasi-real photons. Quasi-real photons are virtual photons, such as those exchanged in electromagnetic interactions, with very low momentum transfer ($Q^2 < 0.1$ GeV/c^2), and within this limit have very similar properties to real photons. The scattered electrons that produce the quasi-real photons during interaction with the target, will be detected by the new Forward Tagger, which will act as an integral part of the trigger mechanism for photo-production experiments in CLAS12.

3.1 Electroproduction at very small Q^2

When electrons are scattered at very small angles (low Q^2), they can produce quasi-real photons. These photons have an intrinsic linear polarisation which can be determined from the scattered electrons energy/momentum and scattering plane. This is an advantage over the previously used method of producing Bremsstrahlung photons, as only the average polarisation can be determined for these. This knowledge provides extra information that allows the production

mechanisms of reactions to be better contained, refining the accuracy of partial wave analysis [62]. This method has been successfully used before at DESY [63] and CERN [64].

One of the major objectives of CLAS12 is the search for exotic mesons. Most previous meson spectroscopy experiments have used pion beams, CLAS12 will utilise a photon beam that is expected to increase the probability of observing exotic states. This is because utilising a spin-1 probe may favour the production of meson states where both spins are aligned, which would increase the probability of observing states with exotic quantum numbers [26].

3.2 Sub-systems of the Forward Tagger

The Forward Tagger is a new detector system designed to measure particle properties at forward angles, between 2° and 4.5° from the beamline. It has been designed to optimally detect the properties of electrons scattered at very small angles, with an acceptance exceeding 99% [61]. The new detector will be placed between the High Threshold Cherenkov Counter (HTCC) and the torus magnet support within CLAS12, in a limited space, at most 40 cm in length, just under 2 m downstream of the (nominal) target position. A simulation of the geometry of the Forward Tagger is shown in Figure 3.1.

The detector is composed of three major sub-systems:

- Electromagnetic Calorimeter (FT-Cal)
- Scintillation Counter (FT-Hodo)
- Tracker (FT-Trck)

The FT-Cal will detect the electrons, measure the energy of the electromagnetic shower, and provide a fast trigger for other detector systems in CLAS12. The FT-Trck will measure the scattering angles (θ_e and ϕ_e). The FT-Hodo provides electron/photon separation and further background reduction by taking measurements in coincidence with the calorimeter.

The limited region available for the detector and the close proximity to the beamline (2.5° corresponds to ∼8 cm) necessitates compact detector systems

which are able to process the very high flux present, while remaining highly resistant to radiation damage. All components are contained within a region <5° from the beamline, to minimize interference with any of the other systems in CLAS12.

An overview of the main subsystems of the detector will be given in the following section, before going to explore in more depth the design of the FT-Hodo which is the main focus of my thesis.

3.2.1 FT-Cal

The FT-Cal is a highly segmented lead tungstate based electromagnetic calorimeter which has to fulfil demanding requirements in a limited space. The detector requires high light yield and a fast recovery time (∼10 ns) for high energy resolution and minimal pile-up within the detector. Pile-up occurs where signals arrive quicker than the recovery time of a detector element, these either distort the original reading or are missed entirely. The FT-Cal also needs excellent timing resolution for tagger events, in conjunction with other systems within CLAS. Finally, it requires high radiation hardness, combined with a small radiation length and Möliere radius within the detector. The Möliere radius is the typical radius of the electromagnetic shower, perpendicular to the incidence vector of the charged particle, produced when it interacts with a material.

To achieve these objectives, the detector was designed to be highly segmented in the transverse direction, in order to maintain a sustainable output rate from each pixel. In addition, the transverse size of each element should be comparable to the typical Möliere radius of the electromagnetic shower produced in the detector. This will minimise unnecessary pixel firing by containing the shower to a limited number of crystals. A simple diagram of the FT-Cal is shown in Figure 3.2, showing the arrangement of the crystals.

Lead tungstate ($PbWO_4$) has been extensively studied and used in several large scale detectors in recent years [65, 66]. It was selected for the crystals in the FT-CAL because of its fast scintillation decay time (6.5 ns), short radiation length (0.9 cm), and limited Möliere radii (2.1 cm). The main disadvantage of the material is its limited light yield (0.3% of NaI(TI)). However, recent improvements in manufacturing processes and cooling of the material below 0℃ have shown an improvement in this by a factor of 6-8. With this configuration, an energy

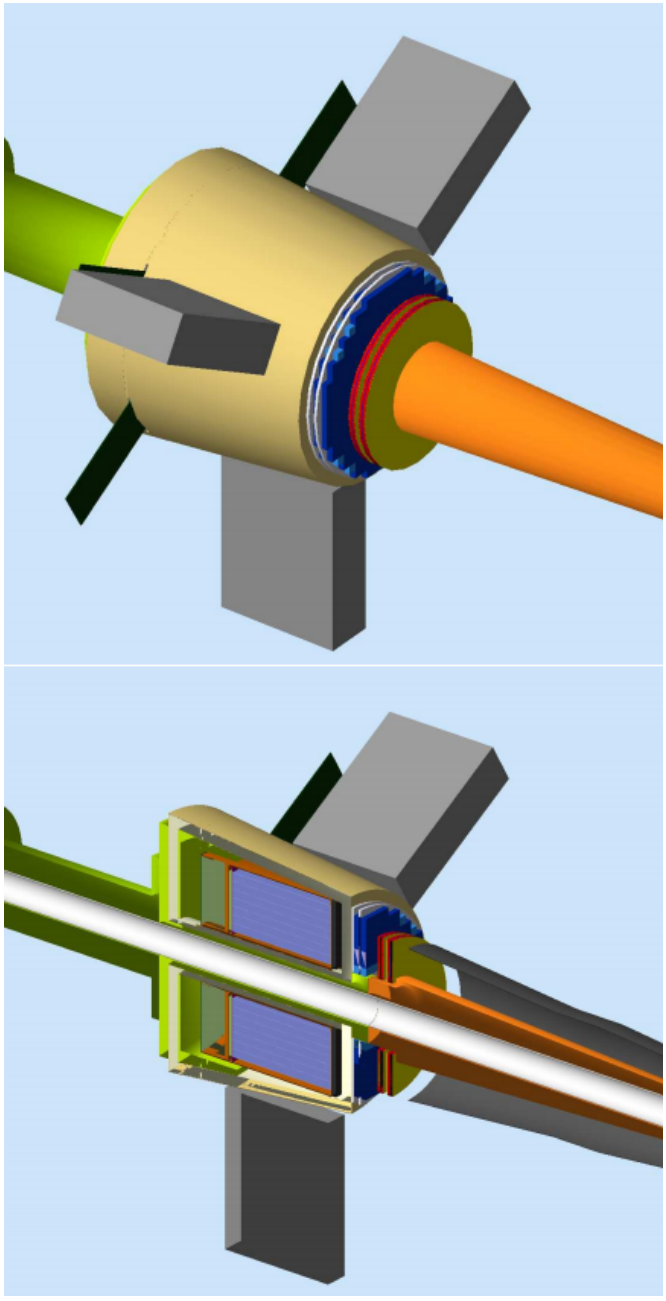

Figure 3.1 *The geometry of the Forward Tagger used in a simulation of the detector system is shown, from both an external view and in cross section. The crystals of the FT-Cal are highlighted in light blue, and the FT-Hodo's in Dark Blue. The FT-Trck is highlighted in bright yellow and red. The tungsten support pipe is coloured in green and the Möller cone in orange [61].*

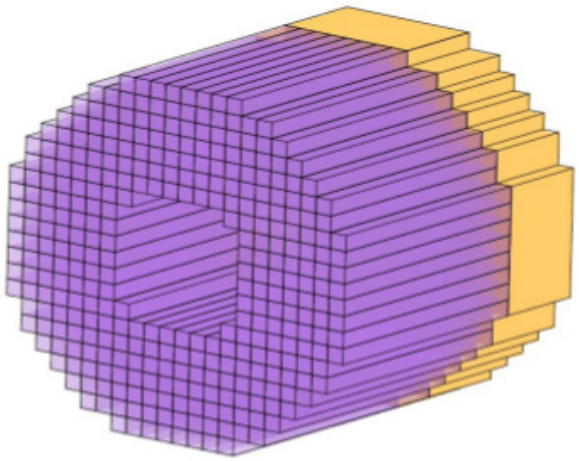

Figure 3.2 *A simple schematic diagram of the geometry of the Forward Tagger Calorimeter. With each of the individual lead tungstate crystals highlighted in purple and the readout systems in yellow [61].*

resolution of $\leq 2\%/\sqrt{E(GeV)}$ is expected.

The readout from the detector is required to operate in a high magnetic field, which excludes standard photomultipliers. Instead, Avalanche Photo Diodes (APD) were selected, as they have been shown to be both radiation hard and able to perform well under such conditions. Further information on the design and properties of the FT-Cal can be found in the forward tagger technical design report [61].

3.2.2 FT-Hodo

The main design objective of the Hodoscope is to differentiate between photons and electrons that interact with the Forward Tagger. The two particles produce indistinguishable electromagnetic showers in the dense lead tungstate of the FT-Cal. However, although electrons produce clear signals in the Hodoscope, photons will predominantly pass through the low z materials without interacting. Electrons will be identified in the Forward Tagger by observing near simultaneous hits, correlated in both position and time in the FT-Hodo and FT-Cal. To achieve this objective, the FT-Hodo must provide highly efficient charged particle detection, with similar spatial and timing resolutions to the calorimeter.

The Forward Tagger comprises a two-layered array of fast response plastic scintillator tiles, a thicker layer for improved timing resolution and a thin layer for

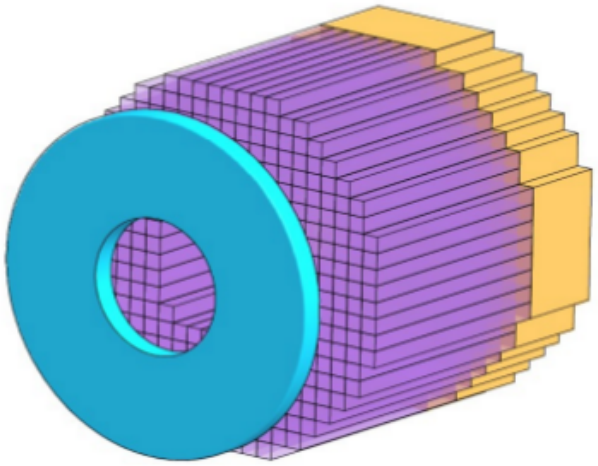

Figure 3.3 *A simple representation of the Hodoscope, highlighted in light blue, is shown in relation to the Calorimeter [61].*

enhanced background rejection. The positioning of the detector elements in the Hodoscope will mirror the layout of the FT-Cal, ensuring uniform coverage across the two detector systems. The restrictive geometry of the volume occupied by the Forward Tagger precludes the use of standard light guides and photomultipliers. Instead, each element is read out using embedded wavelength shifting fibres (WLSF), which are flexible and enhance the performance of the readout silicon photomultipliers (SiPM). Similar systems have been used in the past to achieve the sub ns timing resolution required [67]. Figure 3.3 shows the position of the FT-Hodo in relation to the FT-Cal.

The vast majority of particles incident on the Hodoscope will be highly relativistic, leaving a fixed minimum ionising deposition in the detector, regardless of particle momentum. As a result, having high energy resolution is not critical for detector performance. The main requirements for high detection efficiency and high timing resolution are the number of photons that reach the SiPMs and the efficiency of these detectors.

3.2.3 FT-TrcK

The role of the FT-Trck is to provide precise positional information to reconstruct the vertex angles of particles entering the forward tagger. It is composed of two double layer Micromegas (Micro-MEsh Gaseous Structure) detectors with a spatial resolution of ± 200 μm [68]. These work using similar principles to

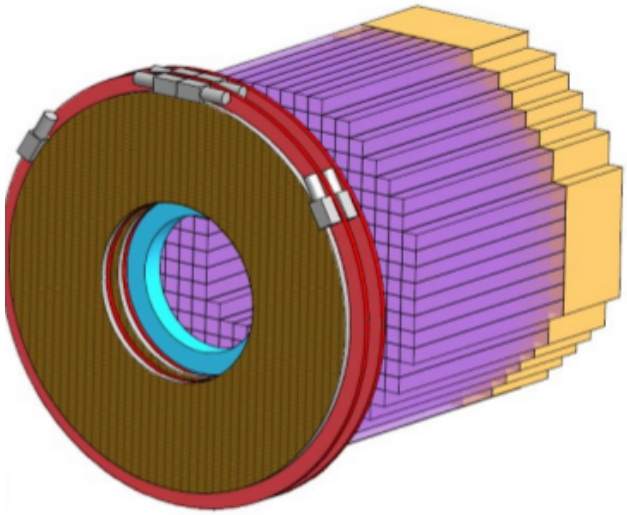

Figure 3.4 *The three major subsystems of the Forward Tagger are shown with the FT-Trck, highlighted in brown and red, superimposed in front of the FT-Hodo and FT-Cal [61].*

wire chambers, collecting ionised electrons from small pockets of gas within a wire mesh. Those used in the FT-Trck have a pixel width of 500 μm. Each Micromegas detector will provide an independent measurement of the (x,y) coordinates and act in conjunction with hits in the Hodoscope and calorimeter to improve background rejection. Figure 3.4 shows the position of the FT-Trck in relation to the FT-Cal and FT-Hodo.

This configuration of the FT-Trck is expected to achieve angular resolutions of $\sim$ 1.7% and 2.8° in the polar and azimuthal angles respectively. Further information on the design and properties of the FT-Trck can be found in the Forward Tagger technical design report [61].

3.3 Summary

The Forward Tagger is a new detector system for CLAS12 which measures the properties of particles scattered at shallow angles, between 2° and 4.5° from the beamline. It is an integral part of the trigger system for photo-production experiments in CLAS12, identifying the energy of the scattered electrons used in a quasi-real photon beam. The detector system is formed from 3 major components, the FT-Cal which measures the energy of the electromagnetic showers; The FT-Trck which accurately measures particle scattering angles and the FT-Hodo which

provides discrimination between electrons and photons. The FT-Hodo was the focus of my work for the project and its design is discussed in the next chapter.

Chapter 4

Design of the Hodoscope

This chapter will discuss in more detail the design of the Hodoscope, outlining the aims and constraints of its construction. Critical points will be highlighted and the interconnected nature of different elements elaborated upon. However, deeper discussion into the development decisions made and their consequences for the operation of the Hodoscope are reserved for Chapter 7, where some important sub-systems will be covered in more depth. A large proportion of the design, development and testing of the different components of the detector system were carried out by myself during this PhD. Many different experimental tests and prototypes of components were produced and assessed, but only the final versions are discussed in this chapter.

As discussed in Section 3.2.2, the main requirement of the Hodoscope is to differentiate between electron and photon hits in the calorimeter, because these produce nearly indistinguishable electromagnetic showers in the FT-Cal. It also utilises a two-layered design to minimise photon misidentification and suppress false events created through photon conversion. The detector will operate with sub-nanosecond timing resolution, to function as part of the trigger system, so as not to compromise the timing of the calorimeter. It will also achieve $> 99\%$ particle detection efficiency for the lifetime of its use and achieve this under conditions of 3.8 rad/h radiation flux and 5 T magnetic fields.

The hodoscope is positioned upstream of the FT-Cal fitting within a volume, no more than 330 mm in diameter and a depth of 40 mm. This limited space and harsh operating environment required an innovative approach to its development, to optimise the performance of the detector system. To achieve these ambitious

targets, the design of the FT-Hodo is based around a segmented array of plastic scintillator tiles (EJ-204) [69], embedded with Wavelength shifting fibres (Kuraray Y-11) [70] and read out by 3x3mm Silicon Photomultipliers (Hamamatsu S13360-3075PE) [71].

4.1 Plastic Scintillator Tiles

The plastic scintillators provide fast timing, sufficient light yield and resistance to radiation, necessary in the high flux environment of the Forward Tagger. The limited space, radiation and magnetic fields present in the detector volume require signals to be read out externally. WLS fibres were selected for their flexibility, excellent optical characteristics and radiation resistance. These fibres shift the wavelength of light produced by the scintillators into the ideal operation range for the SiPMs, but their attenuation length is relatively short at 3.5 m [70]. Because of the geometry of CLAS and the environment whilst the beam is active, the light needs to be transported more than 5 m to reach the SiPMs. To resolve this after $\sim$10 cm, still within the volume of the detector, the WLS fibres are fusion spliced to clear optical fibres which have an attenuation length $>$ 10 m [72]. This combination allows the scintillation photons to be transported to the readout SiPMs with a light loss of less than $<$ 40% [61].

Each layer of the Hodoscope is comprised of 44 15x15 mm (P15) and 72 30x30 mm (P30) plastic scintillator tiles, arranged with four-fold symmetry about the axis of the beam, covering the same acceptance as the FT-Cal, shown in Figure 4.1. At the centre, nearest the beamline, there is a continuous ring of P15 tiles where the flux is expected to be at its highest. Outside this, the majority of tiles are P30 type, with each one covering the same area as 4 crystals in the calorimeter. This configuration provides greater resolution in the area of highest flux, while increasing acceptance throughout the rest of the detector.

4.2 Wavelength Shifting Fibres

The photons produced in each of the 116 tiles in each layer of the Forward Tagger are read out using embedded WLS fibres. These fibres absorb the typically $\sim$ 400 nm, photons produced in the scintillator tiles and re-emit them in green, $\sim$ 470

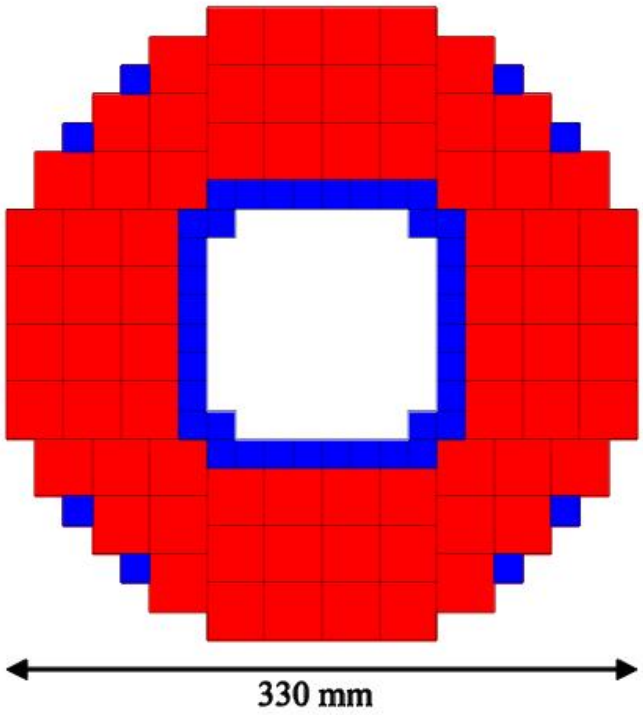

Figure 4.1 *Layout of the plastic scintillator tiles in the Hodoscope arranged symmetrically around the beamline in the centre of the diagram.* 15×15 *mm elements are shown in blue with* 30×30 *mm elements in red [61].*

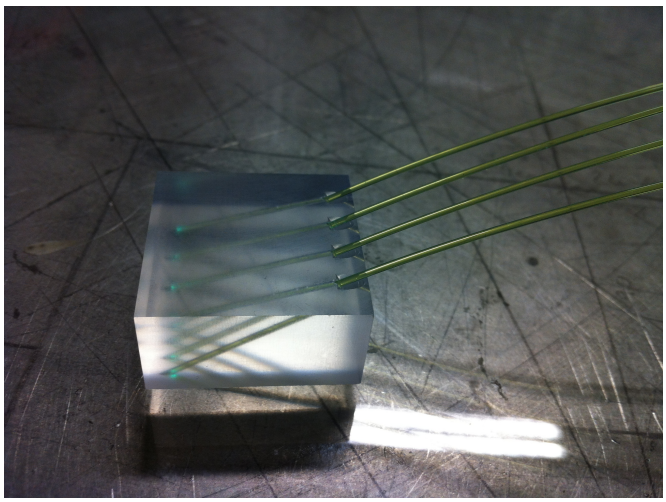

Figure 4.2 *A photograph of an unprepared 15 mm thick P30 tile occupied with 4 wavelength shifting fibres. The diagonally drilled channels for each fibre can be clearly seen.*

nm optical range, which is the ideal operating range for the SiPMs [70]. Each tile has diagonally drilled channels just larger than the 1 mm diameter of the fibres, four for a P30 tile and two for a P15. The channels are aligned to maximise the fibre length inside each tile, increasing the photon capture cross-section of each scintillation photon. The design also allows for the fibres to feed out naturally from each tile, while maintaining almost complete acceptance of the detector system. Figure 4.2 shows a photograph of a P30 tile, where the channels can be clearly observed, along with the route of the fibres out of the element.

The WLS fibres used in the detector are multiclad Kuraray Y-11(200) S-Type fibres 1 mm in diameter. This type of fibre has shown consistently excellent performance across a wide array of academic studies [73, 74]. The multi-clad fibres produce significantly higher light yield than traditional single-clad fibres, as the two layers of differing refractive index outside the core have a much greater photon trapping efficiency. The S-Type fibres were selected for their significantly increased resistance to crazing and their transmission at small bending radii (< 40 mm) - Crazing describes micro-fractures that damage the transmission properties of the optical components. The benefits of the S-type fibres come at the cost of transparency, leading to a $\sim 10\%$ reduction in attenuation length. This is insignificant for the short lengths of WLS fibre used in the detector.

The WLS fibres inserted into the tiles are fixed into place, using radiation hard optical cement of similar refractive index to the scintillator and fibre. This approach minimises the photon loss across the transition and holds the fibre in

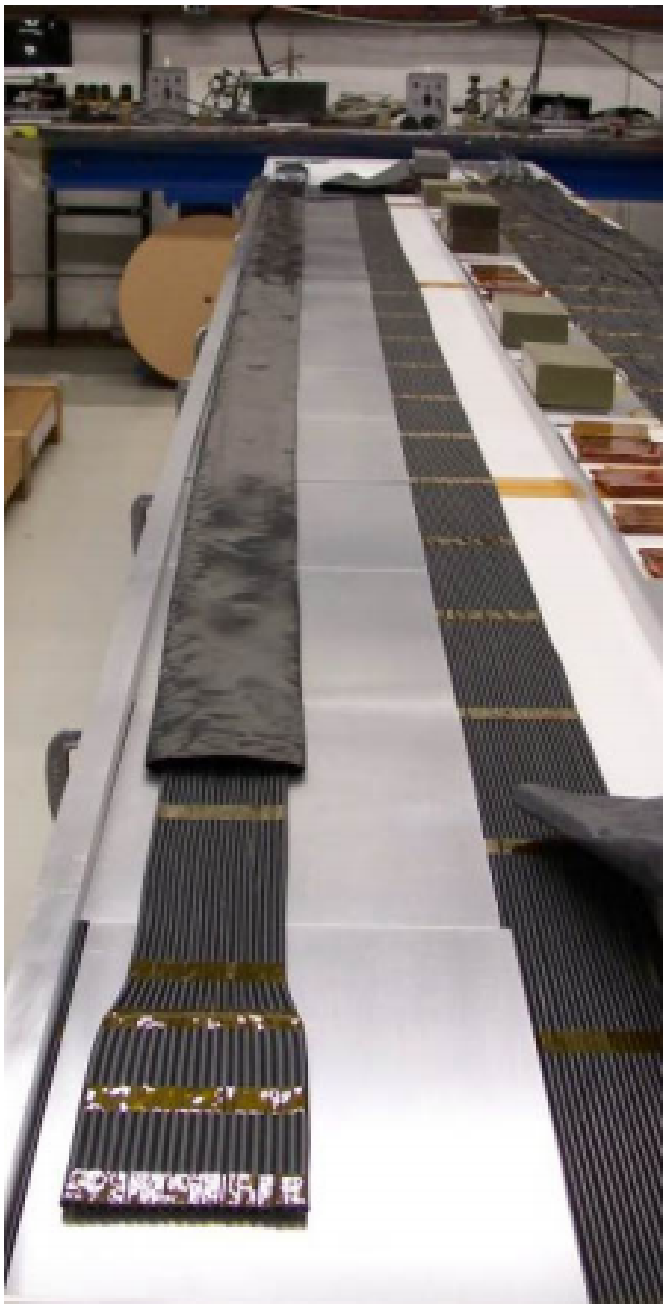

Figure 4.3 *A photograph of the full length spliced fibres, with protective sheeting, after fusion splicing at Fermilab. The fibres are put into groups of 4 and placed into protective black PVC sheathing to shield them from sources of UV light.*

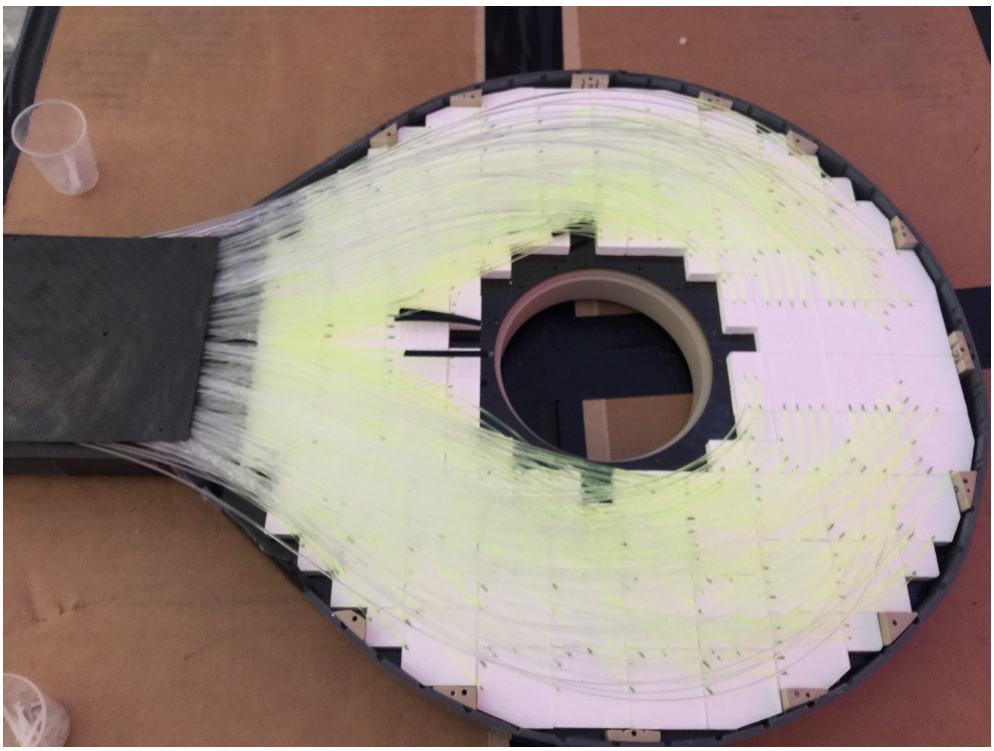

Figure 4.4 *A photograph of the Hodoscope with the carbon fibre lid from one of the layers removed, exposing the tiles and fibres beneath.*

place in any orientation of the Hodoscope. After 10 cm, each WLS fibre is fusion spliced to a $\sim$ 5 m long section of Kuraray double-clad clear plastic fibre, with much greater attenuation length. Fusion splicing melds the two fibres together at high temperatures, producing a join with with minimal loss of light, $< 2\%$. This process was carried out at Fermi National Laboratory, with 10 cm lengths of WLS fibre spliced to 6 m lengths of clear fibre. A photograph of the sliced fibres laid out on laboratory benches is shown in Figure 4.3.

4.2.1 Fibre Routeing

After exiting the tiles, the fibres are constrained by the limited space available above the tiles across the body of the detector. Ideally, each fibre would be allowed to curve as smoothly as possible on its route out of the detector, minimising the light loss due to the curvature of the fibre. However, there is limited space available for fibre routeing within the detector. This necessitates careful planning to avoid areas of over-density, which would restrict the fibres when exiting the tiles, or too much crossover, which would limit the amount of fibres which can pass through a particular area. These constraints are most significant in two

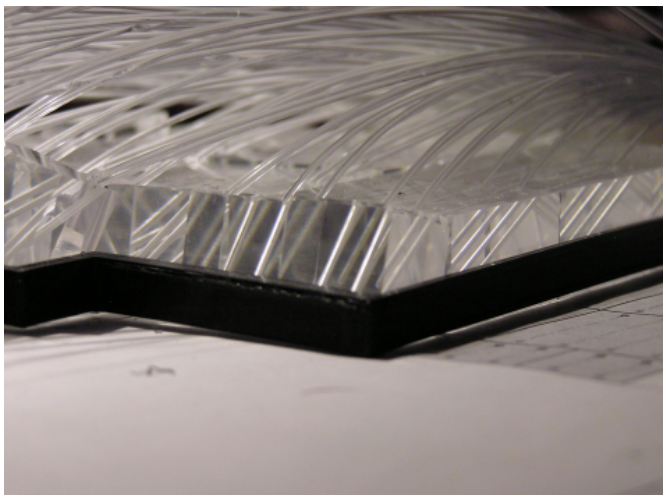

Figure 4.5 *A photograph of a fibre routeing test being carried out to optimise pathing within the detector. The test utilised lengths of clear fibres inserted into plastic tiles.*

areas: firstly, near the bottom of the detector where all the fibres have to pass on their route to the SiPMs, and secondly, near the centre of the detector where the density of fibres exiting tiles is highest. Further details on the solutions to these problems is given in Section 8.2.2. Figures 4.4 and 4.5 show the complexity and density of the fibre routeing throughout the detector volume for one of the layers.

4.3 Detector Enclosure

The base and lid of both layers of the detector are formed by a sheet of 0.5 mm thick black carbon fibre, shaped like an elongated disc, with a diameter of 330 mm, extended outwards at the bottom of the detector, shown in Figure 4.6.

Between the carbon plates is a central support ring made of Polyether Ether Ketone (PEEK), and, at the outer edge, 13 PEEK support pillars space the carbon fibre plates and provide locations for countersunk screws, to hold the outer and inner plates in place. Alternate holes pass directly through one layer into the layer below, allowing the two layers to be held firmly together by the supporting pillars. The outer pillars are positioned and individually shaped to fit in the limited gaps between detector elements, without interfering with the operation of the detector. A prototype of the carbon fibres disc and spacers in shown in Figure 4.7.

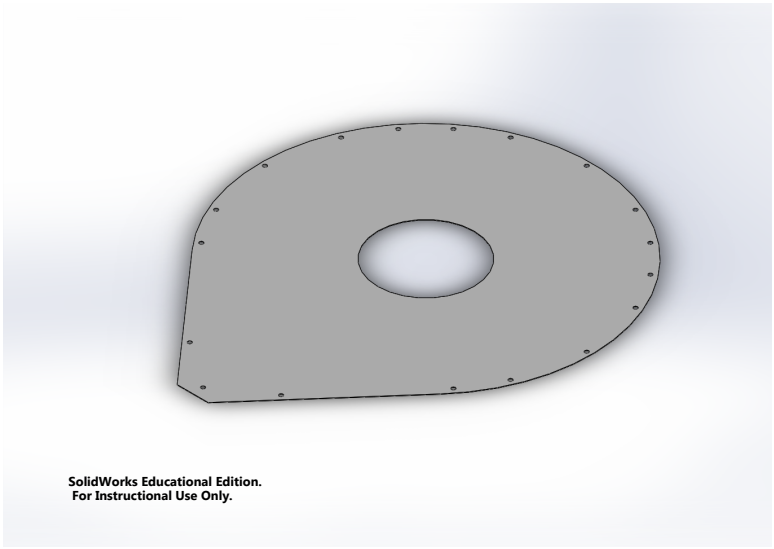

Figure 4.6 *A CAD diagram of one of the 0.5 mm thick carbon fibre plates used in the Hodoscope.*

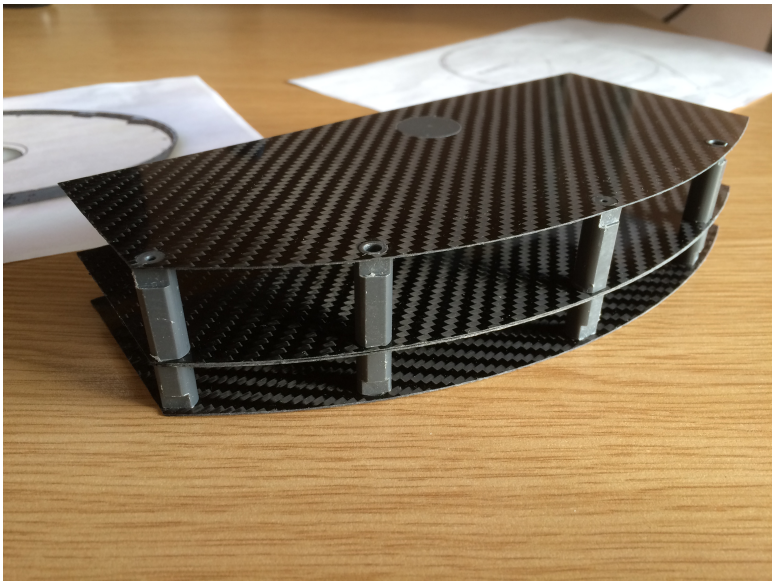

Figure 4.7 *A cutaway showing a prototype of the outer spacers used to hold in place and support the carbon fibre discs in the Hodoscope.*

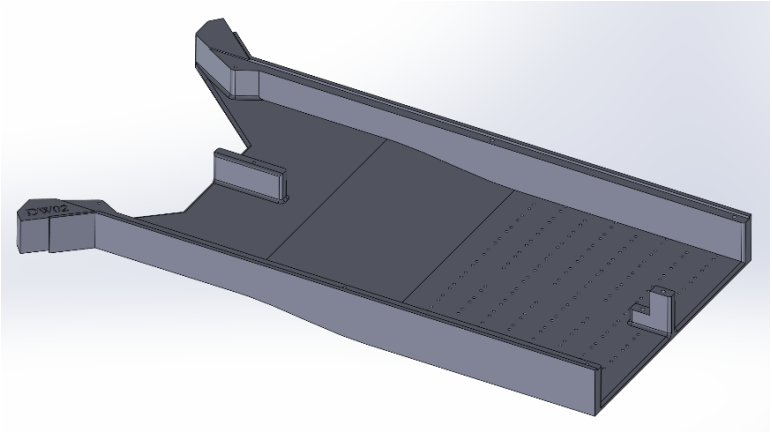

Figure 4.8 *A CAD drawing of the Hodoscope delta wing section that would be connected to the thin layer of the detector.*

The fibres in the detector exit each layer through a carefully designed 3D printed component called the delta wing. This critical component acts to channel the fibres out of each layer of the detector, holding them in place and helping to facilitate a light-tight seal for the internal components of the detector. It also acts as part of the supporting structure for the detector, replacing any supporting pillars at the base of each layer. The fibres are held in place by lacing cords that thread through holes in the base of each side of the delta wing. The component is split into two interlocking pieces, one for each layer of the detector, with greater depth allocated for the layer of thick tiles for improved fibre routeing. This is shown in Figure 4.8. As in the main body of the detector, each side of the delta wing is covered by a sheet of 0.5 mm thick carbon fibre secured by countersunk plastic screws, sealing in the fibres it protects.

The outer edge of the detector is a flexible plastic strip that bridges the two layers of the detector and is designed to allow the carbon-fibre discs to slot seamlessly into channels that run along its length, two back-to-back in the centre and one at the top and bottom, shown in Figure 4.9. It attaches to the detector system though countersunk screws which fit into the outer pillars of the detector and the delta wing at its base.

The spacing pillars and carbon fibre sheets combine to produce a lightweight but rigid and relatively strong construction. The carbon-fibre plates are very stiff in the direction of the weave of the carbon fibre, but they are inextensible and brittle in the transverse direction. The pillars, outer rim and delta wing help to offset these issues and the interlocking design spreads any weight-bearing across the entire structure. The structure is also completely composed of materials with

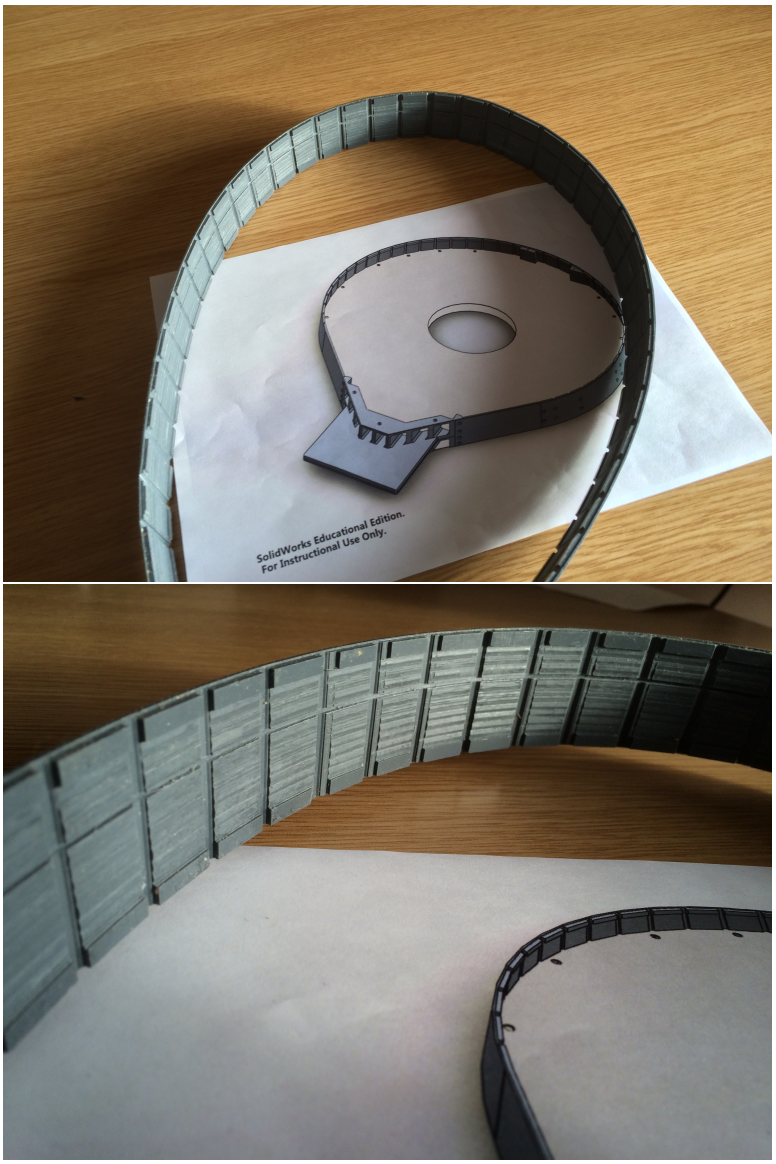

Figure 4.9 *Photographs of the flexible plastic strip that forms the outer edge of the Hodoscope. The channels for the outer and central carbon fibre discs can be clearly seen at the top, bottom and near the centre of the strip. The central channel is higher because of the difference in spacing of the thick and thin layers of the detector.*

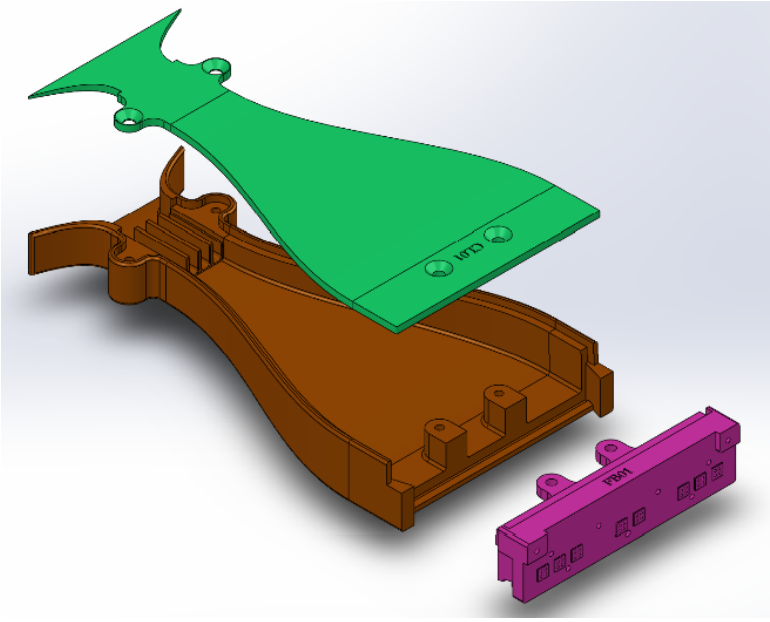

Figure 4.10 *A deconstructed 'fishtail' connector image showing the smoothly widening body, light-sealing lid and end connector which mounts onto the SiPMs.*

low atomic numbers, minimising the chance of any re-scattering being caused by the detector system.

Between the delta wing connector and the electronics, the optical fibres are grouped into bundles of four that are sealed from light and protected by flexible black PVC sheathing with an internal diameter of 3 mm. These are grouped together and pass through CLAS in cable trays, with weight bearing tethers strategically positioned to ensure the weight of the bundles is not borne by the fibres themselves.

4.4 Silicon Photomultipliers

The optical fibres join to the SiPMs via a 3D printed 'fishtail' connector, which spreads and positions the fibres in ideal locations for optical transmission. Each connector junctions fibres to supply eight different SiPMs, routeing up to a maximum of 32 optical fibres. The connectors are composed of three interlocking pieces, a smoothly widening body, a light-sealing lid and an end piece into which the fibres are glued, cut and polished. The separate end piece allows for easier insertion and replacement of fibres. A CAD drawing of this is shown in Figure 4.10.

The fibres from each tile are read out by an individual SiPM. These have high efficiency, high gain, fast timing response and are sensitive enough to trigger on single photons. These properties make them well suited for a fasting timing detector such as the FT-Hodo. SiPMs are highly sensitive to input voltages and require high voltage supplies, stable to 0.01 V, for optimum operation. However, their high gain allows for very clean signal separation from their main source of background, thermal noise. An electron signal from a thick tile is typically 20-30 times the magnitude of larger thermal background signals. In order to achieve a timing resolution < 0.5 ns, simulations indicate that SiPM signals with a magnitude of at least 55 photons are required. This target is one of the essential design requirements for the detector system.

In contrast to the Hodoscope, the FT-Cal utilises avalanche photo diodes instead of SiPMs, because of concerns over possible radiation damage. However, the APDs used in the FT-Cal are directly connected to the crystals in a region of high flux. The SiPMs used in the Hodoscope are positioned several metres away from the beamline and the main concern, neutron flux, is expected to cause minimal damage over the lifetime of the detector at these distances [75].

4.5 Signal Electronics

The SiPMs are mounted on mezzanine boards in two groups of eight, with each group supplied by a separate high voltage connection. There are 15 mezzanine boards in total providing support for the 232 channels of the Hodoscope. All the boards slot into a single VME crate, along with a control board, with a single low voltage rail supplying a uniform voltage to all the electronics. The controller board allows the high voltage supplied to individual channels to be adjusted through variable resistors on the pre-amplifier boards. It also provides monitoring for the temperatures of critical components in real time. The SiPMs are matched into groups with similar voltage requirements, but adjusting the voltage delivered to individual channels is necessary for optimal performance.

Signals from the amplifier boards are passed to the Flash Analogue-to-Digital Converters (FADC) that form the data acquisition system. These boards continuously digitise signals, using a fast Analogue-to-Digital Converter (ADC) and store the waveform if a trigger condition is met. The FADCs replace the ADCs and Time to Digital Converters (TDC) used in CLAS, thereby offering

several advantages. Firstly, FADCs store the entire waveform and not simply the charge deposited; this allows the potential for more sophisticated trigger conditions and offline analysis. Secondly, the system works in a circular cycle, so when a trigger occurs the current buffer is frozen and stored before readout, but the system continues acquisition into another buffer, thus reducing the deadtime in the system. Finally, there is no need for delay cables, as the time difference between waveform digitisation and trigger arrival is programmable for up to 8 μs. CLAS currently uses more than 50 km of delay cables just for the ToF systems [61].

4.6 Signal Transmission

For optimal performance of the detector system, it is critical to maximise the percentage of photons produced in the scintillators that reach the SiPMs. Improving the capture cross-section and transmission of the WLS fibres is essential to this. Compared to the volume of the scintillators, the surface area of the WLS fibres is small; even if a photon enters this region, there is a limited photon capture angle for transmission. To improve the chances of capture, each of the tiles is coated in three layers of highly reflective TiO_2 scintillator paint, with a reflectivity of $\sim 96\%$ in the spectrum of photon wavelengths produced by the tiles. This ensures that many passes of the photons are possible before entering the fibres. The ends of the fibres are mirrored, using the same material, to ensure that photons that were captured by the fibre, but not in the transmission direction of the fibre, are reflected back up the fibre towards the SiPMs.

TiO_2 paint was selected for its consistency and ease of application across the 232 tiles and 784 fibres, as well as its high reflectivity.(After extensive testing, other candidate materials, such as PTFE or Tyvek®, with theoretically higher reflective indices proved either inconsistent or impractical to apply to the geometry and volume of tiles and fibres).

Another critical element to signal strength is the quality of transmission of light, both within and between material boundaries. This requires maximising attenuation length in the materials, minimising air gaps and transitions, while ensuring that those which exist occur between materials of similar refractive indices. The quality and consistency of the application of optical cement used between the tiles and fibres, the fusion splice, and the precision junction between

the optical fibres and the SiPMs are all critical points for transmission.

4.7 Light Sealing

A signal of great amplitude is of limited use, unless outside sources of noise can be minimised. The critical elements to this are sealing the detector system from outside sources of light and isolating the channels from each other in order to minimise crosstalk between elements. The entire detector is designed with these twin considerations in mind.

The reflective coatings around the detector elements help maximise transmission while simultaneously minimising possible crosstalk. Similar principles follow for the optical fibres, where bend radii are kept above minimum thresholds to increase transmission and reduce crosstalk.

Points of intersection between different elements of the detector, such as the fishtail connector lids, are designed with recesses,in order to provide secure connections between components, but also to maximise the length of light path required to pass through, forcing light to reflect from multiple matt black surfaces to enter. This reduces the amount of light that passes through any gap.

Most of the surfaces of the detector are made in black, both for low transmission and beneficial absorptivity properties. Where possible, multiple precautions are engineered into the design of components, to minimise the effect of external light sources. For example, when groups of fibres pass between the head of the detector and the electronics, they are sealed in protective lightproof black PVC sheeting and further sealed by a surrounding layer of tedlar sheeting, which encompasses all the fibre bundles, creating a seamless join between the delta wing of the detector and the entrance to the fishtail connectors.

4.8 Summary

The FT-Hodo is a double layered fast timing detector capable of discriminating between photons and electrons with sub nanosecond timing resolution and $> 99\%$ acceptance. The detector uses plastic scintillator tiles read out by WLS fibres, which are in turn fusion spliced to clear plastic fibres. These fibres transport

the light over 6 m outside the region of high radiative flux, to be read out by SiPMs connected to FADCs for data acquisition. The SiPMs are sensitive to single photon signals with very high gain and with excellent signal-background discrimination. The two-layered design allows for a thick layer for good timing resolution and a thin layer for excellent background rejection.

The main head of the detector system, comprising 232 segmented detector elements and 784 fibres, fits into a volume with a radius of 330 mm and a depth of 38 mm. Fibres exit the system through a delta wing structure at the bottom of the detector, which acts to align, support and seal the fibres from the outside environment. In order to achieve the design requirements of the system and accommodate the detector in such a tight volume, every element of the detector system has had to be carefully designed, extensively tested and optimised.

The next chapter covers the simulations which were undertaken as part of the proposal for this project, before my PhD began; these shaped the initial designs of the detector.

Chapter 5

Simulations

Two GEANT4 based simulations of the Hodoscope were developed in 2011 by Derek Glazier at the University of Edinburgh. The first modelled individual tile and fibre combinations in the Hodoscope and the transport of photons through these to the SiPMs. Using this simulation, the dimensions, configurations and properties of the tiles and fibres could be adjusted to optimise the design of the system. The second simulation modelled the operation of the entire detector, in conjunction with the calorimeter, to assess their performance working together. Details of the results from the first simulation will be discussed in this section, with further details available in [61].

The first simulation determined the energy deposited in the crystals using standard GEANT4 physics models, with the properties of the components used (light output, reflectivity, refractive index, etc) inserted, to model realistically the detector element design.

The validity of the simulation was checked by using the same physics models to simulate the CLAS inner calorimeter Hodoscope, the output of which is shown in Figure 5.1 for a MIP, producing a peak of $\sim$18 photoelectrons. This correlated well with the performance delivered by the actual detector system.

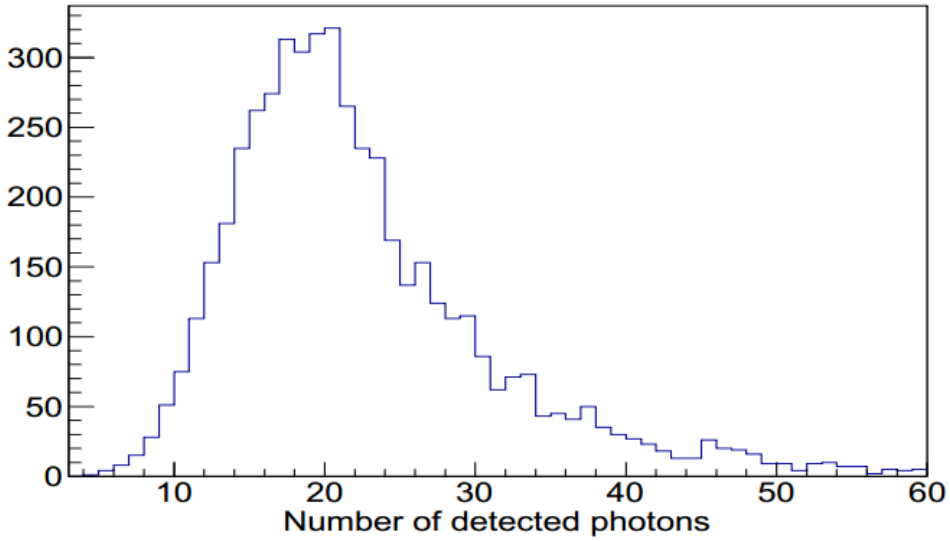

Figure 5.1 *Sample results from a validation simulation of the photon output of a MIP in the CLAS Inner Calorimeter Hodoscope. The results matched well with the performance of the detector system [61].*

5.1 Tile Thickness

The amount of energy deposited in a tile by a MIP is proportional to its path length when passing through the scintillator. A thicker tile will result in more photons being released, but only a proportion of these will be trapped by the optical fibres. The effect of changing the thickness of the tiles and varying both the number and diameter of optical fibres was simulated; the results of this are shown in Figure 5.2. It should be noted that the simulations modelled fibre channels parallel to the surface, rather than the diagonally drilled channels used in the final detector design.

The results show a strong correlation between the number of photons outputted and increasing both tile thickness and the number of fibres, for both 15x15 mm and 30x30 mm tiles. However, there is limited space available for both scintillator and tile routeing, so limits must be placed on both. The simulations showed a clear advantage of utilising four 1 mm diameter fibres over one larger 2 mm diameter fibre for a 30x30 mm tile, which would occupy a similar volume within the detector.

The simulations indicated that the geometry of the P15 tiles would outperform the larger P30 tiles. A two-fibre P15 outperforms a four-fibre P30 at all thicknesses simulated, although the gap closes with increasing tile thickness. However, four

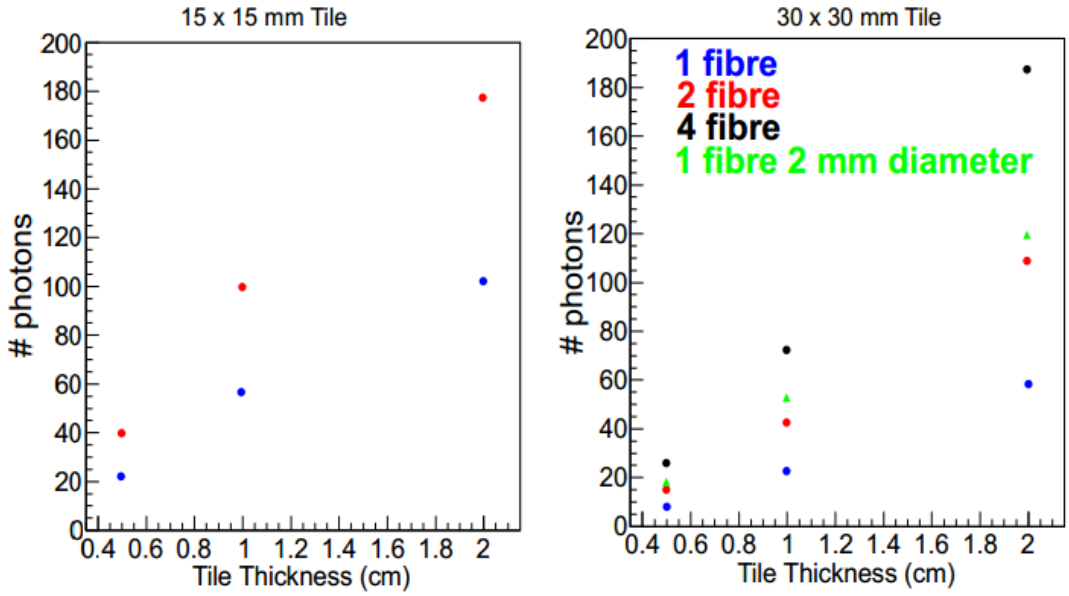

Figure 5.2 *Simulations of the variation in the photon output of detector tiles with changing thickness and different configurations of output fibres [61].*

Tile Type	Thickness [mm]	Expected Photons
P15	7	70
	15	150
P30	7	55
	15	120

Table 5.1 *Summary of the expected photon output of the detector tile dimensions selected for use in the Hodoscope.*

P15s with two fibres would require twice as many fibres for the same coverage as one P30 with four fibres. In addition, using smaller tiles would result in a lower acceptance for the detector, with additional space required for reflective materials and unavoidable air gaps between the scintillators. A compromise utilising both designs was selected, with a band of P15 tiles occupying the region of highest flux at the centre of the detector and the majority of the acceptance covered by the larger P30 tiles. A summary of the simulation results for the performance of the selected tile thicknesses for the two layers of the detector is shown in Table 5.1.

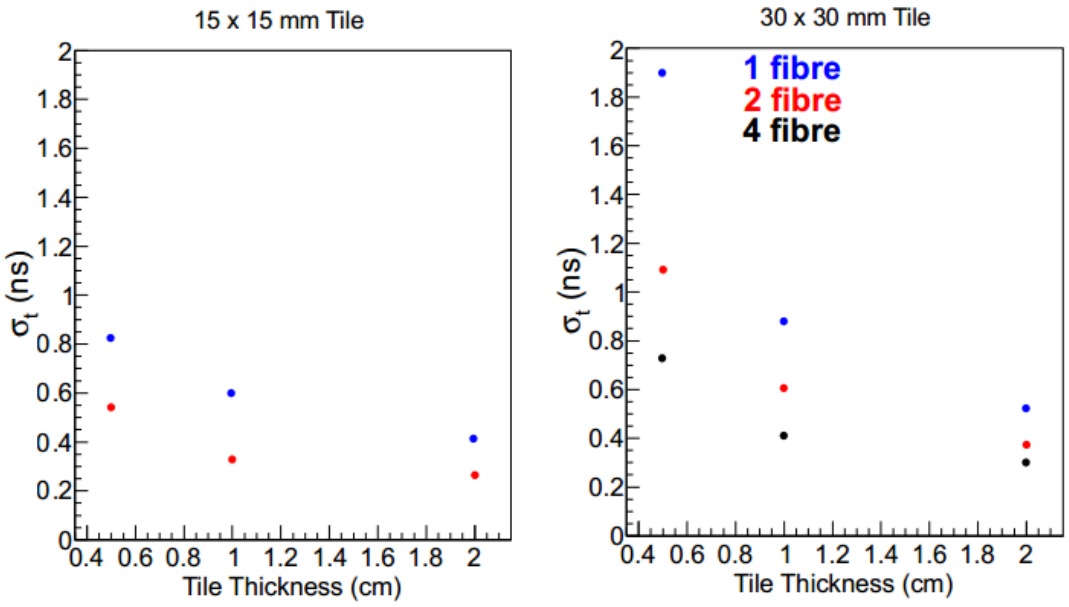

Figure 5.3 *Results showing how the timing resolution of detector elements varies with thickness and different output fibre combinations [61].*

5.2 Timing Resolution

Following a similar format to the results for tile thickness, the results for timing resolution are shown in Figure 5.3.

The critical point to notice is that increasing the number of photons collected improves the timing resolution of the detector elements. The absolute rate of improvement is most significant at lower levels of photon collection, but the effect continues throughout the range of thickness tested in these simulations. This is likely a geometric affect related to the probability that the photons produced in the scintillator are quickly captured by the optical fibres. The results indicated that sub nanosecond timing resolution is achievable for the detector element design, and 0.5 ps levels of timing could be achieved with photon output levels of ∼55 photoelectrons. A summary of results for the tile dimensions used in the construction of the detector is shown in Table 5.2.

5.2.1 Fibre Bending

Light losses due to the bend radius of fibres, both within the Hodoscope enclosure and while routeing through CLAS12, were also simulated as part of these tests,

Tile Type	Thickness [mm]	Expected Photons	Timing Resolution [ns]
P15	7	70	0.40
	15	150	0.30
P30	7	55	0.50
	15	120	0.35

Table 5.2 *Summary of the expected timing resolution of the detector tile dimensions selected for use in the Hodoscope.*

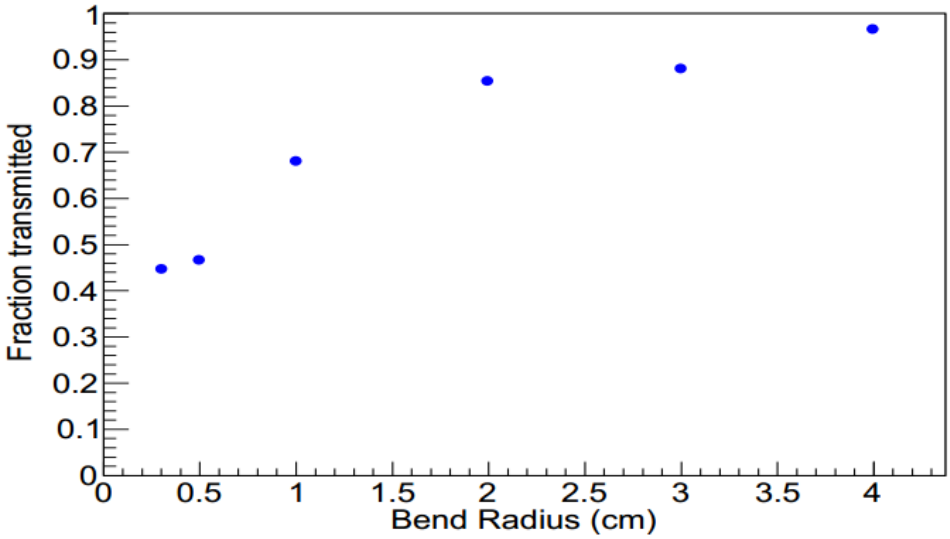

Figure 5.4 *Results of a simulation measuring the fraction of light lost in wavelength shifting fibres at different bend radii [61].*

the results of which are shown in Figure 5.4. The results matched closely with the performance specified by the manufacturer of the fibres Kuraray. In terms of the design of the detector, the results suggested that the bend radius should be limited to no less than 2 cm (ideally higher), in order to minimize light losses during transport.

5.3 Radiation Dose

In addition to the light transport simulations, a further study to determine the radiation exposure of the Hodoscope was carried out by INFN Genoa. This study aimed to determine the dose to which different elements of the Hodoscope would

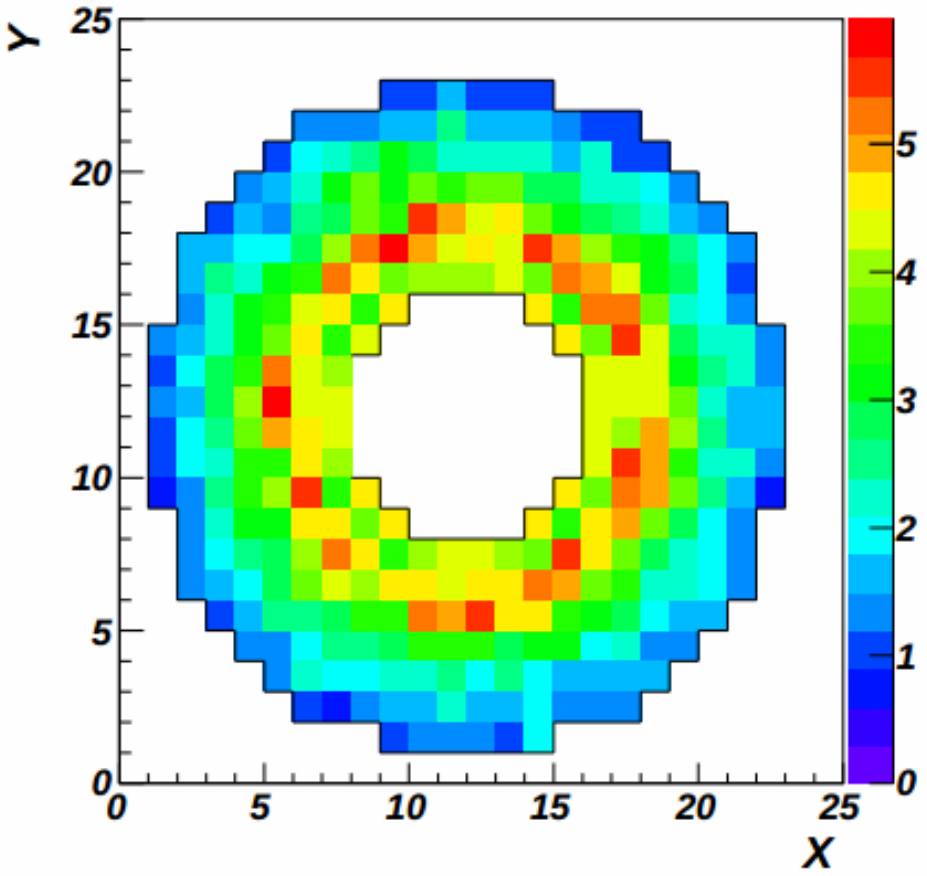

Figure 5.5 *Results from a simulation of the radiation dose experienced by the FT-Cal crystals in rad/h at a luminosity of* 10^{35} $cm^{-2}s^{-1}$. *Maximum values of just over 5 rad/h were obtained for some of the inner crystals, although averaged over each crystal in the Hodoscope this represents a peak of 3.8 rad/h [61].*

be exposed, in order to ensure that they would be suitably resistant, and that their performance would not degrade significantly over the lifetime of the detector.

The simulations indicated that without the Møller electron shield in place, the largest dose would be incurred by the inner pixels of the detector at a rate of 3.8 rad/h. Figure 5.5 shows a plot from the INFN simulation, with each pixel representing one of the 15x15 mm tiles in the calorimeter, which is positioned directly behind the Hodoscope.

Taking the average element value of 3.8 rad/h, and considering this to be the dose for all elements across the Hodoscope, produces an annual dose of 33 krad for each crystal. A large number of studies have shown that exposure to radiation can change the properties of plastic scintillators, reducing the light yield and therefore

the timing resolution of the tiles. Similar effects have been shown to occur in wavelength shifting fibres and optical cements, reducing their transparency and increasing attenuation length, thus lowering the performance of the materials. However, most studies are carried out at radiation doses far higher than those expected to be incident on the Hodoscope, considering doses in the 1-10 mrad range delivered over a period of hours rather than years [76, 77]. The components selected have been shown to be radiation hard well beyond the long-term doses applied to the Hodoscope, so this is not expected to be a problem for the detector system.

5.4 Summary

GEANT4 based simulations were carried out to determine the viability of the initial designs of the Hodoscope, simulating both the process of photon transport through the detector and the radiation dose incurred by the different elements of the detector system over the lifetime of the project. The results of these simulations indicated that the best compromise for the system design utilised a layer of 30x30x15 mm tiles tiles, read out by four 1 mm diameter fibres for the majority of the detector system. This was complemented by a ring of 15x15x15 mm tiles, for greater output and resolution in the region of higher flux close to the beamline. The simulations of radiation dose indicated that the detector system will incur an average annual dose of 33 krad, well below the tolerances of the materials selected.

The simulations described in this chapter provided evidence for the viability of the detector design and guided the direction of development. However, they were indicative only of the potential of the system; several years of development and testing were required to go from the early prototypes with minimal output to the optimised final version of the detector system.

In the next chapter, the three sets of tests that were carried out using an accelerated beam are described. These allowed prototypes of the Hodoscope to be tested in conjunction with prototypes of the FT-Cal.

Chapter 6

Beamtime

Throughout the development of the Hodoscope, many experiments have been undertaken to gather more data on the performance of different elements of the detector. Most of these were carried out using radioactive sources or cosmic rays. Both of these sources are readily available, but are both limited, either by the energy of the source or the rate of the cosmic rays. To truly test the detector's performance in an environment comparable to CLAS12 requires an accelerated beam. There have been three beam tests throughout the detector's development, the first carried out at Jefferson Lab and the following two at the Double Annular Φ Factory for Nice Experiments (DAFNE or DAΦNE) Beam Test Facility (BTF). Each one was done in conjunction with a prototype of the FT-Cal, simulating the operating environment in CLAS12. The first two tests were undertaken before the start of my PhD, but are included for completeness.

6.1 First Test: Hall B at JLAB

The first test used only a single 15x15x10 mm tile, read out by 2 wavelength shifting fibres. These were set into channels cut into the surface of the tile, rather than inserted into holes.

The main aims of the test were to provide an initial proof-of-principle test of the equipment and to provide further information to guide the development of the detector system under beam conditions. The single Hodoscope tile was positioned in front of one of the elements of the calorimeter, to take coincidence

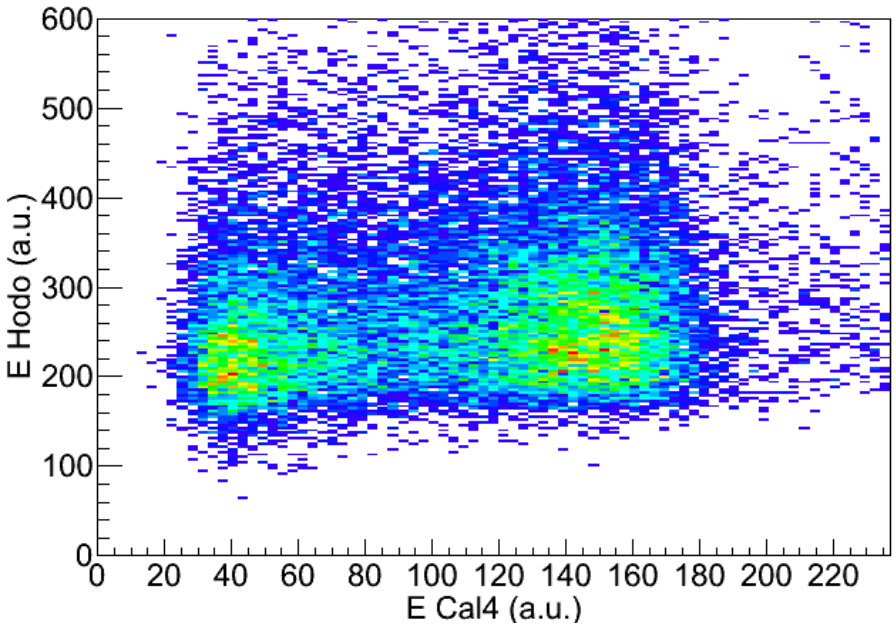

Figure 6.1 *An example of the spread of energy deposited in the test set-up in Hall B. The energy of hits in the Hodoscope vs the Calorimeter are shown (In terms of the ADC channel). The cluster on the left represents pedestal measurements while the cluster on the right shows coincident hits between the two detectors.*

measurements.

The results of the energy deposited in the Hodoscope and calorimeter tile can be plotted in 2D, to determine the spread of hits measured in the test. An example is shown in Figure 6.1, with a clear region of coincident hits measured between the two detector tiles.

This initial proof-of-principle test of a simple readout situation was a success. However, the light output and isolation of the tiles needed to be improved significantly to reach the design requirements of the system.

6.2 Second Test: BTF at DAΦNE

The following set of beam tests took place at the DAΦNE e^+e^- collider situated at the INFN Frascati National Laboratory, Frascati Italy. This facility primarily collides electrons and positrons at a centre of mass energy of 1.02 GeV in order to produce ϕ mesons which primarily decay to kaons, which are the main focus of the experiments taking place at the accelerator. The electrons in the facility are first

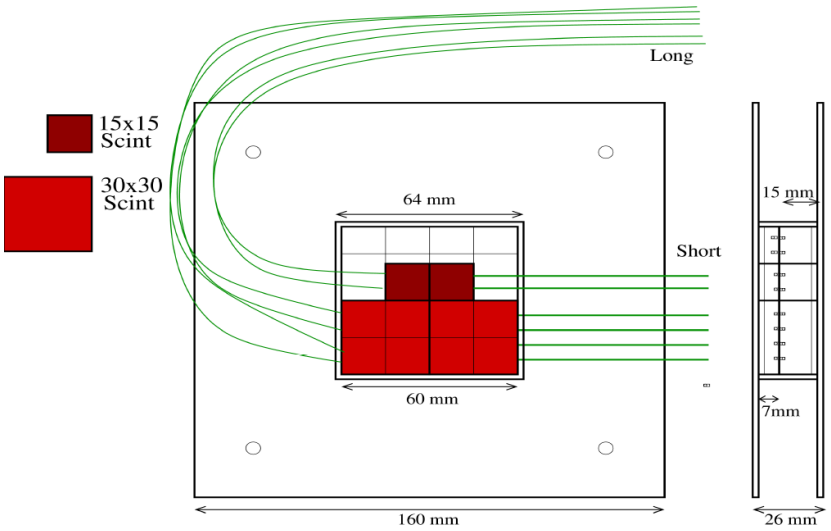

Figure 6.2 *Schematic setup for the BTF tile tests. The configuration shown with the beamline directed into the page with the calorimeter positioned downstream of the prototype Hodoscope.*

accelerated by a LINAC to 510 MeV before being injected into the accumulator. However, when injection is not taking place, the beamline can be delivered to a beam test area (BTF) [78]. The BTF facility is capable of delivering beam for a wide range of energies and is mainly used for calibration experiments.

The main purpose was to test a range of Hodoscope elements at the same time, in coincidence with multiple calorimeter elements. A total of eight tiles were prepared: four larger P30 tiles and four smaller P15 tiles, with an even split between thick (15 mm) and thin (7 mm) tiles. The elements prepared used early designs for reflective materials, optical connections and electronics, with eight Hodoscope channels being read out simultaneously.

The tiles under test were positioned in two layers, with two wider P30 and two smaller P15 tiles used in each layer, with the thicker tiles mounted behind the thinner layer. Each tile was aligned with corresponding elements in the prototype calorimeter for coincidence measurements during the experiment. For ease of readout while minimising attenuation, some fibres were connected using shorter ($\sim$ 0.2 m) and other longer ($\sim$ 1 m) fibres. A simple diagram of the set-up is shown in Figure 6.2.

The results of the tests were successful, taking data from the eight tiles simultaneously in coincidence with the calorimeter. However, there were clear problems with both the overall output of the tiles and the consistency of results between them. An example of these is shown in Figure 6.3.

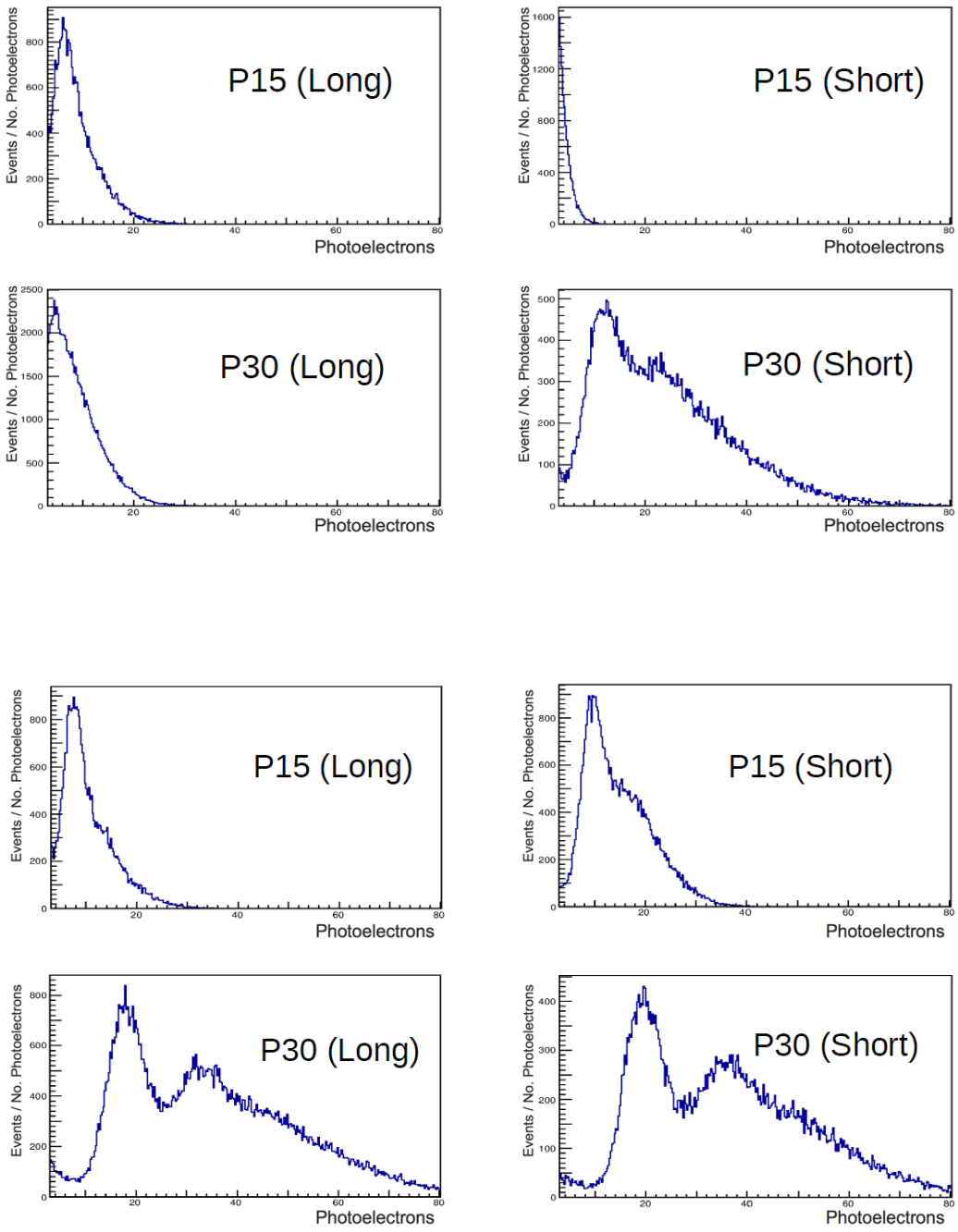

Figure 6.3 *Sample results from the first tests run at the BTF (x-axis units are photoelectrons). Results are shown for the 4 thin tiles (Top four frames) and the 4 thick tiles (Bottom four frames). Results for both single and double electron bunches can be clearly seen, most obviously for the P30 thick tiles.*

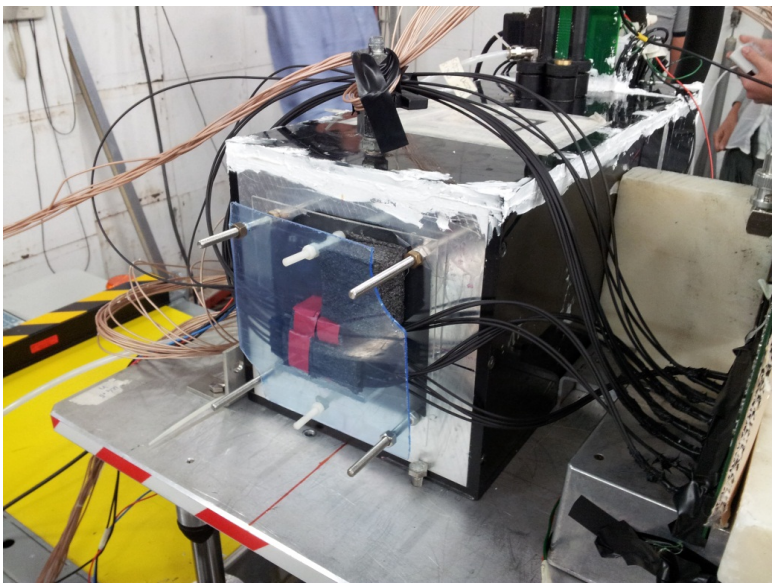

Figure 6.4 *The prototype configuration in situ in Frascati, prior to the start of the beamtime.*

The results obtained were well below the expectations from the simulations. However, during the tests it was found that some of the tiles experienced both poor and inconsistent optical connections, both $tile \rightarrow fibre$ and $fibre \rightarrow SiPM$. Attempts were made to adjust these during the tests, but more fundamental adjustments to the design were required to resolve some of these problems. The strongest performing tiles were the P30 thick tiles, which averaged ∼18 photoelectrons for a MIP.

6.3 Third Test: BTF at DAΦNE

A second set of beam studies at DAΦNE was carried out on a prototype Hodoscope detector in November 2012. A similar detector configuration was utilised as at the previous test, see Figure 6.4. However, the focus was placed on improving the optical output of the tiles to demonstrate the viability of the detector design. A variety of new tiles was tested, including some trialled at the previous round of testing. I designed and implemented improvements to the reflective wrapping of the tiles and optical isolation of the elements. I also developed significant improvements in the quality of the optical connections tiles-fibres and fibres-SiPMs; each group of fibres was glued into a SiPM connector, before being polished, using a series of refining grades of optical sandpaper, in order to ensure a clean optical connection to the SiPMs.

Tile	Thickness [mm]	Fibre Length [m]	Source	Photoelectrons
P30Thin	7	0.2	Eljen*	37 ± 6
P30Thin	7	1.0	Eljen*	28 ± 5
P15Thin	7	0.2	Eljen*	23 ± 5
P15Thin	7	1.0	Eljen*	19 ± 4
P30Thick	15	0.2	NE	78 ± 9
P30Thick	15	1.0	NE	35 ± 6
P15Thick	15	0.2	Eljen	29 ± 5
P15Thick	15	1.0	Eljen	23 ± 5
P30Thick	15	0.2	Eljen	46 ± 7

Table 6.1 *Summary of tile performance during the second set of tests at BTF. Tiles marked with a * were also tested at the previous beamtime at BTF, but now with upgraded fibre→SiPM connections.*

Nine different tiles were tested during the beamtime, with the P30 thick tiles being switched between runs, the results are summarised in Table 6.1. The overall performance of the tiles increased significantly from the results obtained at the previous test, with the best performing tile peaking at just under 80 photoelectrons, shown in Figure 6.5. However, the results were still not consistent across size, thickness and fibre length and the majority of tiles were still performing below the potential indicated by simulations. This set of results was promising and demonstrated that some tiles are able reach the level of output required for suitable timing resolution of the detector. Further studies were needed in order to allow every detector element to reach the same peak performance.

6.4 Summary

During the course of the FT-Hodo's development, prototypes of the detector system underwent three separate beamtests, in order to evaluate the detectors performance under conditions similar to those in CLAS12. The first was undertaken in Hall B at Jefferson Lab and was a proof-of-concept test, to evaluate the viability of the design. This was successful, but the prototypes performance was not as high as required for the final detector. The second test focused

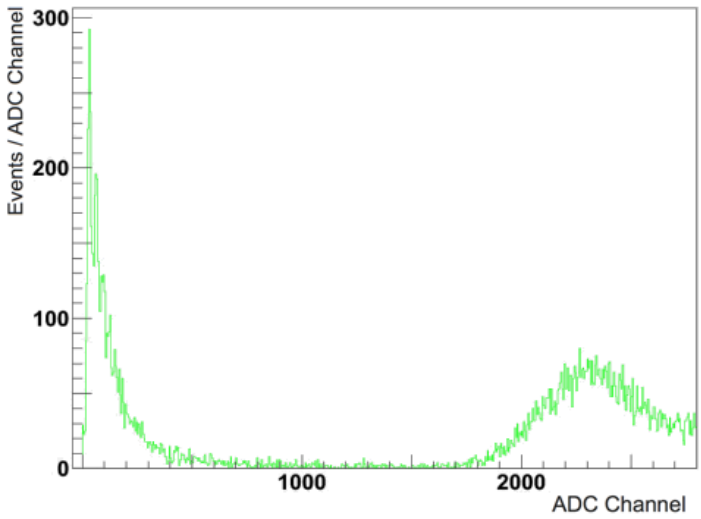

Figure 6.5 *A plot of the strongest performing tile from the second set of tests at BTF. A peak approximating the shape of a Landau distribution (expected of a MIP) is observed peaking around channel 2350 in the ADC. The peak is well separated from the thermal noise across almost the full range of the ADC, peaking at an energy equivalent to just below 80 photoelectrons.*

on the operation of the multiple detector elements simultaneously, working in conjunction with a prototype of the FT-Cal. Extensive data was acquired from the test, collecting results from multiple elements simultaneously, thus achieving the goals of the run. However, again the individual elements performance was inconsistent and well below expectations from the simulations. The third test aimed to greatly improve the performance of the detector elements, by optimising the output of the tiles, their optical connections and isolation from sources of interference. I spent several months in the laboratory designing, testing and optimising improvements to the optical performance of the prototypes. The optical performance of the tiles in the third test was a dramatic improvement over the highest performing tile, outputting over 4 times as much light as the best performer in the previous test. However, there was still significant variation between tiles. Significant improvements to the design and implementation of the detector elements would still be required to achieve the design requirements of the detector system.

The next chapter in the thesis covers the process of constructing the FT-Hodo, discussing the techniques and design decisions made to ensure consistent high performance from the detector system.

Chapter 7

Sub-Systems, Testing and Development

In the following section, the key interconnecting elements of the detector will be discussed in more detail, highlighting some of the critical tests I carried out during their development. Additional focus will be placed on the systems with which I was most involved during my PhD.

7.1 Detector Redesign

Before going on to discuss the final designs of the detector systems and to give more context to some of the development decisions, I want to highlight a significant developmental change in the project that occurred roughly two years into my PhD. It was discovered by another working group at JLab that their original estimates for the dimensions of the new HTCC were incorrect; the pressurised gas used in the detector system would cause a greater expansion than previously expected. This left less space available for the Forward Tagger, which is situated between the HTCC and the torus support structure. A reduction in size of all elements of the Forward Tagger was necessitated, and for the Hodoscope this required a reduction in depth from 44 mm to 38 mm.

At this stage in the development process, all the scintillating tiles had already been ordered, (which make up 22 mm of the detector volume), and it was too late to change their dimensions. This left just 16 mm of space, including tolerances,

for all the detector structure and space for routeing the fibres out of the detector, for both layers of the Hodoscope. This necessitated a complete redesign of the structure and fibre routeing of the detector system, balancing the space available for each layer. Previously there had been ample tolerances, allowing for a more robust design and wider bending arcs for the fibres, but now every fraction of a mm saved was significant.

Several mm were saved by shifting to a carbon fibre based interlocking design, with all screws inset into the detector structure, to ensure no additional depth was used. Fibre routeing paths had to be redesigned to deal with reduced space and ensure no fibres had too tight a bend radius. To give an example, both layers of the detector have the same number of fibres and thus require the same minimum volume for them all to path out of the bottom of the detector. However, for the thin tiles, the exit angle of the fibres is much shallower, therefore with optimised pathing to minimise fibre density in critical areas, less volume is required above the tiles in the thin layer than the thick. Many similar decisions had to be made and at many points, compromises found, in order to ensure the detector could deliver its design aims, despite reduced dimensions. Many of the final designs discussed in this section were heavily influenced by the consequences of this change.

7.2 Plastic Scintillator Tiles

The type of plastic scintillator selected for use in the Hodoscope, doped polyvinyltoluene, was identified before I joined the project. However, the source of supply of the material and the preparation of the tiles (cutting and drilling), was still being considered.

I constructed prototypes to compare scintillator samples supplied by Rexxon and Eljen. The scintillator tiles were wrapped in aluminised Mylar for the tests, and sealed from outside sources of light with several layers of black electrical tape. The test tiles were fitted with short lengths of wavelength shifting fibres, with air connections between the tiles and fibres, and read out by SiPMs. Tile output was evaluated from a cosmic ray spectra, measured with an oscilloscope, to find the landau shaped spectra of the MIPs. With consistent set-up, tile performance is a combination of the light output of the detector tiles and quality of the optical connection to the fibres. Each supplier used a different specialist firm to drill the

channels into the SiPMs, using cooled precision drill bits for an optically smooth finish. On inspection, it appeared that the drilling technique employed on the tiles from Eljen produced a superior quality of finish, producing clear channels with few imperfections. The tiles supplied by Rexxon had obvious scratches from drilling along the length of all the fibre channels.

The final results of the tests showed similar optical performance between the tiles from the two suppliers. However, the tiles supplied by Eljen had to be tested with only two of the four fibres fully inserted, as the two outer channels were not drilled sufficiently wide to allow fibres to enter more than 3-4 mm. Therefore, if adjustment could be made to the width of outer channels on the Eljen tiles, they should provide significantly improved performance in comparison to those supplied by Rexxon. Based on the results on these tests, Eljen was selected as the supplier of the scintillator tiles, with assurances that the fibre channel dimensions would be altered for the final product. Further details on the properties on the selected scintillator can be found in [69].

7.3 Optical Fibres

The supplier of the optical fibres selected for use in the Hodoscope was also determined before the start of my PhD, as Kuraray is a trusted supplier to JLab. However, the optimal type still required further testing and investigation.

To transport light from the scintillators to the silicon photomultipliers (SiPM), a combination of wavelength shifting (WLSF) and standard plastic optical fibres is used. Photons produced in the scintillator are absorbed by a short length of WLS fibre that is inserted into the tiles. After absorption the photons are re-emitted in the ideal frequency range for detection efficiency in the SiPMs. The Y-11 fibres were selected to match the emission spectrum of the scintillators, shown in Figure 7.1. These short lengths of WLF fibre are fusion spliced to 6 m of clear optical fibre, of matching refractive index, producing a juncture with less than 2% signal loss. The photons have a much longer attenuation length in the clear fibres, minimising the signal loss before reaching the SiPMs. The absorption and emission spectra for Y-11 fibres used in the Hodoscope are shown in Figure 7.2.

Double clad S-type wavelength shifting fibres were selected for use in the Hodoscope, for the best combination of photon transmission and resilience to

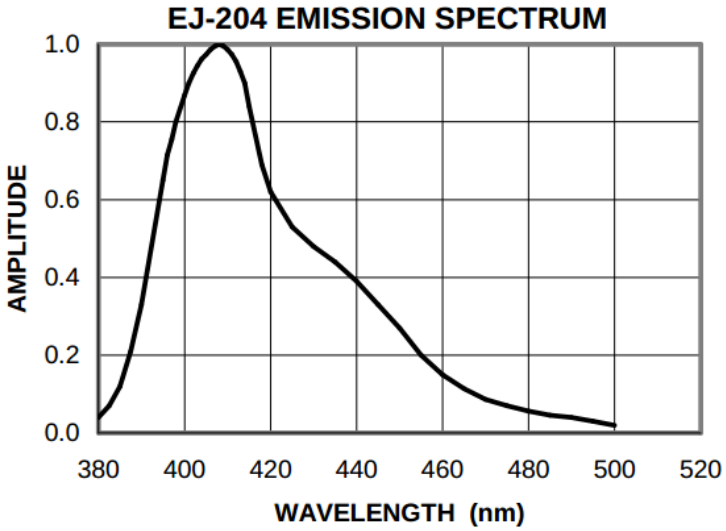

Figure 7.1 *The emission spectrum of EJ-204 plastic scintillator. Matching the emission range of the scintillators and absorption range of the fibres is essential for effective optical transmission [69].*

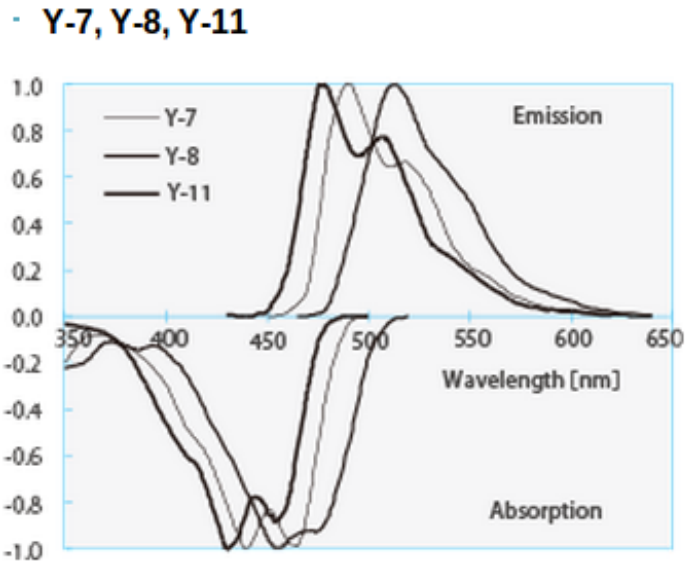

Figure 7.2 *The emission and absorption spectrum for different types of Kuraray fibres is shown. The Y-11 type was selected for the excellent match between its absorption range and the emission spectrum of the scintillator, and its ideal emission spectra for the quantum efficiency of the SiPMs [70].*

tight fibre bend radii. S-type fibres have improved transmission at bend radii of the order of 2 cm, at the cost of some attenuation length; however, as only 10 cm of WLSF is used before the fusion splice, the increased attenuation of the

fibre type is minimised. The improved transmission with tighter bend radii is of particular significance within the Hodoscope itself, because there is very little space for the fibres to route through. This issue became much more significant after the redesign to the detector system, where its depth was compressed from 44 mm to 38 mm. This required the fibres exiting the tiles to curve much more rapidly, in order to fit within the space above the tiles. For further details on the WLS and clear fibres used see: [70, 72].

After the reduction of volume of the detector system, it was critical to test the transmission of the WLSF with tighter bend radii. Based on the Kuraray fibre datasheets, there is a significant fall-off in fibre transmission below a critical threshold; above this, transmission drops only gradually with smaller radii of curvatures.

I carried out tests to measure these experimentally, utilising a 'dark box' designed to be sealed from outside sources of light. The tests utilised several detector tiles with $\sim$ 40 cm lengths of WLSF glued into the tiles. The tiles were set in fixed positions and the fibres set up with varying bend radii, going through a 180° bend before being read out by SiPMs, connected to a high performance oscilloscope. Tests were carried out using both Sr^{90} and Bi^{207} sources, both dominantly β emitters with a range of peak energy emissions. The amplitude spectrum of the SiPMs was recorded for each bend radii measured, starting with wide arcs and progressing down to radii smaller than the tightest undergone by fibres in the Hodoscope. The results of these tests indicated that there was gradual reduction in signal transmission as the bend radii of the fibres are reduced, but significant light losses began to occur only at half the minimum radii used in the Hodoscope enclosure. This provided confidence that losses due to the bend radii of fibres would be minimal in the Hodoscope.

7.4 Reflective materials

High performance reflective materials are critical for optimising the optical properties of the detector. The material used to surround the scintillating tile elements requires the following properties:

- High co-efficient of reflectivity
- Consistent performance across tiles

- Minimal thickness
- Radiation hard

These qualities are required to maximise the light collection of the wavelength shifting fibres, improving the timing resolution of the detector. It allows them to provide consistent performance across individual elements and also over the lifetime of the detector, and finally, to optically isolate each element, ensuring there is no potential for crosstalk, thus minimising the effect of any light leaks into the system.

A high coefficient of reflectivity is critical, to keep photons produced through scintillation inside the detector elements. This also provides additional opportunities for photons which are not quickly captured by the wavelength shifting fibres to reflect off the surfaces and be collected by the fibres. The coefficient of reflectivity for a material is a function of the wavelength of light that it encounters. In this case, the critical range is the emission spectrum of EJ-204, shown in Figure 7.1, which ranges between 380 nm and 500 nm, peaking at around 410 nm. The higher the coefficient of the material across the active range of the material, the higher the potential light yield from the tile. The reflection coefficient at varying wavelengths for several widely used reflectors is shown in Figure 7.3.

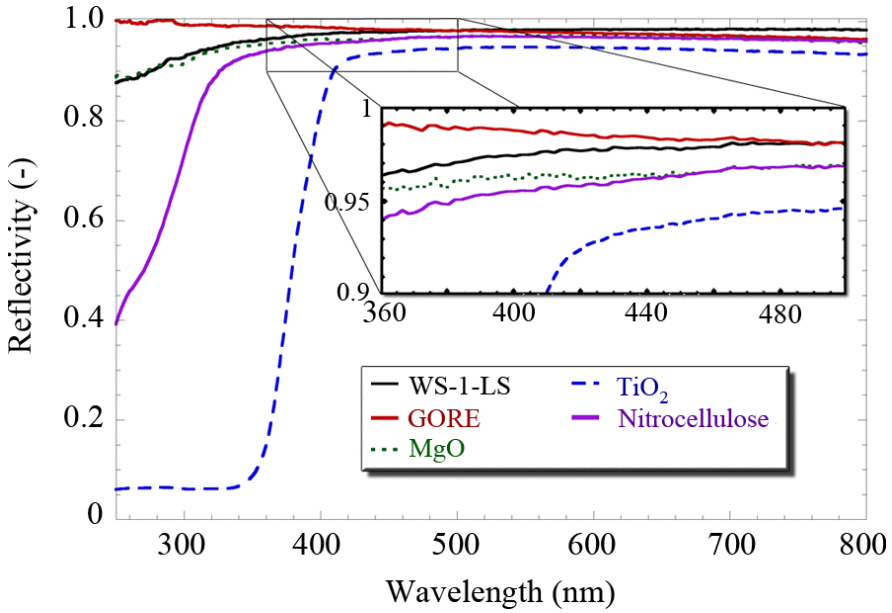

Figure 7.3 *Reflection coefficient for several reflectors, including TiO_2 as a function of wavelength [79].*

Consistency of response to an incoming charged particle is very important in a highly segmented detector such as the Hodoscope, if results from different

elements are to be interpreted together. The reflective material itself must be consistent in both its response to photons and in its connection to the detector elements. It must be able to be moulded with precision to the shape of the detector blocks, without uneven surfaces or air gaps, and maintain its shape over the lifetime of the detector, under the harsh radiation of the beamline. A material which may theoretically be superior in an idealised situation may not perform consistently when applied over many different elements. As a result, systematic testing is required to ensure materials fulfil the design requirement; ease of application becomes an essential factor.

One of the typical disadvantages of segmented detectors is a reduction in the active area of acceptance because of gaps between elements. To keep this reduction to a minimum, the tiles need to be of a uniform size which will tessellate with minimal area covered by non-active materials. Therefore, the ideal reflector is formed of a vanishingly thin layer of material; however, the reflectivity of a material is also dependent on its thickness, with multiple layers improving the coefficient of reflectivity. In addition, with minimal thickness comes fragility and often inconsistency. A balance between these factors is required.

During operation, the detector and its reflective elements will be subjected to significant levels of radiation, with a typical flux of 3.8 rads/h. The reflective materials need to maintain their performance above design requirements, without significant degradation over the lifetime of the detector. Replacement of the material during its lifetime will not be possible, without substituting the complete detector element and possibly causing further problems with nearby elements. Only materials known to be radiation hard under these conditions were considered for use in the detector.

Considering only materials which fulfilled the previously discussed criteria, sample tiles were prepared with the reflectors shown in table 7.1. For each material, I carried out tests using several samples of both P30 thin and P30 thick tiles, checking for consistency of results and any effects of the varying geometry. Tests also provided experience of the difficulty associated with preparing the tiles with each reflector. Considering that batch production would be required for the final system, in order to limit the possible variance of optical connections between the tile and the SiPMs a simple air connection between the fibre and the tile was used, which allowed the rest of the test configuration to be maintained constant for all tests. Tests were carried out using both Sr^{90} and Bi^{207} sources, both dominantly β emitters with a range of peak energy emissions. Although data collected

Reflector	Reflection Coefficient @440 nm	Thickness [mm]	Reference
Titanium Dioxide Paint	0.955	0.14-0.18	[79]
PTFE Tape	0.99	n x 0.08	[79]
Tyvek® Paper	0.97	n x 0.11	[80]
Aluminium Foil	0.78	0.025	[80]

Table 7.1 *Properties of reflectors selected for testing on prototype detector elements.*

utilising cosmic rays would provide a more precise measure of photon output, tests conducted using sources can be completed much more quickly, with statistically significant results. The trigger frequency for each tile-reflector configuration was measured for series of discriminator values to ascertain a frequency spectrum for each combination.

Of the materials tested both PTFE and titanium dioxide paint performed strongly, with the highest mean output of light and they maintained this level consistently across multiple detector tiles. The aluminium foil performed consistently, but did not generate the same signal strength as the top performers. Tiles wrapped in Tyvek® performed very inconsistently; this was probably a result of the difficulty applying and attaching the material consistently to the shape of the element volume.

Taking into account research from literature and tests carried out on tiles [79, 80], titanium dioxide paint was selected as the material which best satisfied the demands required, with a high reflective index, consistent results and ease of application; more specifically BC-620 was used [81]. The PTFE was both thin and highly reflective, but the difficulty in wrapping the tiles with their projecting fibres in a consistent manner, was a major drawback of this choice of reflector. A combination approach applying PTFE to most of the tile and covering the awkward areas with titanium dioxide paint was also considered, but discarded, as PTFE did not significant outperform the BC-620 paint in the tests carried out.

7.4.1 Mirroring the Scintillator End of the Fibres

Wavelength shifting fibres operate by absorbing a photon before remitting it in a new frequency range. For this photon to be captured and transmitted down the length of the fibre, it needs to be produced in a narrow emission range of a few degrees. The vector of re-emission is not dependent on the angle of incidence of the original photon. As a consequence, mirroring the scintillator end of the fibre gives the potential for the angle of acceptance for capturing the photon within the fibre to be almost doubled. This comes at the cost of blocking any photons that may have entered through the end of the fibre, but for a fibre of any significant length within a tile, the benefits outweigh the downsides.

The ideal reflector for this purpose shares many of the same characteristics as for the scintillators, but it also has to attach to the end of a fibre that is inserted into a narrow channel. In order to be effective, the reflector needs to fully cover the end of the fibre, particularly as the multi-layered design of the fibres results in the majority of light being transported in a narrow region near the edge of the fibre. However, if it is fractionally larger than the fibre it will not fit, causing damage or becoming damaged when placed into the channel. In most examples in the literature, such as the study done by Joram [82], the mirrored fibres were placed in flat channels which pass all the way across the scintillator, where there was easy access to the ends of the fibres. However, the design of the Hodoscope restricts this access, and the results of tests I carried out using a more idealised reflector, such as thin discs of aluminised Mylar, were inconsistent. In addition, it proved extremely difficult to position and attach discs of Mylar precisely to the ends of a polished single fibre, even after I tried several alternative approaches to the task. After these tests, the titanium dioxide paint used as the reflector on the scintillators was considered, along with aluminium sputter deposition, which would deposit a thin layer of aluminium directly onto the fibres. Initially TiO_2 paint was tested and provided more than a 50% increase in photoelectron yield, in comparison to unpainted fibres. The material was easy to apply and results were consistent across the limited sample of tiles tested. After these successful tests the costs of carrying out sputter sputter disposition on 800 fibres was deemed excessive compared to the potential benefits of the technique. Therefore TiO_2 paint was selected as the material TiO_2 for this task.

7.5 Supporting Structure

The design of the detectors structure has undergone many changes throughout its development, most dramatically after the changes to the volume available. Throughout my PhD, I have been actively involved with the development of the structural design, whether this was through testing prototypes, or providing detailed feedback at the University of Edinburgh to the mechanical workshop and other technical staff, who were responsible for constructing the different elements of the structure. Only the final version of these components is discussed in this section, but this version was the result of many months of development time.

The superstructure of the detector supports the scintillator tiles and fibres and ensures that they are isolated from sources of background noise, such as ambient light in the detector hall. This structure must be rigid and robust, whilst being composed of materials with low density, in order to minimise scattering effects. There are also strict limitations on dimensions, as the detector system must fit into a limited volume and maximise the space available for all the detector elements.

The detector itself is split into two interlocking units which house the respective 7 mm and 15 mm thick detector elements. The units can be removed from each other for maintenance and future applications, but while in situ at CLAS12 the layers will form a single detector. Each layer is composed of a top and bottom plate of 0.5 mm thick black carbon fibre. These are spaced by a series of PEEK columns around the edge of each plate, which act to support and maintain the rigidity of the structure. At the centre there is a collar made of PEEK that fixes into the support structure which positions the detector on to the supporting beampipe. The thin sheets of carbon fibre are extremely strong in the direction of the fibre weave along the plate, but are very fragile in response to a transverse force. The other support structures support the transverse load. The spacers and the collar also act as an anchor to lock the two sections of the Hodoscope body together, through nylon screws that pass from one layer to the other. At the base of the plates is a delta wing, which channels the fibres out of the main body of the detector and into the support structure beyond. Surrounding the outside edge of the detector, covering the area between the four carbon fibre layers, is a curved belt of flexible plastic, with grooves for the plates to fit into. This attaches to the detector through nylon screws which run through the belt and into the spacers around the edge of the detector volume. Prototypes were constructed to ensure

the design provided the structural rigidity and strength needed to support the mass of the detector system. Thorough testing on these demonstrated the design could easily cope with the forces that could potentially be applied to the system.

7.5.1 Fibre Delta Wing

The fibre Delta Wing is the exit point of the optical fibres from the detector body. It acts to channel the fibres into the limited space available for their passage. It also holds the fibres' protective PVC sheaths in place, spreading the load of the fibre bundle across the detector structure. As the main exit point from the head of detector, it is essential that the component can maintain the light seal required of the detector structure, while providing a smooth path for the fibres out of the detector.

The Delta Wing is constructed from four main components, two 3D printed connectors, one for each side of the Hodoscope, and two carbon fibre lids, which are screwed into place, helping to seal the system from outside sources of light. The two connectors fit smoothly into one another and their depth varies across the length of the component. This is to minimise the stress put on to the fibres as they transition out from the two different sides of the Hodoscope. The two pieces are held together and connected to the carbon fibre plates of the detector by nylon screws, adding to the rigidity and improving the structural integrity of the detector system. Within each connector, there is minimal structure, in order to maximise the space available for the routeing of the fibres. Each connector is mirrored down the centre line of the component and provides routeing for 12 stacks of 4 bundles of fibres. Under each stack are situated two sets of indented holes, which contain flexible ties which can pass around four fibre bundles and fix them in place. The sets of holes are staggered across the width of the connection, so that the extra space required for the ties is spread along the length of the connector.

The routeing of each fibre bundle was designed to optimise the light transport of the fibres, and to minimise the stress placed on each component and any overlap between fibres in the Hodoscope. Inside the Delta Wing, the fibres pass in groups of four into protective black PVC tubing with an internal diameter of 3.0 mm and a wall thickness of 0.3 mm, which isolates each group, protecting it from damage and sealing it from outside sources of light. The protected bundles are tightly packed, filling almost the entire internal volume of the delta wing. This adds an

additional layer of protection for the light seal between the scintillator tiles and any sources of light outside the detector volume.

7.5.2 Fishtail Fibre-SiPM Connector

The 'fishtail' connectors create a sealed juncture between the optical fibres and the silicon photomultipliers. They act to guide the fibres precisely into position and maintain their optical isolation from the external environment. The connectors are 3D printed to create a consistent precise design to interface with all 30 groups of SiPMs. The fishtail connector is composed of three components: firstly the main body, comprising most of the length of the connector, which takes in the appropriate fibres separating from the main transport bundle of the detector, secondly, an interlocking end piece, which interfaces with the electronics board and into which the fibre optic cables are glued, and finally, a lipped lid which seals the construction from outside sources of noise. The fibres enter the main body through a flared opening, which narrows to a channel just wide enough for eight 3.6 mm sheaths to fit through, before curving more widely, following a similar contour to a wine bottle. The flared entrance enables a wider angle of acceptance of fibre bundles. The narrow opening helps to minimise any light leaks into the component. The widening body allows the fibres to spread out evenly and to be guided towards their respective SiPMs with a wide radius of curvature, minimising any loss of light and stress on the fibres. The fibre bundles pass through the main body, still encased in their protective casing, up to their juncture with a recess into the end piece of the connector, maintaining isolation of the fibre optics.

The connector positions each fibre less than 1 mm away from the SiPMs, with an even spread across the surface area of each detector. This alignment maximises the potential acceptance of the detector, spreading the light across the pixels of the SiPM. Another important property is that both the separation distance and spread of the fibres is consistent across different channels, to allow proper calibration of the detector system.

7.5.3 Electronics Enclosure

The electronics enclosure is designed to house the electronics rack where all the mezzanine and pre-amplifier boards are situated, along with the control board. The enclosure's main purposes are to give protection from outside sources of light and also to provide lightweight and robust containment for the electronic modules, both in transit and in situ. Additional space is allocated above and below the electronics rack for sets of fans, which passing air over the electronic boards to reduce thermally induced dark current in the system. Pictures of the completed unit during testing are shown in Figure 7.4.

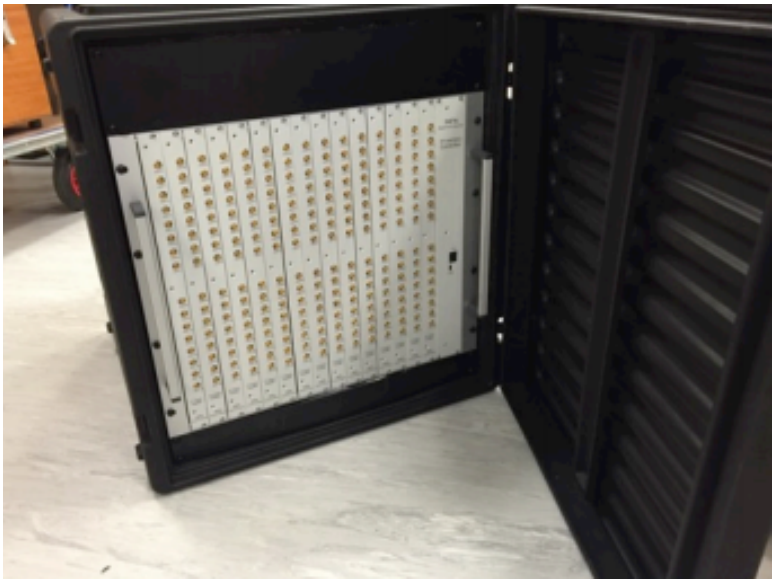

Figure 7.4 *Photograph of the rear of the electronics enclosure, where the output from the pre-amplifier boards is read out through Lemo cables.*

7.6 Silicon Photomultipliers

Silicon photomultipliers (SiPM) are highly sensitive radiation detectors with high efficiency and potential for very precise timing resolution. They are designed to trigger on single photons of light with high efficiency, producing a signal with high gain and very low time jitter of less than 100 ps. They are designed to be highly segmented, allowing many photons to be detected simultaneously, with each element isolated from one another to avoid unnecessary background noise and produce highly precise clean signals.

SiPMs consist of a matrix of highly sensitive micro cells (pixels) all connected

in parallel. Each one is composed of a Geiger-Mode avalanche photon diode (GM-APD) connected to a resistor for passive quenching, see Figure 7.5. When operating above a breakdown voltage, (that is dependent on the particular SiPM, but is ~ 65 V in those used in the hodoscope) the diode rapidly discharges, once triggered by a photon or another source of noise, producing a signal with a high gain; then the resistor acts to quench the discharge and the cell will switch to a recovery mode, where the capacitor in the diode is recharged ready to trigger again.

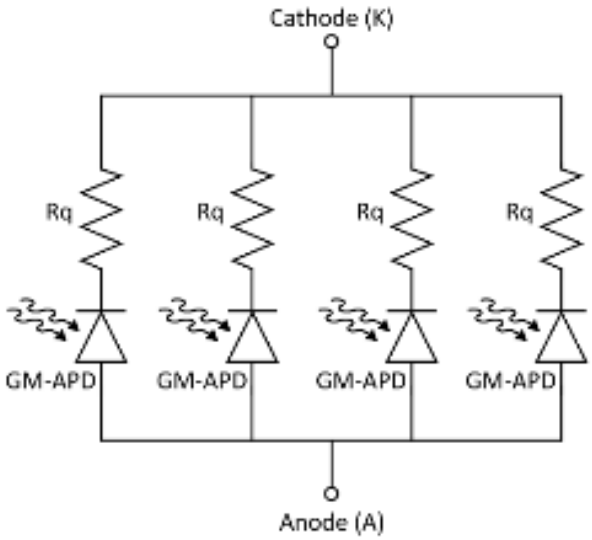

Figure 7.5 *A schematic representation of the parallel arrangement of Geiger-Mode avalanche photo diodes with quenching resistors in a silicon photomultiplier [83].*

7.6.1 Photon Detection Efficiency

The probability of a pixel triggering on the arrival of an incoming photon to the SiPM is known as the photon detection efficiency (PDE). This is defined as a product of three factors: quantum efficiency, triggering probability and geometry efficiency.

$$PDE(OV) = Qe \times Pt(OV) \times Ge \tag{7.1}$$

Quantum efficiency (Qe) expresses the probability that a photon is absorbed by the silicon and converted in an electron/hole pair. Qe is a function of the photon's wavelength and angle of incidence upon the SiPM. This factor is the critical reason

for the wavelength shifting fibres used in the Hodoscope. Triggering probability (Pt) is the likelihood that an electron/hole pair successfully triggers a sustained avalanche process, resulting in a current pulse. This value is highly dependent on the overvoltage (OV) above breakdown applied to the circuit rising rapidly with increasing voltage. Pt is also wavelength dependent, as the probability of generating an avalanche depends on the creation position of the electron/hole pair, which is dependent on the wavelength of the incident photon. The geometry efficiency (Ge), also known as the fill factor, is a function of the amount of dead area present on the surface of the SiPM. Areas that are not active if a photon is incident upon them. Some dead area is necessary to accommodate structures to isolate the pixels from one another; however, each new generation of SiPMs improves geometry efficiency, increasing the acceptance of the devices.

7.6.2 Sources of Noise

The primary source of noise in SiPMs is the dark count rate (DCR), which appears as uncorrelated pulses in the absence of light. These are a result of electron/hole pairs created by thermal excitations in the active region of a GM-APD, mimicking the appearance of a genuine single photo electron trigger pulse. The DCR for a SiPM is dependent on temperature, approximately doubling every 10℃. It scales directly with the area of the device and is an increasing function of the overvoltage applied to it. During operation, the DCR for the Hodoscope will be close to 1 MHz, however, because the pulses are uncorrelated, and have short rise and fall times and tiny amplitudes compared to a signal pulse, the dark events can be filtered with a simple discriminator at the level of 1.5 photo electrons [83].

In addition to the primary noise, there are two sources of correlated noise in SiPMs, afterpulsing (AP) and optical crosstalk (OC). Both of these types of events originate from an existing current event (either a photon event or a dark event) and are largely dependent on the current density of the original event and the trigger probability (Pt). Afterpulsing results from charge carriers, trapped in silicon defects during discharge, which are released later during the recharge phase of a cell. This results in a new current pulse produced on the tail of the true event, typically a few ns after the original peak. Optical crosstalk involves photons which are produced during an avalanche leaking into the active area of a neighbouring cell, triggering another avalanche (known as direct OC), or becoming re-absorbed into an inactive region of a cell. Those in the inactive region can then diffuse back

into the active region of the cell, causing another pulse with a short time delay (the order of a few ns), with respect to the original signal. Both AP and OC increase more than linearly with overvoltage and quadratically with cell size; for more detailed information see [84].

7.6.3 Operation in the Hodoscope

The high efficiency of SiPMs and their high gain, fast timing response and ability to trigger on single photons make them ideal for a fast timing scintillating detector such as the FT-Hodoscope. They are used in place of standard photomultiplier tubes as the detection mechanism for the photons produced in each scintillator tile. Each tile is read out by a 3x3 mm array of Hamamatsu SiPMs, with a pixel pitch of 75 μm and a fill factor of 82%; this provides 1600 pixels for a maximum expected signal size of 200 photons. Each tile is connected to a SiPM by fibres, which shift the wavelength of the photons into the ideal range to maximise the quantum efficiency of the SiPMs. The gain of the detectors is very sensitive to the voltage applied; they require a supply stable to within 0.01 V to maintain a consistent response level. The operating voltage for each SiPM is individually calibrated and adjusted, using variable resistors assigned to each channel [71].

Another consideration is the operating temperature of the SiPMs, as this affects both the dark count rate and the gain of the channels. Keeping the temperature at the lower end of the operating range, (between -20℃ and 60℃ for the Hodoscope) keeps the dark noise to a minimum; it needs to be stable to properly calibrate the gain of the detector. At lower temperatures, which suppress the level of dark noise in the detector, higher overvoltages can be applied to the system, increasing the probability that a photon generated electron/hole pair will trigger an avalanche, increasing the photon detection efficiency of the SiPM [85, 86]. A typical signal from a minimum ionizing particle, interacting with a detector element in the Hodoscope, will result in a signal with a magnitude of between 40 and 100 photoelectrons. This is far larger than the levels of signals produced through dark noise, typically 1-3 photoelectrons when crosstalk is included. As a result, the signal peaks can be easily separated from the dark noise by a simple discriminator cut at the 5-10 photoelectron level, without signal loss. As a result, although desirable to maintain operation at a lower temperature, the main consideration for the Hodoscope is temperature stability during operation. While in operation in Hall B, the detector will be maintained at a nearly constant

temperature, around 25℃, by the atmosphere control systems in the hall.

When in operation, signals from electron triggers arriving at a SiPM will involve a large number of photons arriving almost simultaneously. In this situation, several parallel cells can trigger independently, so that the amplitude and area of the pulse generated is proportional to the number of cells which fired. This allows both the integral of the pulse and the pulse height to be used to determine the amount of photoelectrons generated in the SiPMs. A signal of around 10 photoelectrons in magnitude would be enough to have confidence that a pulse is a signal not generated through thermal excitations. However, simulations indicate that producing a signal of 55+ photoelectrons is required to produce the < 500 ps timing resolution which the detector is designed to surpass.

7.7 Electronics

The electronic circuit boards used for mounting the SiPMs and the pre-amplification stage of signal processing were designed and assembled by colleagues at the L'Istituto Nazionale di Fisica Nucleare in Genoa. The designs passed through several prototypes which were tested and evaluated in Edinburgh before a final design was reached. In this section, some further details of these boards will be discussed, along with information on the flash analogue-to-digital converters used to process signals post amplifications.

7.7.1 Mezzanine and Pre-Amplification Boards

On each mezzanine PCB are mounted two groups of eight SiPMs, with each set having access to an individual high voltage supply. Each board fits into a standard electronics rack, with 15 boards required to supply the 232 channels necessary for the different elements of the Hodoscope, leaving 8 channels of free capacity. An additional pre-amplifier board is required for each group of 8 SiPMs and these are connected to the back of each mezzanine board. The pre-amps are designed to allow the full dynamic range of signals produced in the SiPMs to be processed, with clean signals from one photon electron, up to over 200 for particularly energetic depositions. Signals refined in the pre-amps are read out through lemo cables from the back of the electronics crate. Figure 7.6 shows an overview of the electronics crate with a single fishtail connector attached.

The SiPMs used on the boards are matched into their groups of eight, ensuring a tailored voltage can be applied to each grouping. In addition, the voltage supplied to each channel on the pre-amplifier boards can be adjusted within a 2 V range through a variable resistor, for precision calibration of each channel. All of the boards are managed through a single control board, which also serves as the input point for the low voltage supply, which is spread across all the boards in the crate. Through the user interface, the controller board can be used to adjust the voltage supplied to each channel, monitor the temperature of each SiPM and provide additional higher level functionality for the control software.

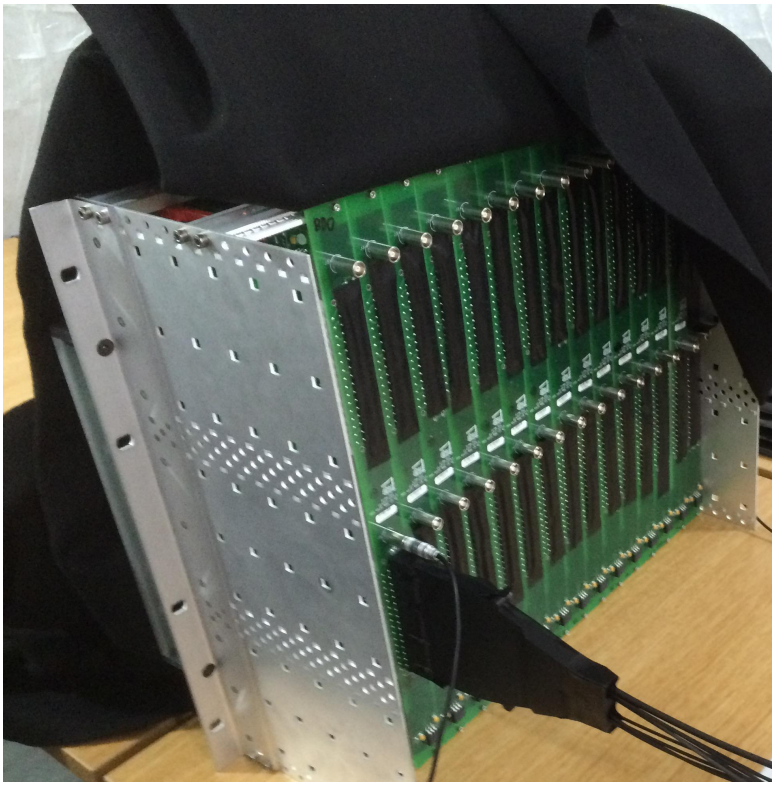

Figure 7.6 *Overview of the amplifier crate with a single fishtail connector attached. The other sets of SiPMs are covered to protect them from damage.*

7.7.2 Flash ADCs

The flash ADCs process the output signal from the electronics, taking a continuous readout of the spectrum of signals arriving at the electronics, rather than simply recording the integrated charge like a standard ADC. When trigger conditions are met, a 'snapshot' of the signal trace is taken and stored to disk, which allows opportunities for additional offline analysis, based on the shape of

the pulse waveform. The modules are also designed to work with a continuous duty cycle, continuing to record data reaching the detectors, while triggers are stored to disk, by reading the results into a set of memory buffers. This design minimises the dead time of the detector system, maximising acceptance and allowing it to process the very high trigger rates expected at CLAS12 luminosities.

7.8 LED Flasher

In order to gauge any changes in the optical performance of the detector system over time, a fibre optic flasher has been installed in the Hodoscope. The system will allow the optical output of the fibres to be measured separately to the files, by using a driver of constant magnitude to radiate the system and measure the level of output, throughout the lifetime of the detector. The flasher includes three diffusers in each layer of the Hodoscope, which are attached to the carbon fibre lid and spread throughout, so that four different areas of the Hodoscope can be studied. The diffusers can be illuminated by spreading light onto the fibre optics in a sector.

The use of the flasher will be most significant pre-run and post-run, to assess any changes in response of the fibres and the effect of any annealing, repairing damage from radiation. The system will allow the response of the optics to be considered separately, rather than just as a convolution of the fibre/tile output.

The LED Flasher was developed by the Nuclear Physics department at the University of Glasgow. The main testing of the flasher was undertaken at JLAB after the construction of the detector.

7.9 Summary

The design process for every element that forms part of the completed Hodoscope detector was the result of several years of research, simulation, design, prototyping, testing and optimisation. A design that may seem superior in theory is often inconsistent, or has unexpected consequences for other elements of the detector system. Therefore, the development process is very complex, requiring detailed tests, adjustment to the resources available and inventiveness in finding solutions to unexpected problems. The designs have also needed to be flexible, because

of the dramatic changes enforced on the dimensions of the detector system more than two years into my PhD.

The next chapter of the thesis covers the process of constructing the FT-Hodo, turning the optimised designs discussed into this chapter into a single high performance detector system able to provide consistent results when installed at JLab.

Chapter 8

Construction of the Hodoscope

The Hodoscope was constructed in a purpose-built environment in a laboratory at the University of Edinburgh. The space was designed to minimise dust levels and exposure to UV light and to provide a temperature controlled environment for testing. The tent was constructed to isolate the detector elements for construction and fitted with an air filtration system and specialised UV lighting, which blocked out wavelengths shorter than the red part of the visible spectrum.

8.1 Tile and Fibre Preparation

A rigorous and meticulous approach to preparing each of the individual tiles and fibres was critical to the absolute performance and consistency across the many different channels of the detector. Initial testing of the tiles and fibres was carried out on a small sample order, to allow the preparation process to be optimised.

8.1.1 Tile Preparation

The plastic scintillator tiles were cut to size and polished by the supplier before being outsourced to a specialist firm to drill the channels for the wavelength shifting fibres. All the tile dimensions were measured and visually inspected for signs of crazing (micro-fractures due to stress) or any other damage; any damaged tiles were excluded from use. All this data was stored for future use in optimising the arrangement of the tiles in the detector. Initially, a subset of these tiles was

prepared to check the quality and consistency of the scintillator tiles, to ensure the accurate performance of the detector. Once these checks were passed, each tile was hand painted with three thin coats of TiO_2 reflective paint, brushing from the centre of each side towards the edge to minimise edge lapping. After painting, each side was lightly sanded, with P1200 grit paper, to produce a smooth finish. The width of the coat of paint was then measured at multiple points, using vernier callipers, and compared to the tile dimensions previously collected. This is to ensure a thickness of 0.15-0.2 mm for optimal reflective properties, without excessively increasing the dimensions of each tile. This process was repeated for every side of each tile and final dimensions collated for positioning optimisation. Where corrections were needed, the painted sides were first smoothed with a layer of P1200 grade sand paper, before refining the surface with 3 μm grade optical lapping film until smooth.

Small variations across a number of successive tiles can combine to produce significant asymmetries and misalignments across the detector volume, hence the need for such meticulous control over this process. Figure 8.1 demonstrates the inherent gaps present within tiles; minimising these is critical to maintain the alignment and acceptance of the detector system.

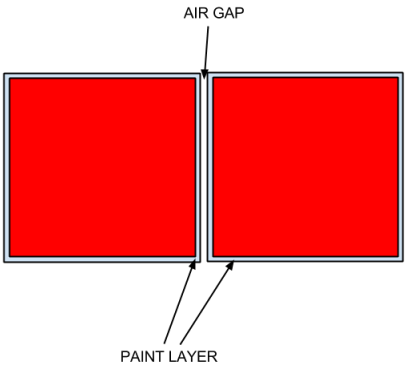

Figure 8.1 *Illustration of the inherent gaps present between tiles (highlighted in red). Minimising these is critical for the alignment of detector elements, maximising the acceptance of the detector [87].*

8.1.2 Fibre Preparation

Once preliminary inspections and testing were successfully completed, the major batch of clear and wavelength shifting fibres was shipped to Fermi Lab to be cut and prepared for fusion splicing. Each length of fibre was checked for any signs of damage, before 6 m lengths of clear fibre and 10 cm lengths of WLSF were polished using the Ice Polishing method [88], before being fusion spliced together, with the join protected by a protective jacket. The initial lengths used are more than 0.5 m longer than the juncture between the tiles and the SiPMs. The fused fibres are required to follow paths of varying length in the finished detector and are trimmed to size later in the construction process. After being fused together, the combined 1 mm diameter fibres were then put into groups of four and slid into protective 3 mm diameter black PVC sleeving, which acts to protect the fibres from damage and seal them from outside sources of light. The final stage of the preparation process was to put a reflective mirror on the end of the WLSF end of the spliced fibres. Each end was cleaned, using a lens cloth and IPA (Isopropanol) solution to remove any dust. Two thin ($\sim$ 0.05 mm) coats of TiO_2 were then applied to the end of the fibre and any excess on the sides removed with IPA. The mirroring must reach the very edge of the fibre, in order to effectively reflect the majority of light which is carried near to the edge of the fibre. However, it must not exceed the boundary, or the fibre will not fit into the channels in the scintillator tiles.

8.2 Assembly

Once the elements were prepared, the first stage of the assembly process was to arrange and attach the scintillating tiles on to the carbon fibre sheets which form the base of each layer of the Hodoscope.

During construction, the Hodoscope was split into its two layers and each group of scintillator elements was arranged and affixed to their respective carbon fibre sheets separately, before the two layers were combined for the later stages of construction.

8.2.1 Tile Arrangement

The tiles are cut to size to a tolerance of less than 0.1 mm; however, these small differences, particularly combined with further uncertainty introduced by the thickness and smoothness of the reflector, can create small but significant gaps between tiles. To maximise the acceptance of the detector, an optimisation algorithm was written by Jamie Fleming at Edinburgh to arrange the detector tiles to minimize the gaps between them. It also prioritised the minimization in regions close to the beamline, which are affected by a higher luminosity than the regions at higher scatter angles.

The regions most strongly affected by any deviation from the standardised size are those where several P15 tiles are grouped together, marked in blue in figure 8.2. In these regions, there are twice as many tile edges as in a similar space filled with P30 tiles, thus amplifying the effect of small differences. To compensate for this, one P15 tile in the centre of each row of scintillators around the centre of the detector (element 16) was cut slightly slimmer, to maintain the uniformity of the detector tile arrangement.

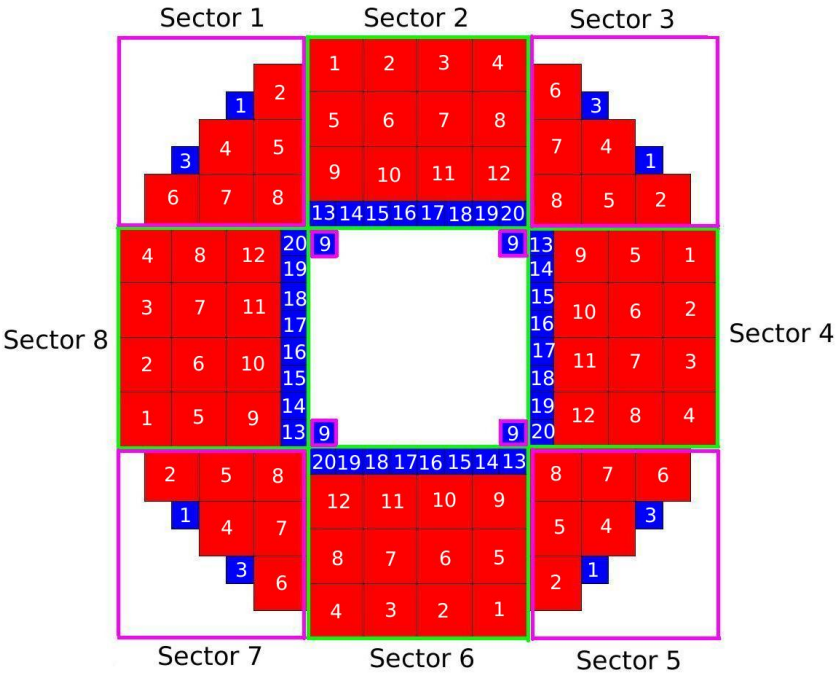

Figure 8.2 *A schematic view of the numbered scintillator tile arrangement in the Hodoscope, with P30 tiles highlighted in red and p15 tiles in blue. The sectors and tiles are numbered starting from the top left whilst maintaining 4 fold rotational symmetry about the beam axis.*

The critical central P15 elements were positioned using a 3D printed plastic jig, positionally aligned by affixing it to the central ring of the detector. Outside this, the optimised P30 tile groupings of even sectors were positioned and aligned, using a bespoke metal jig; the set-up is shown in Figure 8.3. This configuration ensured orientation with respect to the tiles in the calorimeter. The critical P30 tiles closest to the centre of the detector, which are exposed to the greatest level of flux, were aligned first, with the others progressing radially outwards in the jig. After this, the odd sectors were aligned with the even sectors already in place, again working radially outwards in each sector. Finally, the inner ring of P15 tiles was added to complete the arrangement.

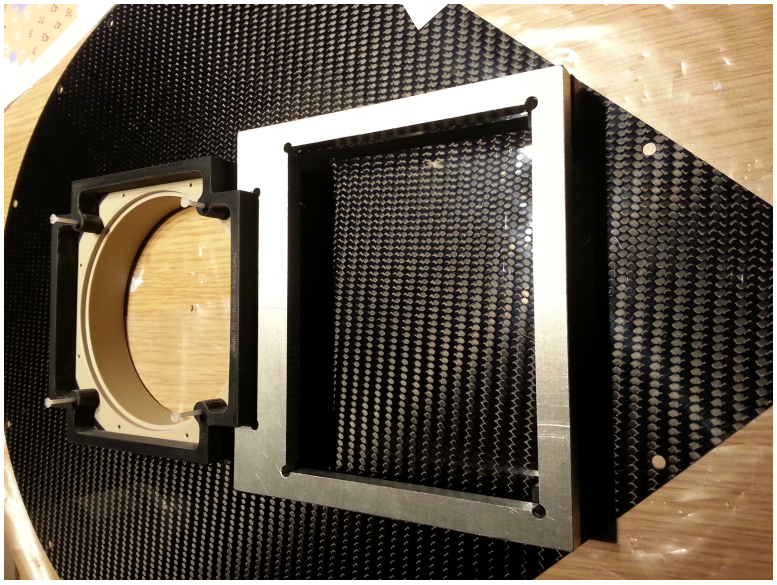

Figure 8.3 *A photograph of the plastic and metal jigs used to align the detector tiles in the even numbered sections of the detector. The plastic jig provided alignment relative to the beam pipe, while the metal jig spaced the inner ring of P15 tiles and constrained the locations of the first P30 tiles to be positioned in each sector.*

While quality control can minimize the effects of asymmetries developing towards the edge of the detector, in a design that attempts to maximise acceptance there will always be some asymmetries produced. These can be clearly seen in Figure 8.4 where a limited number of tiles extend beyond the limit of the detector volume after positioning. These excesses were cut in the machine workshop in Edinburgh and the process of polishing, sealing and quality control repeated for the new edges.

Once all tiles had been positioned and optimised, each one was individually lifted using vacuum tweezers and glued into position, using a two part epoxy

Figure 8.4 *An example of tiles protruding over the radial limits of the Hodoscope.*

adhesive, which cures over two days. A slow curing Araldite was selected for its known radiation hardness and gradual release of heat during the curing process, minimising the impact on the tiles. After glueing, a foam support layer was placed over the tiles, held down with small weights to minimise the chance of movement during curing. Once all tiles were attached in place, a survey was carried ou, marking the corners of all the tiles on a sheet of clear acetate to map their positions in relation to the central structure of the detector. The results of this will be critical when relating data taken from both layers of the Hodoscope, along with results from the FT-Trck and FT-Cal.

8.2.2 Fibre Arrangement

Fibre pathing throughout the main detector volume, through the transition into the confined space in the delta wing, will be discussed in this section. There is limited space within the detector volume and a large number of fibres to route. As a result, I had to design a compromise between the ideal path for each individual fibre, and the collective effect on the system. It is also critical that each scintillating element performs above the design requirements, so tiles which have more restricted pathing need to be prioritised, to ensure a suitable bend radius for their fibres and sufficient light output from the elements.

When optimising the routeing it is critical to consider a number of factors:

- Tiles further from the delta wing have more flexibility for routeing.
- There is a tight limit on the vertical height between the tiles and the roof of the detector volume.
- Minimising cross-over between fibres helps to improve packing efficiency.
- Certain tiles cannot be routed to the nearest exit points because it would require too tight a bending radius.
- The critical point for the fibre exit is the juncture at the base of the detector at the edge of the final row of tiles, where the maximum number of fibres have to fit through a limited space.

Considering these factors and testing arrangements with prototypes in the laboratory led to the grouping shown in Figure 8.5. There are twelve groups of four bundles with four fibres in each one, for each half of each layer, with a mirrored arrangement in the opposite half.

Each group was allocated a column in the delta wing, numbered from the centre outwards, with the closest elements to the delta wing filling the lower rows of the columns. In groups which included P15 tiles, which have only two fibres per element, two tiles were routed into the same fibre bundle. This was essential for space management in the delta wing, and the fibres could be split again to separate SiPM channels upon reaching the electronics. The fibres from tiles further back from the delta wing tended to take a wider arc, closer to the edge of the detector, leaving additional room for the densely packed fibres emanating from the P15 tiles at the centre of the detector.

The bundled fibres in the delta wing are held in place with elasticated cords that pass around each column of four bundles, through holes at the base of the delta wing, and are tied in place at the top of the delta wing. Each column of bundles is fixed in place at two points and the points shift along the length of the delta wing, to minimize the space taken up by the cords.

8.2.3 Fibre Glueing

Once the scintillator tiles were aligned and affixed into position for each of the layers in the Hodoscope, the next stage in the construction process was to

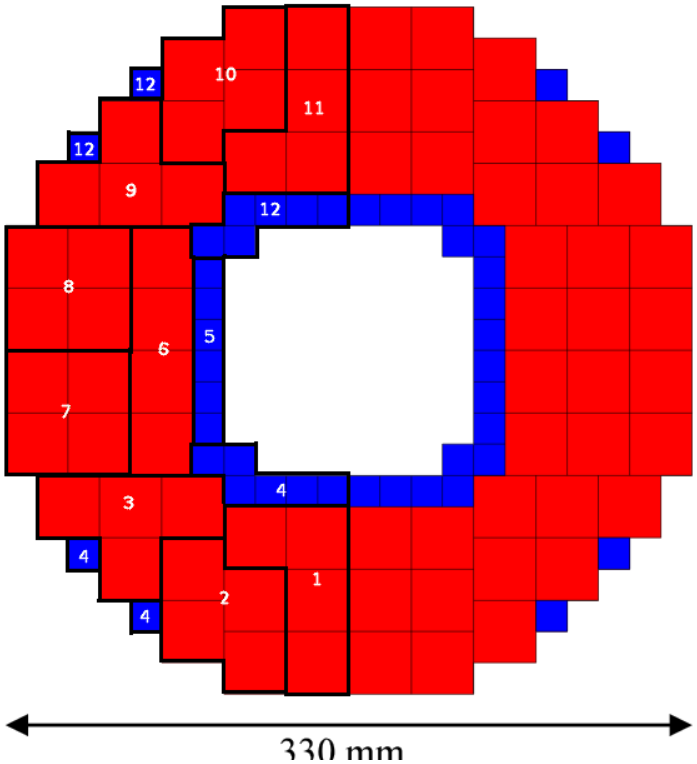

Figure 8.5 *The groups of tiles allocated to different columns in the Hodoscope delta wing. Column numbers ascend from the closest point to the central pillar in the delta wing outwards towards the edge. The arrangements are mirrored symmetrically for both sides of the detector and apply to both the thick and thin layer.*

embed the WLS fibres into the channels in the tiles, following the fibre pathing design, taking each fibre through the detector body and into position in the delta wing. This required affixing the fibres into place in a specific order, addressing problematic tiles as a priority, and then progressing from the tiles closest to the delta wing back up the detector and radially outwards.

The optical glue used to fix the fibres into place was Epotek 301-2, a radiation hard (no significant reduction in performance at the radiation levels experienced in the hodoscope) clear optical adhesive with a similar refractive index (1.54) to both the scintillator tiles, (1.58) and WLS fibres (1.42 and 1.59) [69, 70, 89]. Epotek 301-2 is a two part adhesive which requires an overnight cure to solidify. The glue was prepared in small batches, 2-3 g, enough for around 8 P30 tiles. The ratio of the components of the two-part glue was accurately measured, by first measuring the weight of the more viscous component on scales accurate to 0.01 g. The secondary component was then added by a fine syringe up to the total weight for an exact ratio. The two parts were then blended with a mixing baton for five minutes, following a figure of eight pattern, to evenly mix the components. The combined glue was then placed in a vacuum chamber and the pressure was lowered gradually until just below the boiling point of the epoxy and then visually inspected for trapped gasses. This process removed any air bubbles which had been trapped in the mixture without compromising the quality of the adhesive. Samples from each batch of glue were stored between microscope slides and marked for future reference, along with notes on the fibres glued with each batch.

Once the glue was prepared, the tile channels were cleared of any debris, using pressurised air, before a small quantity, 20-30 μg of glue was inserted, using a syringe directly into the very bottom of each channel. The lengths of fibre to be inserted were given a final clean with IPA, before being inserted one by one into the channels. Insertion of the fibres forced the pooled glue upwards, pushing any air trapped in the channel up and out of the channel ahead of the glue and creating a smooth even connection between the fibre and the scintillator tile. Once glued in position, the fibres were left raised up, so gravity ensured the fibres stayed in position, filling the entire length of the channels. Tiles were glued in small batches to ensure ideal conditions for curing.

The fibres also needed to be glued into the fishtail connectors which form the junction with the SiPMs, in order to ensure a stable connection. In this case, the glue joint is not an optical connection, and the Araldite glue which was also

Figure 8.6 *Ends of the fishtail connections after the fibres were glued into place then polished. The connectors from the layer of the Hodoscope which is currently open are clearly differentiated by the captured green light which is radiating from the ends of the connectors.*

used for affixing the tiles to the carbon sheets was the preferred option. The fibres for each element were inserted into the channels in the end pieces of the fishtail connectors, leaving an overshoot of at least ∼5 cm. The exact amount was dependent on the fibre path length between the specific tile and SiPM being used for each channel. About 100 μg of glue was then applied to a ∼2 cm length of this overshoot next to the connector, and this was pulled back into the connector block for curing overnight. Once cured, the fibres were trimmed using fibre cutters, before being polished flush with the edge of the connector. The fibres were then smoothed using several grades of optical lapping film down to 3 μm, for improved optical transmission [90]. Figure 8.6 shows the ends of the polished fibre connectors after completion of the glueing process, with the fibres of the open half of the Hodoscope illuminated with green light clearly visible.

8.3 Sealing and Transport

After all the elements of the detector system were glued into place, the final stage of the process was to seal the detector system from outside sources of light. This was done separately for each layer of the detector once it was ready, before rotating the entire detector as a unit and starting work on the other layer.

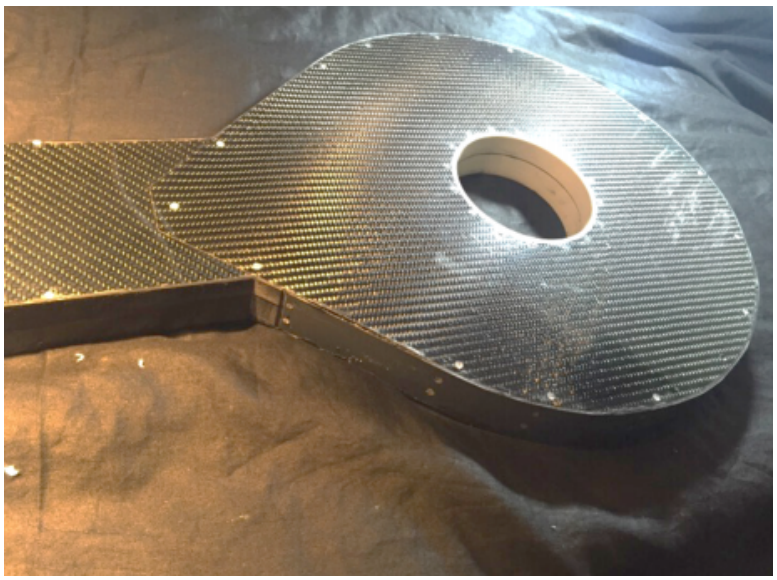

Figure 8.7 *The sealed head of the detector, before the Kapton® was applied.*

The head of the detector system was sealed by first placing a small bead of black silicon putty, approximately 1 mm thick, around the end of the detector rim, including the delta wing and the the central ring. The carbon lid was then positioned and secured down using nylon screws, taking great care to minimise any unnecessary pressure on the WLSFs. The edge of the detector system was then sealed, with a layer of Kapton® tape securing the layer in place. These steps ensured that the head of the detector system was sealed from external sources of light. A picture of the sealed head of the detector, before the Kapton® tape was applied, is shown in Figure 8.7 Between the end of the delta wing and the electronics unit, the fibres are bundled together and wrapped in a layer of black tedlar, creating a light-tight seal between the end of the detector and the electronics unit.

Transporting the completed detector system from Edinburgh to Jefferson Lab required specially designed storage which was designed via consultation with Seabourne Group. The storage crate was based around laser-cut high density foam, made to measure for the Hodoscope's dimensions. This was designed to minimise any movement during transport and protect the fragile components of the detector. The CAD design of the storage crate, along with a photograph of the packed detector is shown in Figure 8.8.

The Hodoscope was shipped from Edinburgh at the beginning of 2016 and arrived in JLab in mid January, ready for testing in conjunction with the completed FT-Cal.

Figure 8.8 *The specially designed transport crate for the FT-Hodo. Top: A CAD picture of the design. Lower: An overhead view of the FT-Hodo packed before being sealed and transported to Jefferson Lab.*

8.4 Testing at JLAB

A team of four from Edinburgh, including myself, arrived at JLAB in late January 2016 to set up and test the Hodoscope. The primary aims of the trip were to:

- Inspect the Hodoscope for any damage during transport.
- Set up the detector for some preliminary testing in Jefferson Lab.
- Make repairs to any damaged channels or components
- Begin testing in combination with the FT-Cal.

After unpacking, the detector was inspected for any obvious signs of damage. The primary concerns were cracks in the fragile optical fibres or detector elements, along with possible damage to the fishtail connectors. A couple of the end pieces of the fishtail connectors had been cracked in transport, but otherwise there were no obvious signs of damage. These could be easily replaced by cutting small sections from the fibres and reinserting them into a new end piece.

The next aim was to set up the detector and electronics to test for any problems, gradually moving through the sectors before attempting to test all channels simultaneously. Testing the channels in this manner allowed any dead or poorly performing channels to be identified and investigated to find the cause of the problem. The detector was positioned on top of the FT-Cal and connected up to the electronics, with improvised supporting structures constructed to support the fibre bundles. This is shown in Figure 8.9.

The Hodoscope was tested in conjunction with the FT-Cal, using cosmic rays and a pair of large scintillator panels as a trigger. This allowed both systems to be run simultaneously with an outside trigger, before attempting more complex tests using the detectors themselves as the trigger mechanism.

Early testing showed that there were a few problems with some channels in the electronics, but all the channels of the detector were working well. This was the first time the Hodoscope had been tested in conjunction with the finished FT-Cal and also read out using flash ADCs. This was only the beginning of the calibration and optimisation of the detector in conjunction with the full electronics set-up, but the initial results were very positive.

Figure 8.9 *Setting up the Hodoscope for testing at Jefferson Lab. An improvised structure was used to support and hold in place the fibres during testing. This arrangement minimised mechanical stress on the fibres and ensured stability for several months of testing.*

My major contributions to the development of the Hodoscope ended with the successful test at JLab. I continued to attend group meetings and contribute my experience to discussions, but after this point I devoted the majority of my time to the analysis covered in Part III of this thesis.

8.5 Current Status of the Hodoscope

Since the successful initial tests of the constructed detector at JLab, the main focus of development has been developing and optimising the software which will be used to control the function of the detector system. Alongside this, calibrations have been undertaken to find the optimal voltages and temperatures for operation of the detector system. A few of the results at the time of writing will be presented in this section, along with a brief overview of the timeline for the detectors installation into CLAS12.

Figure 8.10 shows a plot of the amplitude of low level noise present in the SiPM from sector 8 element 5 in the detector system (one of the thin tiles). A clear peak can be observed at $\sim$ 11 mV, which is the noise generated by thermal electrons producing signals equivalent in size to one photoelectron. A second, much smaller peak can be seen at $\sim$ 22 mV, a double photoelectron peak, caused

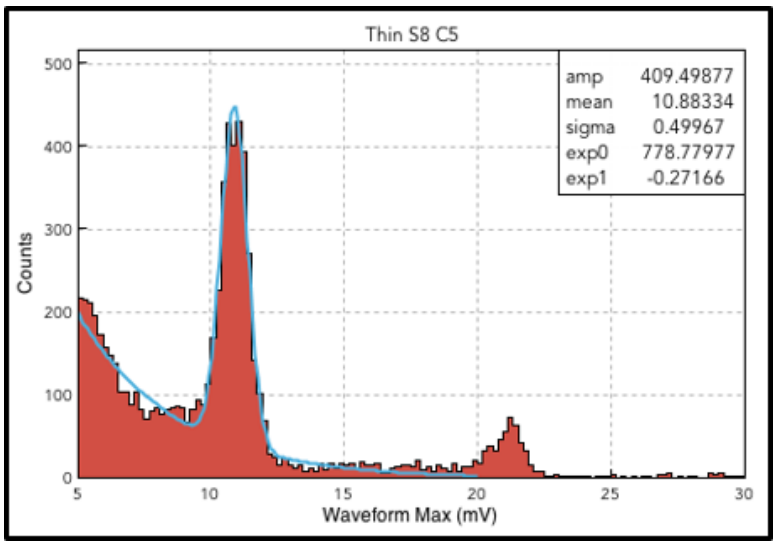

Figure 8.10 *A fit to the single photoelectron peak of one of the channels in the Hodoscope. This is predominantly a result of the thermal noise present in the SiPMs. This peak can be used in conjunction with the smaller second photoelectron peak (also visible) to calibrate the output of each individual channel for signal events.*

by 2 pixels triggering almost simultaneously. The distance between these peaks can be used as a calibration of the detector system, to determine the number of photons arriving in a signal peak. The minor peak before the single photoelectron peak, is a pedestal peak, caused by latent current, left residually in the system, producing signals of very low amplitude.

Figure 8.11 shows the typical Landau distribution of a charge spectra produced by collection of cosmic ray data in the flash ADCs. Using this in conjunction with the data collected from the single and double photoelectron spectrum shown in Figure 8.10, the average number of photoelectrons produced by each element of the detector system can be determined. This is shown for the thick and thin tiles in sector 4 in Figure 8.12.

The results for the number of photoelectrons produced by the channels in a representative sector are shown in Figure 8.12 demonstrating the detector elements are performing above design requirements. The elements from the thick layer of the detector, which are critical for the timing resolution of the system, are averaging over 100 photoelectrons. This is almost double the number estimated to be required from simulation to achieve 0.5 ns timing resolution. The thin tiles are not performing as strongly as the projections from simulations, but nevertheless they are averaging $\sim$ 50 photoelectrons. This is well beyond the requirements for clean background rejection. These levels of performance are

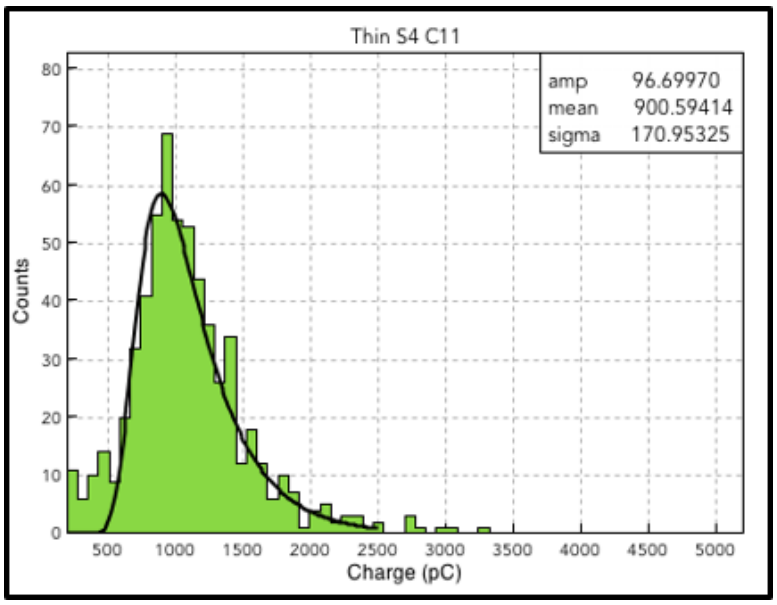

Figure 8.11 *A typical distribution of the charge deposited by data collection with cosmic rays. The dataset follows a Landau distribution with a long tail at higher energies.*

a dramatic improvement over the performance levels of the detector elements achieved in the first beam test at DAΦNE, Section 6.2, just before I joined the project, with the highest performing element in this sector producing almost eight times the number of photons as the highest performer in that test.

Currently, the Forward Tagger is scheduled to be installed into Hall B at the beginning of July 2017, ready for an engineering beam test in September 2017. Once the detector is fully installed and has access to beam conditions, full calibration and optimisation can begin. The results from current testing indicate that the sub-nanosecond timing required of the detector should be achieved and, with proper calibration, a much lower timing resolution is achievable.

8.6 Summary

The Forward Tagger Hodoscope was constructed in a purpose built environment at the University of Edinburgh. This first involved preparing the 232 scintillator tiles and 784 WLSF ready for assembly. Once the laborious process of preparation and quality control was complete, the detector assembly could begin. This process followed a very detailed plan to ensure the optimum performance of the detector system, carefully mapping and detailing the process as it progressed. Once

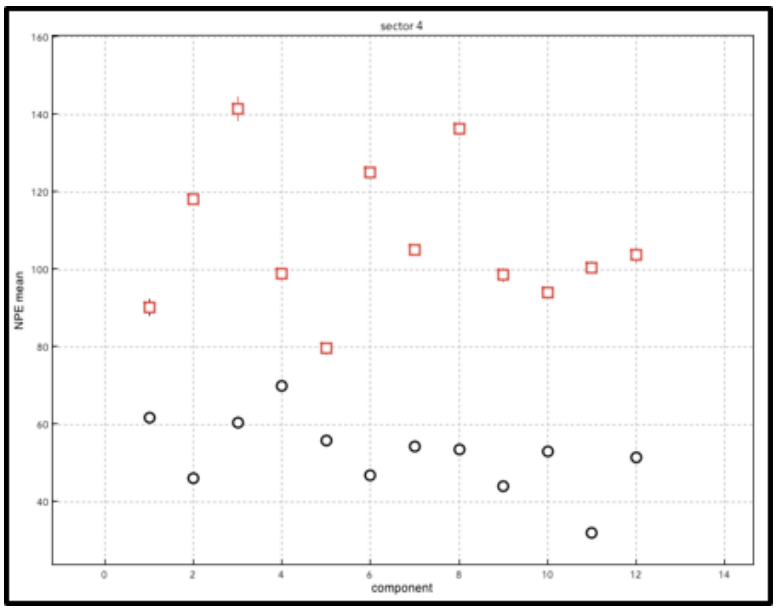

Figure 8.12 *The average number of photoelectrons produced by each tile in Sector 4 of the Hodoscope for a calibration run with cosmic rays. The thick tiles (red squares), used for improved timing resolution, produce an average of over 100 photoelectrons. The thin tiles (black circles), used for improved background rejection, average around 50 photoelectrons.*

assembled, the detector was sealed and the delicate elements of the detector carefully arranged in bespoke packaging, designed to protect the system during transport to Jefferson Lab.

The system sustained minimal damage during transport and any poorly performing channels were repaired, while the Hodoscope was tested for the first time with the constructed FT-Cal. Joint tests were carried out, utilising cosmic rays to take coincidence measurements, with the two detector systems working in unison. The results from these initial tests were highly successful and the system underwent an extended period of testing, where the software for its operation in CLAS12 was further developed.

Current results from the Hodoscope show the thick and thin tiles producing signals with an amplitude equivalent to a 100 photoelectrons and 50 photoelectrons respectively. This is well beyond the design requirements expected of the Hodoscope and, with this performance, sub nanosecond timing resolution will be achieved. Optimisation of the algorithms to determine the timing resolution is ongoing, with an aim of achieving sub 500 ps timing resolution. In July 2017, the Forward Tagger, including the Hodoscope, will be installed into Hall B at

Jefferson Lab, and in September 2017 the first engineering beam run is planned to occur. With proper access to beam data, full calibration and optimisation of the Hodoscope will begin, working in conjunction with all the other detector systems in CLAS12.

Part III

First Measurement of the $\gamma p \to \omega\pi\pi p$ Decay Channel

Chapter 9

The $\gamma p \to \omega\pi\pi p$ Decay Channel

In parallel with my work on the Forward Tagger, I carried out an analysis of the $\gamma p \to \omega\pi\pi p$ decay channel, using data collected from the g11a run period of CLAS. This is a study in meson spectroscopy, utilising a dataset from a photon beam on a liquid hydrogen target. This is the first time this decay channel has been studied using data from a photon beam, and it is of particular significance for resonant decays via $b_1(1235)\pi \to \omega\pi\pi$ that is predicted to be a decay channel of the lightest hybrid meson [26]. In addition it also includes a number of resonant decay channels for which there are limited experimental datasets. This reaction channel has been identified as one of the 'golden channels' for meson photoproduction in CLAS12, and this study is a preparatory investigation into the channel at CLAS6 energies. The details of the analysis and its results are discussed in the following sections.

Before going any further it is important to define the Mandelstam variables, s, t and u, for the scattering processes of two particles to two particles are defined as:

$$s = (p_1 + p_2)^2 = (p_3 + p_4)^2 \tag{9.1}$$

$$t = (p_1 - p_3)^2 = (p_4 + p_2)^2 \tag{9.2}$$

$$u = (p_1 - p_4)^2 = (p_3 - p_2)^2 \tag{9.3}$$

Channel	Branching Ratio
$\omega \to \pi^+\pi^-\pi^0$	$89.2\% \pm 0.7\%$
$\omega \to \pi^0\gamma$	$8.28\% \pm 0.3\%$
$\omega \to \pi^+\pi^-$	$1.53\% \pm 0.1\%$

Table 9.1 *The major decay channels of the ω meson [5].*

Where p_1 and p_2 are the four-momenta of the photon and target proton and p_3 and p_4 are the reaction products after the interaction. These define the s-channel, t-channel and u-channel processes that are shown in Figure 9.1.

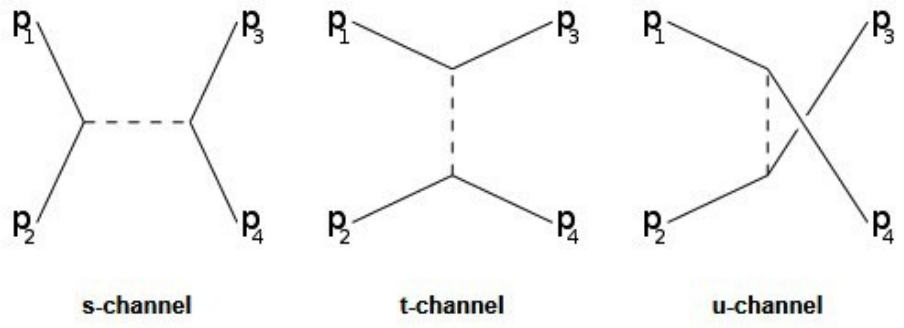

Figure 9.1 *Diagrams of s-channel, t-channel and u-channel processes [91].*

9.1 The $\omega\pi\pi$ Final State

ω is a well established vector meson $J^PC = 1^{--}$, with a mass of 785.65 ± 0.12 MeV/c^2 and a narrow decay width of 8.49 ± 0.08 MeV/c^2 [5]. However, due to its short lifetime, $(7.75 \pm 0.07) \times 10^{-23}$ s it is always reconstructed from its final state particles. The main branching ratios for its decay are listed in Table 9.1.

ω predominantly decays to the $\omega \to \pi^+\pi^-\pi^0$ final state. This leaves the $\gamma p \to \omega\pi\pi p$ reaction as typically a six particle final state, seven if you include the dominant decay branch of $\pi^0 \to \gamma\gamma$. This is a complex final state which requires a wide acceptance detector and a high statistics dataset to ensure a large data sample. CLAS is ideally suited for this purpose and the high statistics g11a run, discussed in detail in section 9.3, provides an ideal dataset for this analysis.

In the energy range available in the g11a dataset, the decay channel is open to a wide range of possible decay routes, including seven different intermediate meson states ending in $\omega\pi\pi$. The properties of most of these mesons are poorly

Meson	$I^G(J^{PC})$	Mass (MeV/c^2)	Full Width (MeV/c^2)	Branching Ratio ($\omega\pi\pi$)
$a_2(1320)$	$1^-(2^{++})$	1318.3 ± 0.5	107 ± 5	$(10.6 \pm 3.2)\%$
$\omega(1420)^*$	$0^-(1^{--})$	$1400 - 1450$	180-250	seen
$a_0(1450)$	$1^-(0^{++})$	1474 ± 19	265 ± 13	seen
$\pi_1(1600)^*$	$1^-(1^{-+})$	1662 ± 9	241 ± 40	seen
$\omega(1650)$	$0^-(1^{--})$	1670 ± 30	315 ± 35	seen
$\omega_3(1670)^*$	$0^-(3^{--})$	1667 ± 4	168 ± 10	seen
$\pi_2(1670)^{*\dagger}$	$1^-(2^{-+})$	1672.2 ± 3.0	260 ± 9	$(2.7 \pm 1.1)\%$
$\Phi(1680)$	$0^-(1^{--})$	1680 ± 20	150 ± 50	not seen

Table 9.2 *Resonances decaying to $\omega\pi\pi$ in the energy range of the g11a dataset.* * *Can decay via $b_1(1235)\pi \to \omega\pi\pi$.* † *Going via $\omega\rho \to \omega\pi\pi$ [5].*

understood, with great uncertainty in the mass, decay width and branching ratios for the particles decaying to $\omega\pi\pi$. The currently accepted values, according to the annual particle data group review (PDG) [5], are shown in the Table 9.2.

Amongst these states, only the $a_2(1320)$ is easily distinguishable from other potential decay routes, with a relatively narrow decay width and a clear separation in mass from other decay paths. The two states around 1450 MeV/c^2 and the five states around 1670 MeV/c^2 are much more challenging to isolate, with the possible exception of the $\pi_2(1670)$, as a cut can be placed on the mass of the combined detected 2π around the mass of a ρ meson. This highlights the $\pi_2(1670) \to \rho\omega$ decay which has a branching ratio of $2.7 \pm 1.1\%$.

9.2 Previous Work on the $\omega\pi\pi$ Final State

There is limited previous work considering decays to the $\omega\pi\pi$ final state. This section will focus in more detail on the work studying the $a_2(1320)$, as this state is fairly narrow with a significant branching ratio to the $\omega\pi\pi$ final state. A summary will also be given on previous work on the other possible resonances in the decay range, at the end of the section.

According to the particles data group, there are no studies able to suitably determine the mass of the $a_2(1320)$ or its width for this reaction channel, with the vast majority considering the 3π final state. However, there are four papers

which provide data for branching ratios of the decay with respect to the majority 3π mode, typically via the $\rho\pi$ channel: [92–95]. All the papers date from 1973-74 and use data collected from hydrogen or deuterium bubble chambers. The studies mostly used pion beams, although the data from Defoix et al. was taken from a proton anti-proton experiment. The yield of $a_2(1320)$ observed varies between 60 and 279, providing limited statistics on the decay channel; from these were determined branching ratios of between 0.10 ± 0.05 and 0.28 ± 0.09, normally for $\Gamma(a_2 \to \omega\pi\pi)/\Gamma(a_2 \to \rho\pi)$.

At the time of writing, none of the analyses used by the PDG to provide values for the $a_2(1320)$ mass and decay width studied the $a_2 \to \omega\pi\pi$ decay mode. The studies highlighted provide evidence only for the branching ratio of the particle to this decay state. Each of these studies was quite limited in its statistics and its methods for background subtraction and fitting. Mass spectra were fitted, by selecting either a Gaussian or a type of Breit-Wigner, in combination with a polynomial or unspecified modified phase space background, or even in some cases a hand-drawn background. Little justification for these choices was provided, beyond that adding a typical resonant structure such a Breit-Wigner improved the quality of the fit. Several mentioned, but none properly addressed, the combinatorial background inherent in this channel, and they made little attempt to remove any bias created by selecting combinations which fitted with expectations for the ω or $a_2(1320)$ mass. The conclusions of these studies varied significantly, with quite large errors arising from the methodology.

Table 9.3 provides a summary of the experimental methodologies used to determine the properties of the resonances listed in Table 9.2. It also highlights whether any of the datasets studied the $\omega\pi\pi$ final state.

With the exception $a_2(1320)$ and $\pi_2(1670)$, across the range of resonances listed there is limited available experimental data. There is great uncertainty in the masses, widths and decay cross-sections for these particles. For the $\omega\pi\pi$ decay channel, there is even less data available, with the last listed studies in PDG for the $a_2(1320) \to \omega\pi\pi$ from the 1970s, and only one listed study for $\pi_2(1670)$ ending in a $\omega\pi\pi$ final state. In addition, the dominant means of production is via pion beams, with some electron annihilation experiments; none of the studies used photoproduction. The current analysis utilises the high statistics g11a dataset, in order to undertake the first measurement of the $\gamma p \to \omega\pi\pi p$ decay channel.

Meson	Typical Beam and Target	$\omega\pi\pi$ Final State	Reference
$a_2(1320)$	$\pi^- p$	none	[96]
$\omega(1420)$	e^+e^-	some	[97]
$a_0(1450)$	$\bar{p}p$	none	[98]
$\pi_1(1600)$	$\pi^- p$	some	[99]
$\omega(1650)$	e^+e^-	some	[97]
$\omega_3(1670)$	$\pi^- p$	some	[100]
$\pi_2(1670)$	$\pi^- p$	some	[99]
$\Phi(1680)$	e^+e^-	some	[101]

Table 9.3 *Summary of some of the previous experiments studying the resonances decaying to $\omega\pi\pi$ in the energy range of the g11a dataset.*

9.3 The G11a run period

This analysis uses data collected during the g11a run period in CLAS, part of experiment E04021, Spectroscopy of Excited Baryons with CLAS: Search for Ground and First Excited States [102]. The runtime utilised a photon beam with a maximum energy of ~ 5 GeV, produced via a Bremsstrahlung radiator from the CEBAF electron beamline. The primary aim of this experiment was to determine more about the nature of a possible pentaquark state which had previously been observed at several labs around the world. However, it also provided an extremely high statistics dataset for meson spectroscopy of rare and exotic decays.

The target for the experiment was composed of liquid hydrogen, kept in this state using cryogenics. The target cell was cylindrical, 40 cm in length with a radius of 2 cm, and constructed from Kapton®. The temperature and pressure of the target was measured approximately once per hour, to allow the density of the target to be determined over time.

The trigger condition during the g11a run required a coincidence between the photon tagger Master OR (MOR) and the CLAS level 1 trigger. The entire tagger was live and collected data during runs, a but only the first 40 segments of the tagger (highest photon energy) were enabled in the trigger. To satisfy the requirements for the level 1 trigger, for any of the 6 sectors in CLAS, a signal was required in any of the 4 start counter paddles and any of the 48 ToF scintillators within a timing window of 150 ns. To satisfy the level 1 trigger as a whole, at

least 2 separate sectors were required to fulfil the requirements listed above. In addition for g11a, a coincidence was required between the photon tagger MOR and the start counter within a timing window of 15 ns [103]. These trigger conditions were designed to select events with 2 or more charged particles and a photon beam energy higher than 1.5 GeV.

During the run period, the toroidal magnets were run with a current of 1920 A, compared to the maximum 3861 A. This configuration improves the detector's acceptance of negatively charged particles, at the cost of momentum resolution gained from a stronger magnetic field.

Data collection ran from May 17th to July 29th 2004, producing a total of 20 billion triggers, and 21 TB of data were recorded. The dataset is well understood, with extensive corrections and calibrations applied to published analyses over time.

9.4 Summary

$\gamma p \to \omega\pi\pi p$ is expected to be one of the 'golden channels' for meson spectroscopy in CLAS12. The current analysis was designed as preparation for further investigation at 12 GeV energies, by studying the decay channel at the energy range used in CLAS6. It is the first photoproduction measurement of the decay channel and it uses the g11a run from the CLAS detector. The dataset utilises a photon beam of up to 5 GeV incident on a liquid hydrogen target, producing a high statistics dataset of over 20 billion triggers. The wide acceptance of CLAS and the high statistics of the dataset provide an ideal environment to study rare meson decays, such as those that decay to $\omega\pi\pi$. For this decay channel, there are eight different known meson resonances in the energy range available to the dataset. However, most of these are poorly constrained, broad resonances with little previous experimental data to determine their properties. This current analysis hopes to provide new insight into this area and provide a foundation for further investigation at CLAS12 energies.

Chapter 10

Data Preparation

In this chapter, the process of turning the raw data into data suitable for physics analysis is described. The chapter is structured in a sequential order following the corrections and adjustments which the data undergoes.

10.1 CLAS Cooking

The raw datasets collected by the detector systems in CLAS are first processed through a stage known as 'cooking'. This converts the output of the detectors into physics variables, such as position or momentum, and is a consistent process applied to all analyses done on a dataset collected in CLAS. The g11a cooking process is detailed in [104]. The analysis carried out in this thesis begins with the cooked data.

10.2 Run Selection

Data collected during the g11a run period was grouped into runs, each of which contained approximately 10 million events. The beamtime covered runs 43490 to 44133, of which the vast majority were undertaken with a beam energy of 4.019 GeV. Runs 44108 to 44133, at the end of the beamtime, were taken at a higher energy of 5.021 GeV.

The run selection used in this analysis follows the same logic outlined in the PhD

Run	Reason for Exclusion
43490-43525	Commissioning Runs
43558	Anomalous ω Yield
43675-43676	Different Trigger Conditions
43777-43778	Different Trigger Conditions
43871	Data Processing Error
43981-43982	Drift Chamber Problems
43989-43991	Data Acquisition System Problems
44013	Different Trigger Conditions
44108-44133	5.021 GeV Beam Energy

Table 10.1 *g11a runs that were excluded from the analysis.*

thesis of M. Williams for analysis of g11a data [103]. The small number of runs taken at higher energy is excluded, to avoid any possible systematic differences between the runs, thus avoiding statistical uncertainties in the total dataset. Runs 43490 to 43525 were commissioning runs, preparatory work to ensure the smooth operation of the equipment. These were not meant for use in physics analysis and therefore have been excluded. Twelve other runs have also been excluded, either for unusual trigger configurations, noted problems with the run, or an anomaly where the normalised yield ω yield was much lower than in other runs. The excluded runs are summarised in Table 10.1.

10.3 Corrections and Particle ID

Particle reconstruction within CLAS requires a precise understanding of the kinematics of particles passing through the detector systems. After the raw data is collected, several corrections are applied, in order to better represent the true properties of the events collected in the detector.

10.3.1 Energy Corrections

Energy corrections are applied to the detected proton and pions, to correct for energy lost due to passage through materials in the detector. At the energies used in CLAS, this primarily occurs through ionisation and atomic excitation.

The corrections apply to energy lost within the target volume, interaction with the beam pipe, the start counter and the air gap between these and the region one drift chambers. The magnitude of these is calculated using the Eloss software package written by Eugene Pasyuk, an extensively reviewed set of energy corrections for particle transport through CLAS [105].

An additional energy correction is required because of a misalignment of the photon tagger's focal plane [106, 107]. This leads to an inaccurate determination of the photon energy. This correction was developed by M. Williams for all the runs of g11a data, by analysing the $(\gamma)p \to p\pi^+\pi^-$ data, to determine directly the beam energy from the detected final state particles. A method of kinematic fitting was used to find the most likely solution to energy differences. This was done on an event by event basis, applying energy and momentum corrections from the previous iteration to the three final state particles and calculating the beam energy from this. The difference between this and the measured value was determined and the results split into bins of beam energy. For the final correction the Gaussian mean of each bin was extracted and added to a beam offset calculated for each run of the g11a dataset. For further detail on the methodology and results see [103].

10.3.2 Momentum corrections

Initial momentum corrections are applied during the cooking process to account for the non-uniformity of the magnetic field in CLAS. This corrects for the adjusted trajectories in the drift chambers. However, variations from the expected magnetic field map, and/or discrepancies in the drift chamber surveys require empirically determined corrections, specific to the g11a runs. These corrections were again developed by M. Williams, through analysis of the high statistics $\gamma p \to p\pi^+\pi^-$ decay channel, utilising a method of kinematic fitting. Just as for the energy corrections this is done on an event by event basis but for 3 hypotheses $\gamma p \to p\pi^+(\pi^-)$, $\gamma p \to p(\pi^+)\pi^-$ and $\gamma p \to (p)\pi^+\pi^-$ [103]. For each iteration, energy and tagger corrections are applied, and the properties of the missing particle is calculated from the others. The momentum corrections are calculated for 72, 5° bins in the azimuthal direction, ϕ, and 15 bins in the polar direction, θ, with greater resolution at smaller angles in θ. Within each bin the mean properties are extracted and used to determine the corrections for momentum, θ and ϕ which are dependent on the initial momentum, incident direction and

charge of the particles. Again for further detail on the methodology and results see [103].

10.3.3 g11a filter code

The cooked datafiles which were selected for analysis needed to be filtered in order to identify possible reactions of interest from the wider dataset, reducing file sizes to manageable levels for analysis. The filter code includes energy loss, momentum, and photon tagger corrections which have been developed over the years for g11a datasets. Particle ID is also finalised at this stage of the code, identifying the proton and pions for later use in the code.

Filtering was done using broad selection, requiring a specific number of positive or negatively charged particles, a property easily identified by the passage of charged particles through the drift chambers. In addition to this, to restrict the file size to a manageable level, a broad cut was used, requiring a missing mass of the system of particles to be in the range 0.68-0.92 GeV/c^2.

10.3.4 Particle Identification

The quality of particle identification produced by the filter code was assessed by comparing how well a hypothesis of the particle type compares to the empirically measured value after processing. This was done using the quantity:

$$\Delta\beta = \beta_{meas} - \beta_{calc} \tag{10.1}$$

Here β_{meas} is the experimentally determined value for β and β_{calc} is the value for a hypothesised particle. This can be rewritten as:

$$\Delta\beta = \beta_{meas} - \sqrt{\frac{p^2c^2}{m_p^2c^4 + p^2c^2}} \tag{10.2}$$

Here m_p is the mass of the hypothesised particle, p is the magnitude of its momentum and c is the speed of light. If particle identification is working well and the detector systems well calibrated, then $\Delta\beta$ will be close to zero. Misidentified particles will appear as additional structures in two-dimensional

plots of $\Delta\beta$ against particle momentum. Examples of the $\Delta\beta$ plots produced are is shown in Figures 10.1 and 10.2.

The particle identification study indicated that the methodology used in the g11a filter code worked in the vast majority of cases, correctly identifying protons and pions, with minimal contamination from other particles. It should be noted that in the analysis framework there are additional cuts and calibrations included, which should exclude contamination from other beam bunches responsible for some of the minor structures in Figures 10.1 and 10.2.

10.4 Analysis Framework

This analysis utilises the HASPECT (HAdron SPEctroscopy CenTer) analysis framework, the development of which I have been an integral part of over the course of my PhD [108]. It is a customisable package designed to standardise, optimise and accelerate the process of meson spectroscopy analysis. The configuration makes use of the ROOT large scale data analysis framework [109], integrating a number of its higher level features such as PROOF, scalable multi-core processing [110] and ROOTSTATS, advanced statistical analysis tools [111].

The HASPECT framework was developed to be computationally efficient and scalable, taking advantage of well established and developed tools already present in ROOT. The software's flexible structure allows users to tailor the software to fit their needs, whilst still utilising the integrated tools. Its consistent structuring allows users' analyses to be cross checked more efficiently by the collaboration. It also enables more efficient development, with less time spent in the complicated, but largely standardised, procedures for reading in and processing data, by transferring this information into formats more useful for physics analysis, such as constructing particle objects with mass, momentum, etc. This consequently allows a faster transition between data collection and higher level physics analysis.

Development of the framework began close to the start of my PhD, and throughout I have acted as the primary beta tester for the framework as it has developed, highlighting any problems I encountered, suggesting changes for improved ease of use or additional features that would be beneficial. Throughout this period, the software has changed enormously, with new features added regularly over time; my own codebase has been completely restructured on

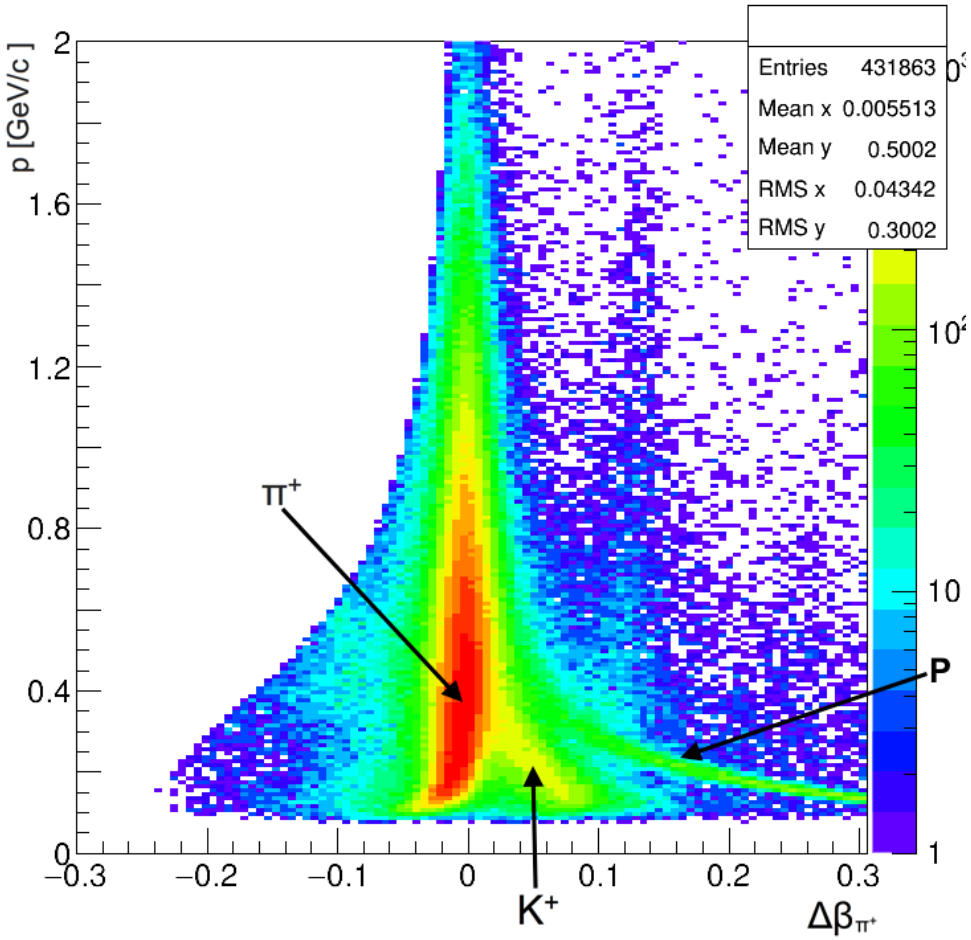

Figure 10.1 *A logarithmic plot of $\Delta\beta$ against momentum for the detected π^+. The vast majority of the dataset is correctly resolved, with the intense red region centred around $\Delta\beta = 0$. Structure at positive values of $\Delta\beta$ indicate misidentified particles of higher mass. At low momentum, a small band of misidentified kaons can be observed between 0 and 0.1 in $\Delta\beta$ and, extending further out, a limited number of misidentified protons can be seen. Finally, a limited sample of correctly identified but mistimed pions, from a different beam bunch, can be observed around $\Delta\beta = 0.1$ parallel to the main intensity in the figure.*

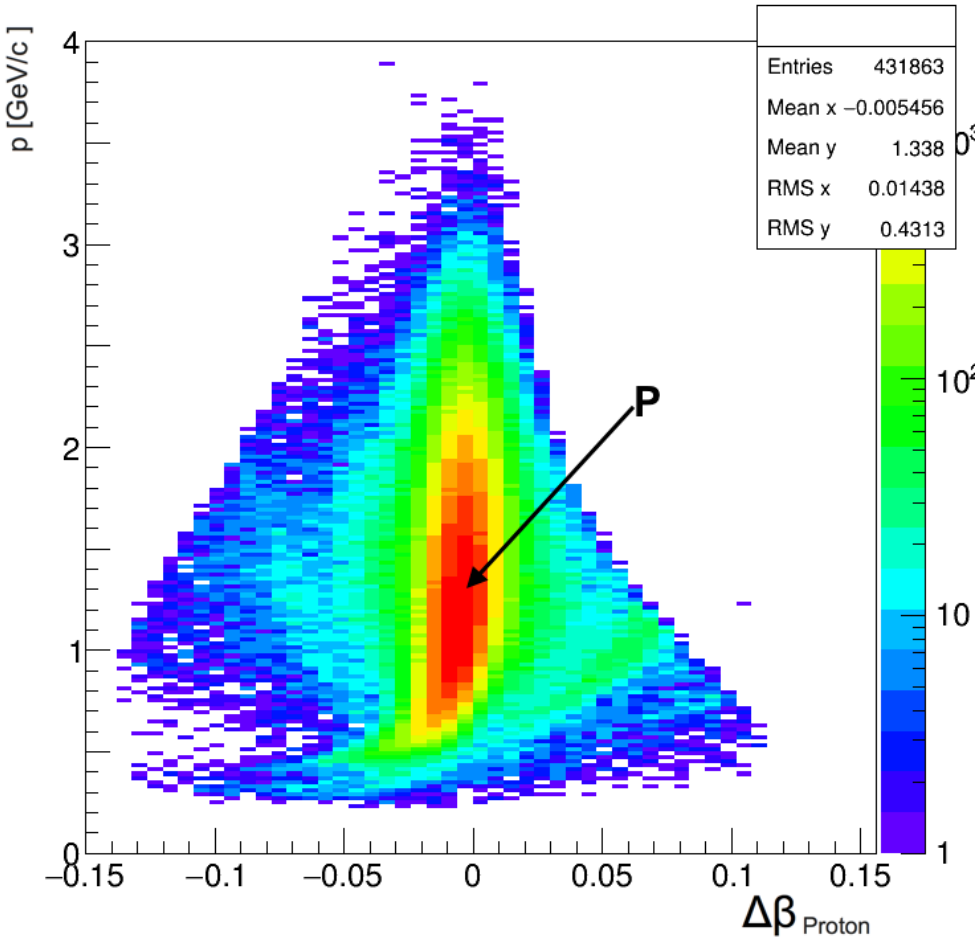

Figure 10.2 *A logarithmic plot of $\Delta\beta$ against momentum for the detected protons. The vast majority of the dataset is correctly resolved, with the intense red region centred around $\Delta\beta = 0$. The additional structure in the plot, most prominently a green band between 0 and 0.05 in $\Delta\beta$ is due to protons which have scattered within the internal structure of CLAS, causing their momentum to be poorly reconstructed.*

multiple occasions throughout the process. However the framework's design allows this to occur more quickly, making use of the TSelector framework in ROOT.

10.5 Code Structure

After the g11a filter code, the skimmed data is split into < 2 GB root files for further analysis.

The rest of the analysis code is split into a number of stages which allow flexibility and the ability for the analysis to diverge at different stages. Shorter codes also allow the programme to be run more efficiently, with only essential stages run each time.

1. Conversion to particle 4 vectors
2. Apply additional data members and corrections
3. Generate histograms or weights
4. Apply background subtraction methodology and generate histograms

The first stage converts the ROOT trees, produced by the filter code, into particle objects in ROOT, incorporating all the critical information such as vertex position, momentum, mass etc. This step simplifies the following physics analysis by creating objects which have a uniform structure for all events. These are then used to select events which correspond to the designated reaction channel of interest, and to discard any events which do not contain exactly the right selection of particles. In addition to these factors, events are selected only if there is merely a single beam photon registered and all registered hits occur within a 2 ns timing window (the gap between beam bunches). These cuts further refine event selection from the cooking process, to minimise desynchronised events.

The second stage of the process generates any additional data of interest, such as the reconstructed ω, and also introduces any necessary corrections or additional frames of reference for particle analysis.

The third and fourth stages are where background subtraction occurs; this will be discussed in more detail in Sections 10.7.1 and 10.7.2.

10.6 Detector Simulations

Monte Carlo simulations are used as complementary sources of data for the ongoing data analysis. They provide a cross check for the significance of any results and are a useful tool to test the consistency of the analysis software.

Simulated 'Pseudo data' is first produced in a 3 step process:

1. Particle Generator
2. Detector Simulation
3. Data Post Production

In the first step, a particle generator was used to create a set of events to be passed through the detector simulation. A program called EdGen, created by Lorenzo Zana, was used to generate these events. The properties of the particles, such as their type, decay route and their distribution in θ and ϕ were customised on each run, to suit the requirements of each simulation [112].

Once generated, the events were passed through the standard GEANT3 based detector simulation of CLAS known as GSIM [113, 114]. This models the physics processes and acceptance effects incurred by real events originating from the target volume, with energies defined in the particle generator.

The simulated events were then passed through the GEANT post production programme known as GPP. This programme reconstructs the events in a similar manner to CLAS cooking; however, first the values produced by the simulation are smeared to match the detector resolution. The exact properties known from the simulation are stored as separate variables,in order to allow properties such as detector acceptance and the quality of particle ID to be determined.

These simulations were used repeatedly throughout the analysis; the specific simulations are discussed in more detail in later sections, where relevant.

10.7 Reaction Selection

10.7.1 $\gamma p \to \omega\pi^+\pi^- p \to \pi^+\pi^-\pi^+\pi^-(\pi^0)p$

Initial studies in this analysis considered the reaction:

$$\gamma p \to \omega\pi^+\pi^- p \to \pi^+\pi^-\pi^+\pi^-(\pi^0)p$$

This requires detection of 5 particles in the final state, with a missing π^0. π^0, which predominantly decays to 2γ, which are poorly detected in CLAS. Reconstructing the properties of the undetected π^0 provides a better selection.

The lifetime of ω is short, $(7.75 \pm 0.07) \times 10^{-23}$ s, resulting in minimal path length between the point of creation and decay. Consequently, within the spatial resolution of CLAS there is no detached vertex for the 3π which originate from the decaying ω. Therefore, all 5π appear to originate from the same point and have to be treated as separate combinations, each potentially arising from the decay of the ω. The combinations are designated based in the order in which the π^- and π^+ are detected within CLAS, in the following scheme:

1. $\pi_1^-\pi_1^+$
2. $\pi_1^-\pi_2^+$
3. $\pi_2^-\pi_1^+$
4. $\pi_2^-\pi_2^+$

Figure 10.3 shows plots of one of the ω candidate combinations (one combination of $\pi^+\pi^-\pi^0$) and Figure 10.4 shows distribution for all four combinations with the same π^0 missing mass cut.

CLAS is a wide acceptance detector able to detect many different types of particle; however, there are areas with no acceptance, such as at angles less than 5° in θ from the beamline, or the regions in the shadow of the toroidal magnets. Even for particles with a high probability of detection, the requirement that all of the final state particles need to be detected limits the statistics available for analysis, as any independent event with one or more particle undetected is excluded. For

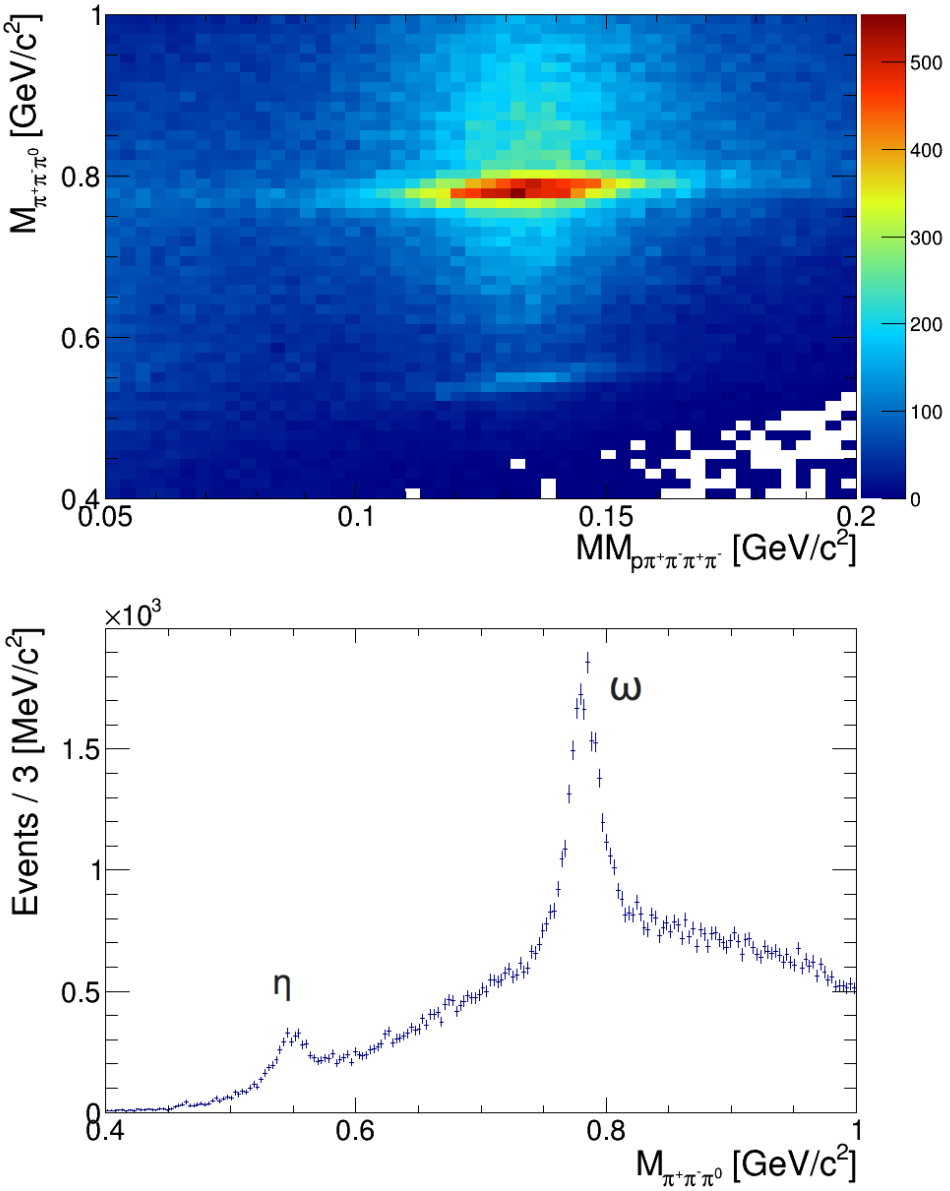

Figure 10.3 *[Upper] A plot of the reconstructed ω vs the missing mass of the reaction, for the highest momentum combination of π^+ and π^- for each event. One of 4 possible combinations of $\pi^+\pi^-$. The intense red region peaks around a mass around 0.78 GeV/c^2 close to the mass of ω, with a missing mass of around 135 MeV/c^2 corresponding to the missing π^0. A smaller peak with the same missing mass occurs around a mass of 0.55 GeV/c^2 showing a contribution from the η meson, which also decays to $\pi^+\pi^-\pi^0$. [Lower] A projection of the 2D plot [Upper] onto the y-axis with a selection on the missing mass of $p\pi^+\pi^-\pi^+\pi^-$ around the mass of π^0. The figure shows a multi pion background with a clear ω peak visible just below 0.8 GeV/c^2 and a smaller peak around the mass of η around 0.55 GeV/c^2.*

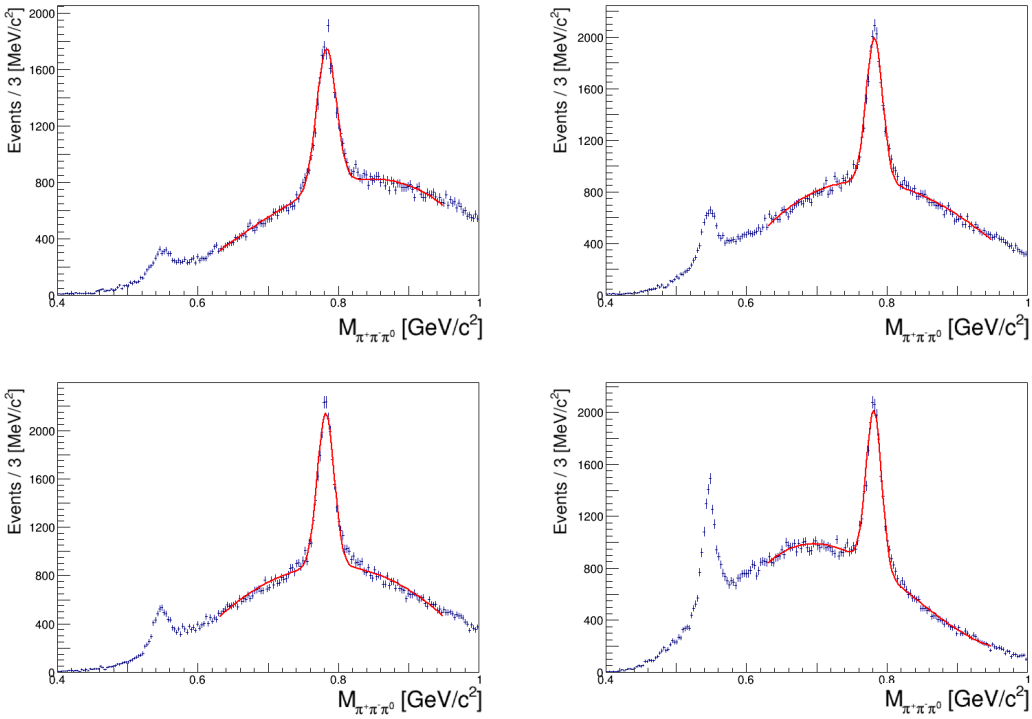

Figure 10.4 *Plots showing distributions of the reconstructed ω mass for the 4 possible combinations of $\pi^+\pi^-$, with a selection on the missing mass of $p\pi^+\pi^-\pi^+\pi^-$ around the mass of π^0. Higher momentum pions are listed first: [Top Left] $\pi_1^-\pi_1^+$, [Top Right] $\pi_1^-\pi_2^+$, [Bottom Left] $\pi_2^-\pi_1^+$ and [Bottom Right] $\pi_2^-\pi_2^+$. A clear ω peak can be observed in each just below 0.8 GeV/c^2, with a peak at the mass of η around 0.55 GeV/c^2, that is more prominent for some combinations. The shape of the multi pion background also fluctuates for each combination, depending on the typical momentum of the pions.*

example, consider 100,000 events entering CLAS, a two-particle final state with both having a 70% chance of detection leaves 49,000 detected. Increasing the number of final state particles reduces the probable number of complete events detected multiplicatively. For example, five final state particles at a 70% detection efficiency would produce 16,807 detections.

During the g11a run, the polarity of the magnetic field used bent positively charged particles away from the beamline and negatively charged particles towards the beamline. Consequently, negatively charged particles were detected only above a minimum production angle in θ. This effect is also positively correlated with the momentum of negative particles; those that are more energetic are more likely to avoid the dead zone around the beampipe. As a result, the cross section to detect negatively charged particles was significantly lower (in simulations the ratio of detected π^- / $\pi^+ \sim 0.55$) and the momentum distribution of these is skewed to higher energies. Figure 10.5 shows a comparison between the true particle ID of generated phase space data and the particle ID of those that were reconstructed after passing through a simulation of the CLAS detector.

This final state is closest to previous literature studies on this channel. However, the harsh requirements of detecting five particles in the final state and the inherent combinatorial background present in the channel led to the decision to move the focus of the analysis away from this final state. Instead the focus was shifted to the reaction:

$$\gamma p \rightarrow \omega \pi^+ \pi^- p \rightarrow (\omega) \pi^+ \pi^- p$$

This final state mode results in vastly increased statistics in the signal region and avoidance of potential bias from combinatorial selection, at the cost of significant increases in background and the signal-to-noise ratio in the dataset. There is also the possibility of introducing acceptance bias as a result of this selection, requiring only one π^+ and one π^- to be detected. This possibility should be kept in mind when considering acceptance corrections to the dataset. However, by utilising more advanced background subtraction techniques, this analysis aims to better understand this decay channel and its possible decay modalities.

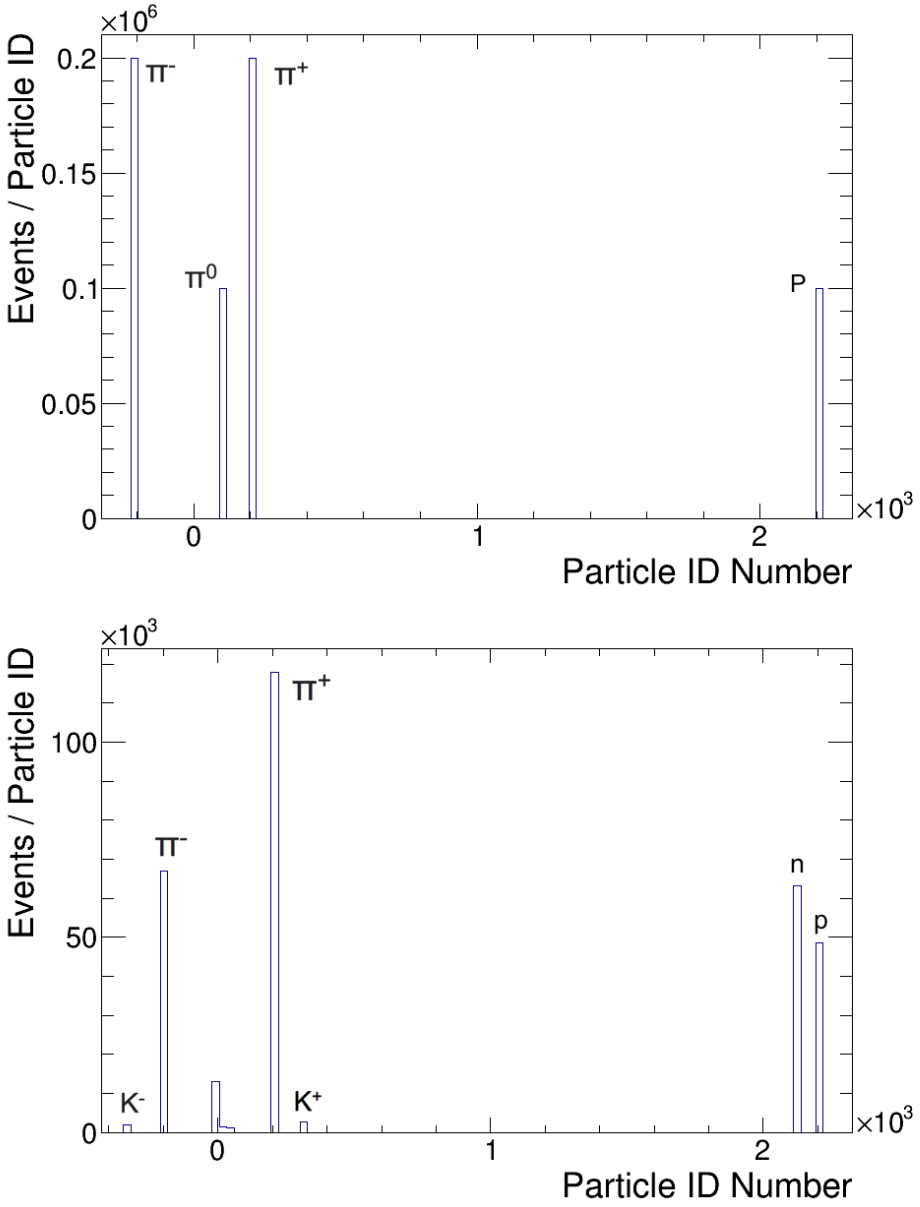

Figure 10.5 *A comparison between generated particle identification, ID, of 100 k phase space Monte Carlo events, [Upper], and the reconstructed particle ID after passing through the CLAS reconstruction simulation, [Lower]. A greater percentage of π^+ (211) than π^- (-211) is detected after passing through CLAS. This is expected from the polarity of the magnetic field during g11a which bent negatively charged particles towards the beamline. As expected, no π^0 particles are detected, but some of the decay γ (22) are reconstructed. Small numbers of electrons(11) and muons (13) are also detected. These are either misidentified, or produced through interaction with the detector system. A small number of pions, misindentified as kaons (311 and -311) is also shown. Finally, the reconstruction shows a large number of neutrons (2112) (although none were incident), a greater number than the reconstructed protons (2212). Some of these will be misidentified protons, but many will instead be energetic photons badly reconstructed in the detector.*

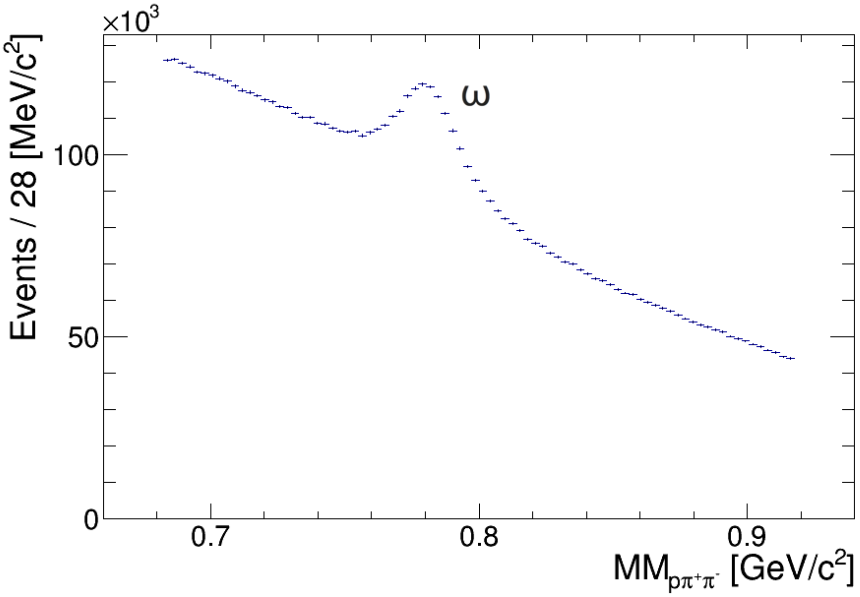

Figure 10.6 *Missing mass distribution for the $\gamma p \to \pi^+\pi^-(\omega)p$ final state for the g11a dataset, centred around the expected mass of ω. A clear ω peak is visible above the background, peaking around 0.78 GeV/c^2.*

10.7.2 $\gamma p \to \omega\pi^+\pi^- p \to (\omega)\pi^+\pi^- p$

This analysis has focused on considering the final state with ω reconstructed and only $p\pi^+\pi^-$ detected in the final state. This final state was selected to greatly increase the available statistics in the signal region, at the cost of increased levels of background. This can be seen clearly in Figure 10.6 for a small sample of the dataset; the ω peak is seen clearly above the background. Filtering of the full dataset used a narrower selection to limit file size and reduce processing time.

This reaction channel avoids selection bias from different combinations; however, a significant fraction of the time, even in a signal event, one or more of the detected pions may have originated from the missing ω. Therefore the combinatorial background must still be taken into account.

With intrinsically higher levels of background, the techniques used to extract the signal contribution are critical. In this analysis two methods were investigated, sideband subtraction and sPlot fitting. These are discussed in more detail in Chapter 11.

10.8 Summary

The process involved in turning the raw data collected from CLAS into a dataset suitable for analysis has been described. This begins with turning the detector results into physics observables and correcting these for any energy and momentum losses between the interaction vertex and the detector. Corrections are also applied for inconsistencies in the response of detector elements. The processed data is then filtered to select a restricted dataset including the reaction of interest, in this case $\gamma p \rightarrow \omega\pi\pi p$. The reduced sample is then converted to 4-vectors for physics analysis and final corrections are applied to prepare the dataset for background subtraction.

Two methods of background subtraction have been used in this study to provide independent methods for analysis. These are discussed in the next chapter in this thesis.

Chapter 11

Signal Selection

This chapter will cover the two different methods of background subtraction used in this analysis, Sideband Subtraction and sPlot Background Subtraction. Utilising two different methods allows the results of each to be compared against one another, providing greater confidence in the significance of any results obtained. Where the two methods disagree, they provide extra information on the cause of the discrepancy, helping to identify possible problems in the analysis.

11.1 Sideband Subtraction

Sideband subtraction is one of the most commonly used methods of background subtraction in hadron physics. The methodology attempts to separate signal events from background in a 'signal region', by subtracting a convolution of the background present in the regions above and below the signal range:

$$Centre_{(Signal)} = Centre_{(Signal+Background)} - Sideband_{(BackgroundNormalised)}.$$

A simple example would be a Gaussian shaped signal, with a background represented by a polynomial which extends across and beyond either side of the signal region. The signal region is defined as the mass range which includes the full width of the signal function, Figure 11.1. The sidebands are regions on either side of the signal region which are purely background, Figure 11.2. To separate

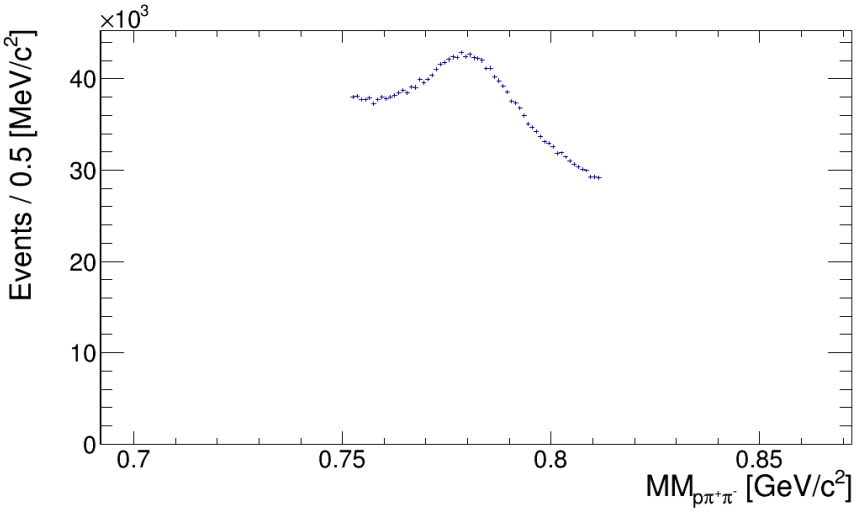

Figure 11.1 *A plot of the data included within the 'signal' region for use in sideband subtraction studies. A clear peak around the mass of the ω meson is seen around 0.78 GeV/c^2, on top of a large multi pion background.*

the signal from the background in the signal region, data is collected from the background on either side of the signal region. The left and right sideband regions are combined and normalised to the magnitude of the background in the signal region. This is then subtracted from results in the signal region, to leave only the signal component in the area.

Sideband subtraction requires that the background can be represented as a continuous function across the sidebands and signal region, allowing the background under a signal peak to be inferred directly from the sideband contributions. It works best when used to identify signal events from a peak well separated from other resonant contributions to the data. If the fraction of signal to background is small - as is the case in this channel - the results are very sensitive to the parametrisation of the signal and sideband regions. Therefore, it is essential that systematic studies are undertaken to ensure the stability of results caused by varying the width, position and normalisation of the sidebands used for determining the background contribution. Without this, artefacts created by statistical variance in the sidebands can dramatically affect the structure of the signal region post subtraction.

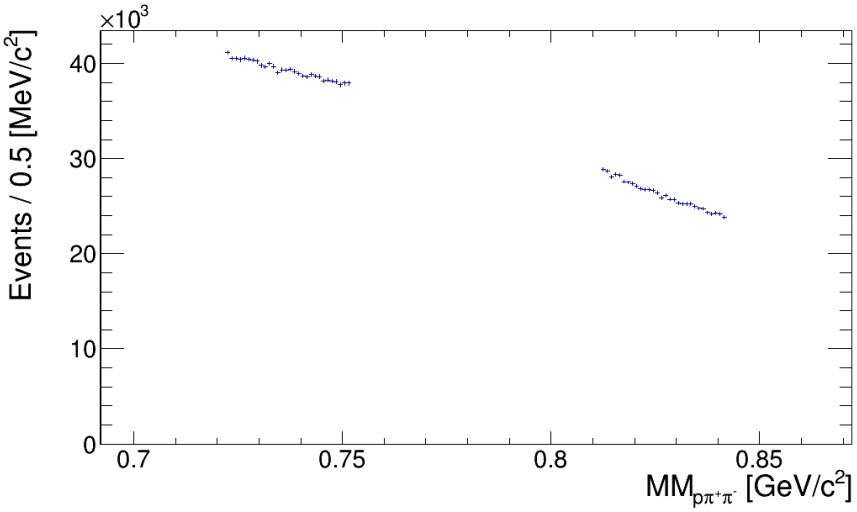

Figure 11.2 *A plot of the data included within the 'sideband' regions for use in sideband subtraction studies. The data can be modelled as a simple polynomial with no significant structure visible.*

11.1.1 Sideband Subtraction Methodology

Sideband subtractions in this analysis were carried out using the missing mass of the system as the discriminating variable. A selection for the signal region is taken by a fit of a convolution of a third order polynomial (background), plus a Gaussian signal in a region around the mass of ω. A Gaussian was selected for the signal function as the width of the ω resonance is narrow, and the detected width is dominated by the resolution of the CLAS detector, which is best represented by a Gaussian function. An example of this is shown in Figure 11.3.

The simplest method of considering the sidebands would be to consider regions on either side of the signal peak, of equal width to the signal region. If the background could be considered as a 1st order polynomial, a sideband subtraction could be simply undertaken, on a bin by bin basis, by summing the contribution of the two sidebands and dividing the total by two, to represent the value of the background in the signal region.

In reality, background functions can rarely be represented well by something as simple as a straight line; the width of the sidebands needs to be varied, to ensure that the stability of the results is not dependent on this quantity. A more sophisticated method for normalising the magnitude of the background contribution involves fitting appropriately the background shape and normalising the contribution of the left and right sidebands, to properly represent the

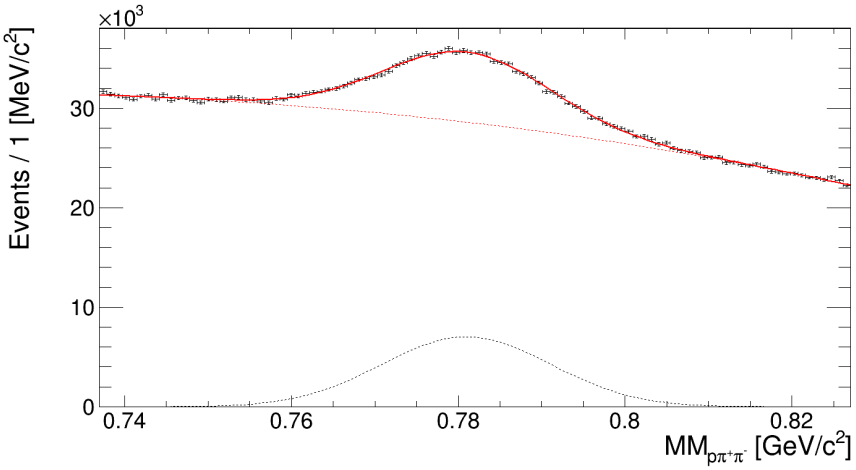

Figure 11.3 *Determining the width of the signal region before sideband selection. The fit to the data is undertaken using a combination of a Gaussian and a 3rd order polynomial. This method uses a similar method of fitting to the initial stage of the sWeights technique discussed in Section 11.2*

magnitude of the background in the signal region. Figure 11.4 shows an example of such a fit.

To normalise accurately sidebands of any width and a background shape, dependent on the cuts applied, a separate fit to each set of changes is required. To achieve this, the sidebands of a given set of data are fitted using the discriminating variable, missing mass, using a 3rd order polynomial, f(x), that describes the shape of the background. The integral of this function in the signal region (bg_{signal}) and in each sideband is then taken. The left (bg_{left}) and right (bg_{right}) sidebands are weighted according to the ratio between their values, and normalised to the magnitude of the integral of the background in the signal region, using the formula shown in Equation 11.1:

$$NormalisationFactor = \frac{\int f(x)_{bg_{signal}}}{\int f(x)_{bg_{left}} + \int f(x)_{bg_{right}}}. \tag{11.1}$$

The values of each bin in the sidebands are multiplied by the normalisation factor, before being summed together and then subtracted from the values of the bins in the signal region.

In the specific case where a histogram being constructed includes the discriminating variable, the bins of the sideband are matched with the most appropriate bins in the signal region. The bin with the lowest energy in the left and right

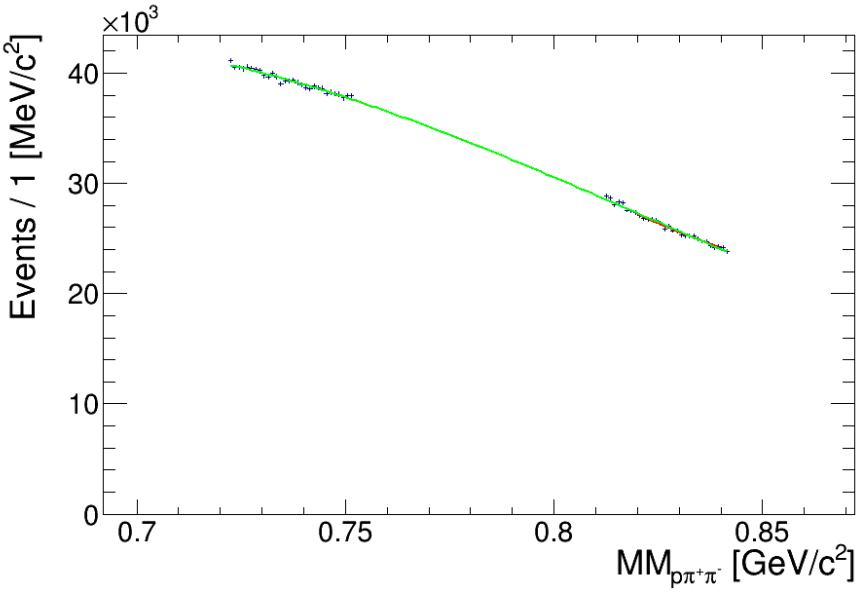

Figure 11.4 *Fitting the background in the sidebands to determine the shape of the background in the signal region using a 3rd order polynomial.*

sidebands would be coupled with the bin of lowest energy in the signal region. If the widths of the sidebands compared to the signal region differ, then the corresponding binning is adjusted, to match for appropriate subtractions across the regions.

11.1.2 Sideband Subtraction Systematic Studies

As previously discussed, sideband subtraction assumes that the background can be treated as a continuous function, and that the two sidebands used for background subtraction are representative of the background in the signal region.

The magnitude of the background subtraction is normalised to the width of its function in the signal region; however, the stability of the subtraction, which is dependent on the width of the sidebands, needs to be tested.

The regions immediately beside the signal region are used to infer the background under the signal. Keeping these narrow reduces the probability of contributions from other significant structures, by attempting to select only the phase space background immediately surrounding the region of interest. However, reducing the size of the sidebands increases statistical uncertainties, by averaging over fewer results and subtracting highly weighted results from the signal region. In an example where the sidebands are much less broad than the signal region, small

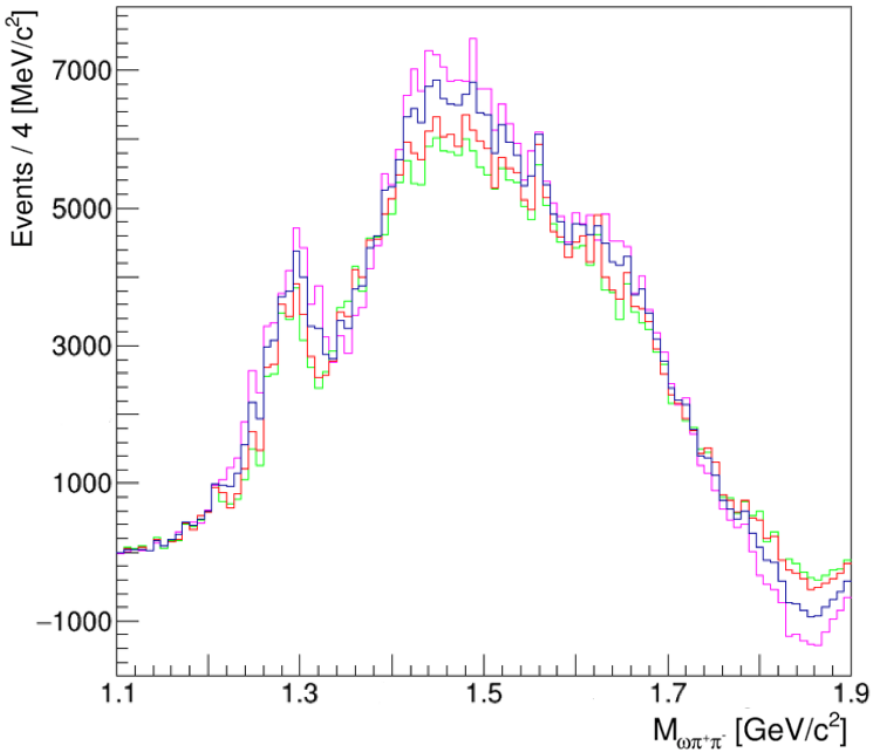

Figure 11.5 *Plots of the mass of $\omega\pi\pi$ for varying widths (SBW) and gaps (SBG) between the signal region and sidebands. Testing the stability of results from sideband subtraction. (SBW,SBG) All numbers in MeV/c^2: Red (30,0), Blue (60,0), Green (15,0), Pink (30,30).*

changes in statistics, or the presence of a localised structure in either sideband, can have a big impact on the background subtracted results.

Figure 11.5 shows the result of a systematic study varying the widths of sidebands used for background subtraction, ranging from the twice the width of the signal region, down to half the width of the signal region. The structure of the datasets remains broadly similar, with a significant peak around 1.3 GeV/c^2, protruding from a distribution that rises to a maximum around 1.45 GeV/c^2, before falling away with an enhanced shoulder around 1.65 GeV/c^2, and finally shows evidence of over subtraction at high mass values around 1.85 GeV/c^2. The choice of sideband width can enhance some of these features; for example, quite clearly at high mass, wider sidebands selection (shown in pink and blue) result in significant over subtractions, due to the extended kinematic range of the wider sidebands.

Considering the results of these studies and the inspection of the structure of the background distributions, a compromise was selected, with each sideband covering

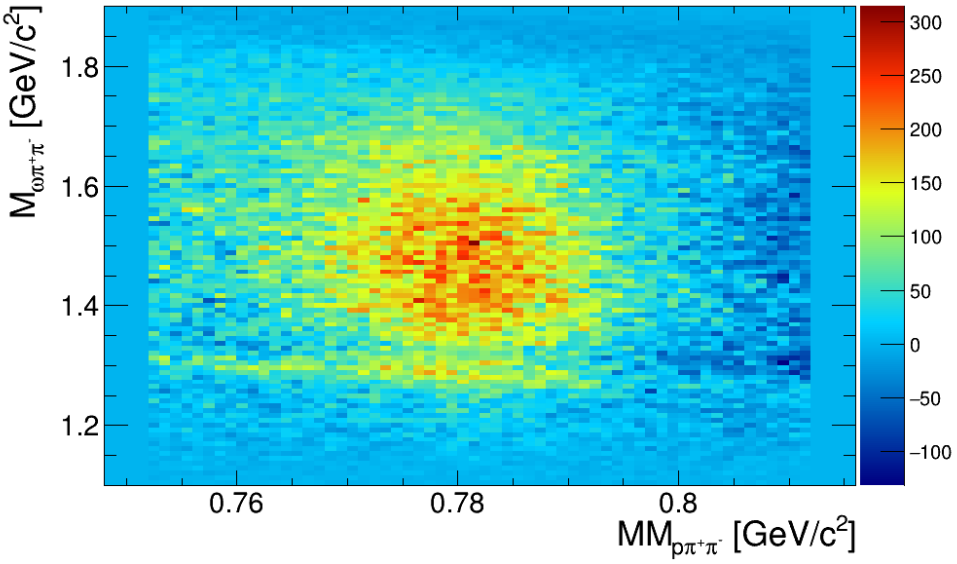

Figure 11.6 *A combination of 10 sideband subtraction studies on $MM_{p\pi^+\pi^-}$ binned in the mass of $\omega\pi\pi$. The distribution is well centered around the mass of ω on the x-axis for all bins, with some correlation observed between the 2 quantities, most obviously in the band around 1.3 GeV/c^2 in the mass of $\omega\pi\pi$. Some consistent over-subtraction is also observed at higher values of $MM_{p\pi^+\pi^-}$.*

an area half the width of the signal region. This avoids any significant variations in the background shape, whilst including sufficient statistics to minimise statistical errors.

Two Dimensional Mass($\omega\pi\pi$) vs Missing Mass($p\pi^+\pi^-$)

The analysis in this thesis relies on reconstructing the missing ω from the missing mass of the $p\pi^+\pi^-$ system, and using this to investigate higher mass resonances which decay to this state. As a result, there is a strong dependence between the quality of the reconstruction of the ω and the significance of inferences about possible $\omega\pi\pi$ resonances. To investigate this further, the $M(\omega\pi\pi)$ was investigated as a function of the ω mass. The dataset was split into 10 bins in M($\omega\pi\pi$) and each of these underwent separate fitting and sideband subtraction, in order to allow for any variance in the shape of the signal and background for different ranges of M($\omega\pi\pi$). The results of the 10 separate bins are combined together and shown in Figure 11.6.

The general features of the distribution indicate that it is well situated around

the centre of the ω mass at 0.782 GeV/c^2. However, there is clear evidence of some over-subtraction at higher values of ω mass (seen as the dark blue regions on the plot), and probably some corresponding under-subtraction at lower values of ω mass. This produces some systematic bias towards any background effects occurring at lower mass of ω. In addition, there is a slight but significant negative correlation between the mass of $\omega\pi\pi$ and the mass of ω, most clearly seen by considering the band around 1.3 GeV/c^2, which produces the clear peak in the one dimensional plot of M($\omega\pi\pi$). This is due to a standard correction applied to the reconstructed ω, to set its mass to its known mass. Looking closely at the band, it is symmetrical about the centre of the plot, with its slope proportional to the difference between the measured and set value of the ω mass. Finally of significance in this plot is the distribution of the band at $\sim$ 1.3 GeV/c^2. It peaks at the centre of the mass of ω, with a distribution following a broadly Gaussian shape across the range, when allowing for some over-subtraction at higher values of the mass of ω. The symmetry of this distribution indicates that this structure may be a product of decay from an ω meson; it is less likely to be an artefact introduced by asymmetric sideband subtractions.

11.2 sPlot Background Subtraction

Another widely used methodology for background subtraction is called sPlot. The basis of this technique is that a distribution can be described by a combination of functions that represent different species of events. Each event in the distribution can then be assigned a sWeight which values its contribution to the signal or background portions of a distribution. Multiplying each event by the calculated sWeights can then be used to construct distributions of other uncorrelated variables.

A simple example would be a Gaussian shaped signal peak with a flat background function for the mass of a particle. Fitting the distribution with a combination of these functions allows the signal events of interest to be separated out, and the distribution of the contributing factors reconstructed. sWeights generated from the fit to the mass spectrum could then be used to construct the scatter distribution in ϕ for the same dataset, separating the signal and background contributions.

To properly reproduce distributions, sPlot requires that the discriminating

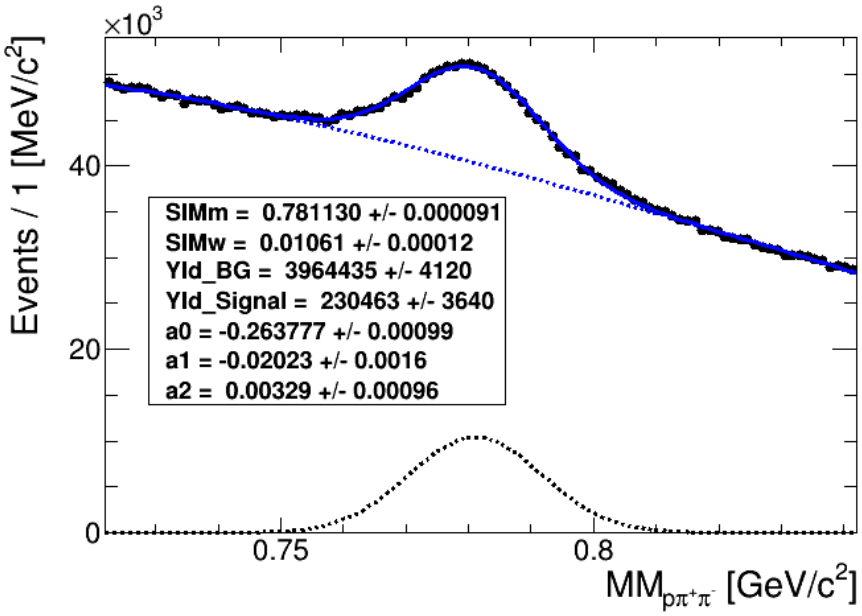

Figure 11.7 *sWeights fit to a discriminating variable $MM_{p\pi^+\pi^-}$, using a Gaussian and a 3rd order Chebyshev polynomial. The ω signal peak (SIMm) is resolved to within 0.01 GeV/c^2 of the PDG value. The width (SIMw) is also in good agreement with literature values for ω, within the limits of the resolution of CLAS.*

variable used for fitting is uncorrelated to other variables of interest. If there is a correlation, then systematic errors are introduced which can be difficult to quantify. A deeper discussion on the methodology and its merits can be found in [115].

11.2.1 sPlot for $\omega\pi\pi$

The missing mass of the reaction was selected as the discriminatory variable, fitting around the ω mass peak to discriminate signal from background. Accurately fitting the dataset is essential for the successful use of sPlot, as all results are dependent on the quality of the fit to the discriminating variable. A combination of a Gaussian signal function and a 3rd order Chebyshev polynomial was found to be the best fit combination for the dataset. A Chebyshev polynomial was selected over a regular polynomial, because they are less prone to approximation errors introduced by fitting with polynomials of higher orders. An example of this fit to the dataset is shown in Figure 11.7, along with the functions used for signal and background.

The mass range used for the background fit was varied in each study, in order

to test the stability of results. Restriction of the background fit mass range to no more than three times the full width of the signal function ensured that the effect of processes far from the signal region, and probably not present in the ω mass region, were minimised. For each set of parameters, the process of fitting was carried out ten times, with varied initial parameters, to try to find the global likelihood maxima rather than just a local one. For each set of cuts, new fits and separate sWeights were calculated, to ensure that results were as accurate as possible to the particular restricted dataset.

One of the main aims of this study is to consider resonant states of $\omega\pi\pi$. However, when using sWeights this creates a problem, as there is an inherent correlation between the missing mass used as the discriminating variable and the mass of $\omega\pi\pi$. As discussed in section 11.2, using sWeights with variables that are correlated with the discriminating variable introduces systematic errors that need to be accounted for. To help adjust for this error, the fit to the missing mass is split into ten mass bins in $M(\omega\pi\pi)$, with the top and bottom mass two bins twice combined, because of limited statistics, and separate fits are carried out for each dataset. The number of bins used is a balance between statistical uncertainty and the significance of the effect of the correlation.

11.2.2 sPlot Systematic Studies

Finding a function to accurately fit the data is essential to properly determine appropriate sWeights for the dataset. To ensure this, several types of function were tested before settling on 3rd order polynomial for the background and a Gaussian for the signal function. For a narrow resonance such as ω, the width of the peak is dominated by the detector resolution, therefore a Gaussian should most closely represent the shape of the signal distribution. The widths of the background function modelled were selected in line with the choices made for sideband subtraction, to minimize the effects of artefacts in the background and to allow both methodologies to be directly compared. In addition, every time a fit was undertaken, the process was repeated ten times, with varying initial parameters, to try to find the best available option.

11.3 Summary

Two different methodologies of background subtraction have been discussed which will be used separately throughout this analysis. Sideband subtraction proposes determining the background contribution under a signal as a convolution of the background in a region either side of the signal region (the sidebands), which can then be normalised and subtracted to leave the separated signal. sPlot background subtraction describes a distribution as a combination of a signal function and a background function for a particular discriminatory variable. The results of these distributions can then be used to weight the data (sWeights) on an event by event basis, and to reconstruct the distributions of other variables of interest. However, where there is correlation between the discriminatory variable and another variable of interest, systematic errors are introduced, which can be mitigated by binning in the variable and carrying out multiple fits for each bin.

Throughout most of the results section of this analysis, which follows in Chapter 12, the impact of both methods of sideband subtraction have been compared. This provides further insight into the results of each technique, based on the variance between the two methods.

Chapter 12

Results

In this section, the results of the analysis will be presented. Those obtained using both sideband subtraction and the sPlot technique for background subtraction will be presented together in each section for ease of comparison. The structure of the results section of this analysis is as follows:

- Section 12.1 is focused on the search for resonanances decaying to $\omega\pi\pi$ by considering the mass distribution for the combined reconstructed ω and the two detected pions. This is covered for 3 regions in both beam energy and t.
- Section 12.2 covers a Monte Carlo simulation of decays of the $a_2(1320) \rightarrow \omega\pi\pi$.
- Section 12.3 presents a simulation into a possible background channel $\eta(1295) \rightarrow \omega\pi\pi$.
- Section 12.4 describes a study looking for resonant contributions to the $\omega\pi\pi$ mass distribution decaying via $b_1(1235)\pi$.
- Section 12.5 also covers searches for resonant contributions to the $\omega\pi\pi$ mass distribution but for decays via $\omega\rho \rightarrow \omega\pi\pi$.
- Section 12.6 presents a study into the effects of detector acceptance using a phase space Monte Carlo Simulation of $\gamma p \rightarrow \omega\pi\pi p$.
- Section 12.7 will cover an exploratory study into the use of Van Hove Plots to separate decay modes based on the kinematics of the reaction.

12.1 The Reconstructed Mass($\omega\pi\pi$)

The first area to be discussed is possible resonant states observed in the reaction:

$$\gamma p \to Xp \to \omega\pi\pi p \tag{12.1}$$

where X is an intermediate excited state which could be a meson of higher mass, such as the $a_2(1320)$, which is known to decay to $\omega\pi\pi$. A full list of possible meson decays in the available energy range is shown in Table 9.2. The combined $\omega\pi\pi$ is constructed from the reconstructed ω and the two detected pions.

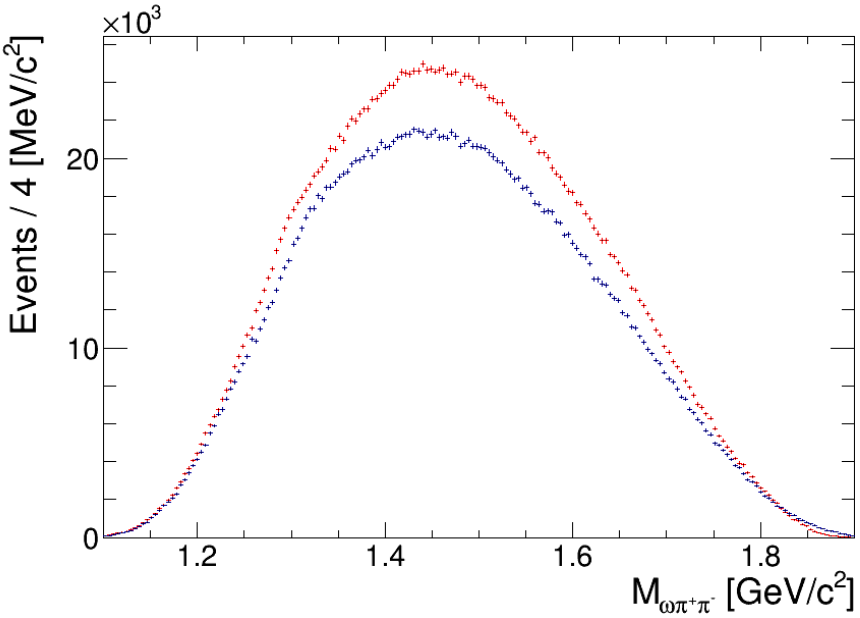

Figure 12.1 *Mass($\omega\pi\pi$) signal region (red) and sideband regions (blue).*

12.1.1 Sideband Subtraction Results

$\omega\pi\pi$ photoproduction has a threshold of $E_\gamma = 1.1$ GeV. Plots for reconstructed ω candidates between $M_\omega = 0.752 - 0.812$ GeV/c^2 around the mass of ω and the sideband regions, before normalisation, are shown in Figure 12.1. Because of the large proportion of background in the signal region, there is little obvious structure in Figure 12.1. However, once the sideband subtraction is carried out, several significant structures are obvious; these provide hints of resonant contributions in addition to the multi pion background. This is shown in Figure

A purely phase space distribution of the $\omega\pi\pi$ system is expected to follow a smooth curve rising up before tailing off, Figure 12.5. However the sideband subtracted mass of $\omega\pi\pi$, Figure 12.2, shows clear structure, most obviously a peak just below 1300 MeV/c^2 and a shoulder to the distribution around 1650 MeV/c^2.

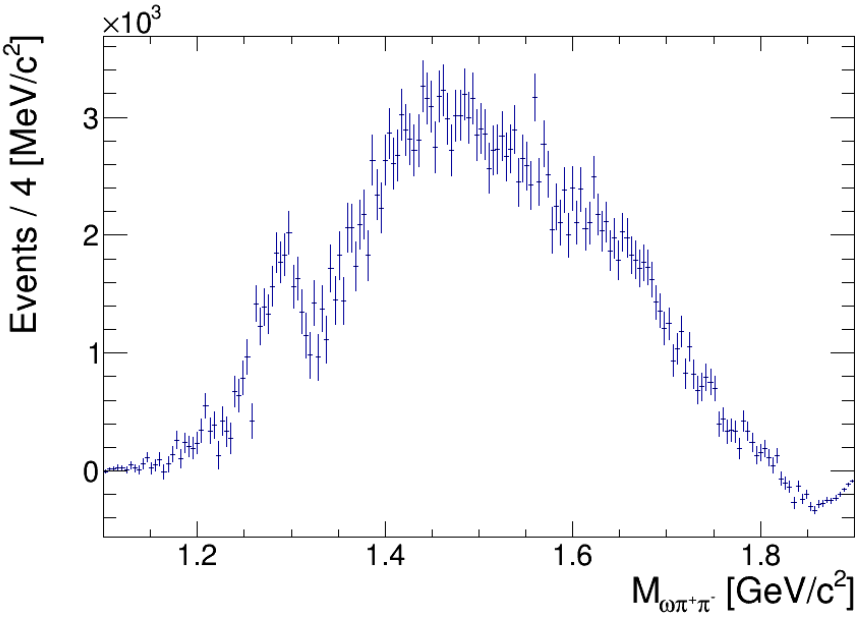

Figure 12.2 *The signal region of Mass($\omega\pi\pi$) after sideband subtraction. A clear peak is visible centred just below 1.3 GeV/c^2, with a shoulder to the distribution around 1.65 GeV/c^2. Negative values occur at high mass values due to over subtraction. This is because the greater kinematic range of the upper sideband distorts the distribution.*

The obvious candidate of interest for the peak around 1.3 GeV/c^2 is the $a_2(1320)$ which decays directly to $\omega\pi\pi$. However, this peak in the data occurs around 30 MeV/c^2, below the established mass of $a_2(1320)$. The width of the peak is also considerably narrower than the 107 ± 2 width of the $a_2(1320)$ [5]. A Monte Carlo simulation of a $a_2(1320)$ dataset is covered in Section 12.2, where possible explanations for these discrepancies are discussed.

The enhancement seen around 1650 GeV/c^2 is in line with 5 possible decay channels, $\pi_1(1600), \omega(1650)$, $\omega_3(1670)$, $\pi_2(1670)$ and $\Phi(1680)$. However all of these are broad resonances, each with limited experimental results to determine their properties. In addition, any structure seen, if due to a resonance, may result from a combination of the above states. Disentangling these contributions would require higher level analysis, such as partial wave analysis, which could identify

the states from their quantum numbers.

Also of interest is the region between 1.4 and 1.5 GeV/c^2, because the $\omega(1420)$ and the $a_0(1450)$ are predicted to decay via this channel. However, any structure is less pronounced and would be a convolution of the two contributions, along with the multi pion background. Again, higher level partial wave analysis would be required to untangle these decay resonances.

It should be noted that at high energies there is some over-subtraction, resulting in 'negative' yields. This is because of the phase space range available to events that occur in the higher mass sideband, when compared to the signal region. The same trend can be observed towards the phase space limit for all the plots in this section. The consequence of this issue is a reduced confidence in any of the results towards the limit of the mass range above around 1.7 GeV/c^2 for these figures. The primary focus of this analysis will be in regions well away from this range, where the statistics are much higher and phase space limitations have a minimal contribution.

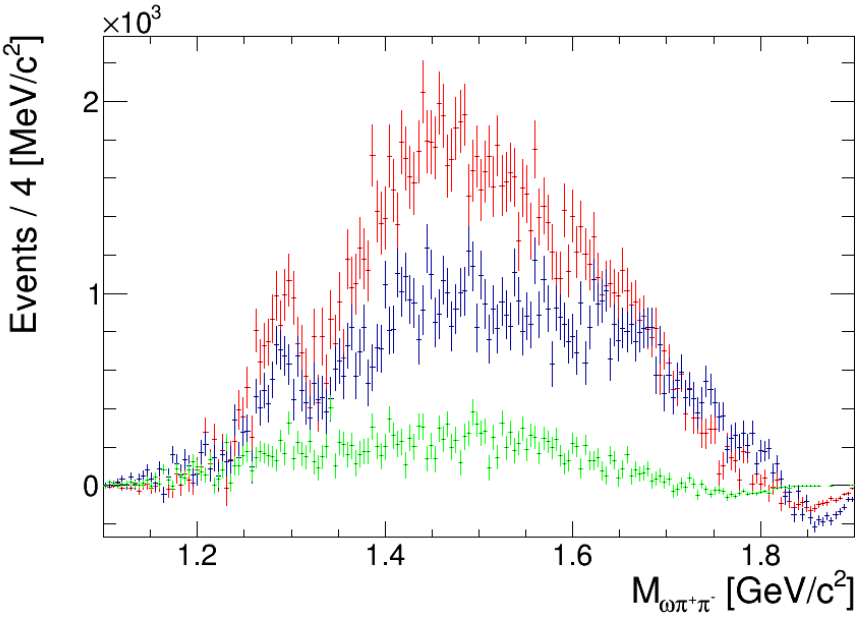

Figure 12.3 *Comparison of Mass($\omega\pi\pi$) after sideband subtraction for 3 ranges of t: [0-1] GeV^2/c^4 (red), [1-2] GeV^2/c^4 (blue), and [3-5] GeV^2/c^4 (green) GeV^2/c^4 values of t.*

Mass($\omega\pi\pi$) Binned in t

The t observable reflects the momentum transferred in the reaction process. For the t-channel meson production, it is expected that the processes should be enhanced at small t. Figure 12.3 shows the distribution of $\omega\pi\pi$ for low, 0-1 GeV^2/c^4, middle, 1-2 GeV^2/c^4, and high, 2-4 GeV^2/c^4, values of t. The contribution to the peak just below 1.3 GeV/c^2 is enhanced at values of t=0-2 GeV^2/c^4 in t. This is indicative of a meson resonant contribution to the structure. The distribution for t=0-1 GeV^2/c^4 has an enhanced contribution between 1.35 and 1.6 GeV/c^2, in comparison to the middle and high distributions, which are comparatively flat between 1.4 and 1.6 GeV/c^2. The distribution of t=1-2 GeV^2/c^4 contains a greater contribution to the mass range around 1.65 GeV/c^2, where several $\omega\pi\pi$ resonances occur.

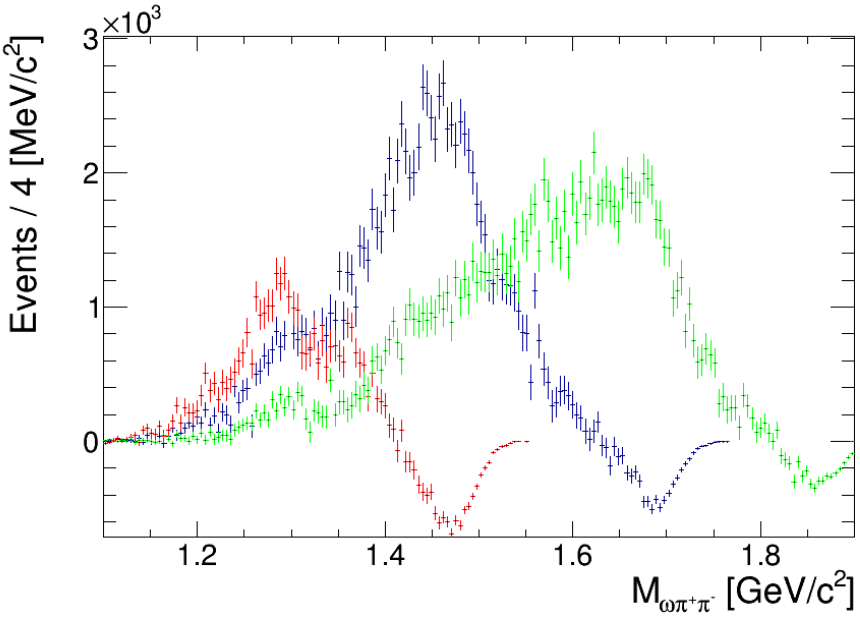

Figure 12.4 *Comparison of Mass($\omega\pi\pi$) after sideband subtraction for low(red), 1.5-2.7 GeV, medium(blue), 2.7-3.3 GeV, and high(green), 3.3-3.9 GeV, values of beam energy. Higher beam energies strongly correlate with a higher mass in $\omega\pi\pi$, as would be expected.*

Mass($\omega\pi\pi$) binned in beam energy

The beam energy constrains the possible kinematics of a reaction and can also influence the reaction mechanism. Figure 12.4 shows the distribution of $\omega\pi\pi$ for low, 1.5-2.7 GeV, middle, 2.7-3.3 GeV and high, 3.3-3.9 GeV, values of beam

energy. Higher beam energies strongly correlate with a higher mass in $\omega\pi\pi$, as would be expected.

The contribution to the peak around 1.3 GeV/c^2 is dominated by the lower energy events highlighted in red, and, to a lesser degree, by the middle energy events marked in blue. However, even in the high beam energy range 3.3-3.9 GeV, there is a visible enhancement just below 1.3 GeV/c^2.

Mass($\omega\pi\pi$) phase space Monte Carlo

For comparison to the experimental data, an $\omega\pi\pi$ phase space simulation passing 10 million events through CLAS was also processed through the same analysis code. The sideband subtracted plot of $\omega\pi\pi$ is shown in Figure 12.5. Limited structure is observed, with the simulated data following a similar distribution to the background samples from the main dataset. However, the statistics available for analysis from this simulation are much lower than the for the experimental dataset.

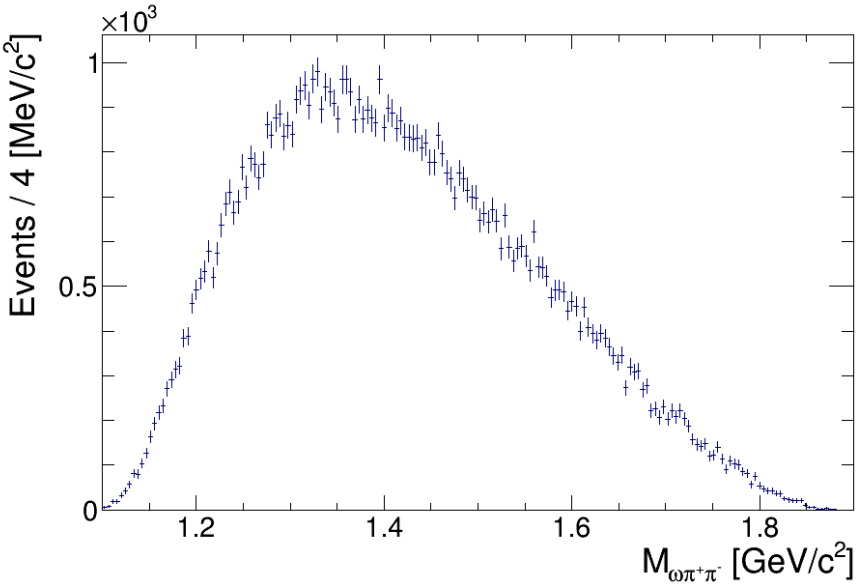

Figure 12.5 *Mass($\omega\pi\pi$) after sideband subtraction for a phase space Monte Carlo dataset of 10 million events.*

12.1.2 sPlot Comparison

This section covers the same $\omega\pi\pi$ reconstruction, but using sPlot signal and background separation rather than the sideband method.

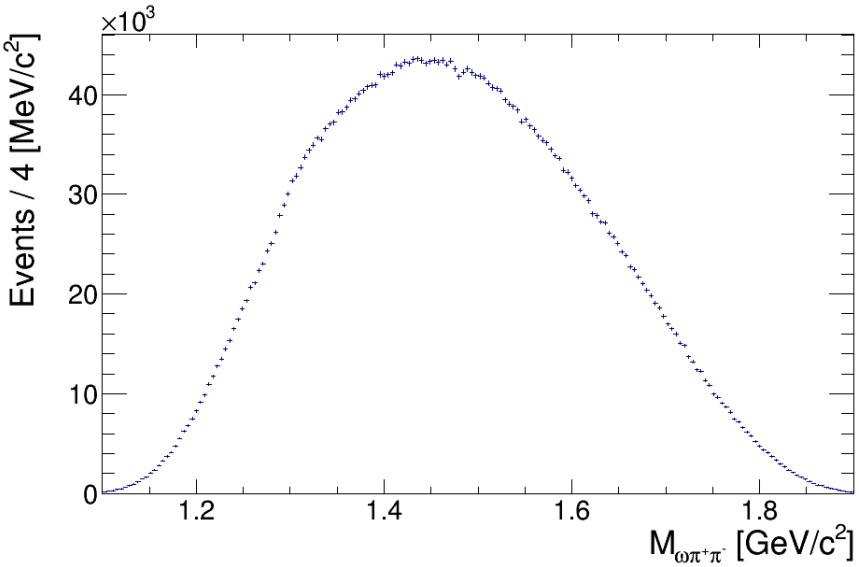

Figure 12.6 *The extracted background Mass($\omega\pi\pi$) spectrum after sWeights are applied. No significant structures are observed, as would be expected.*

The background extracted using the sWeighted dataset is shown in Figure 12.6. This distribution shows a smooth spread across the energy range, with little indication of structure.

The background subtracted yield is shown in Figure 12.7. The general shape is similar to the results from sideband subtraction. There is an enhancement at around 1.3 GeV/c^2; however it is less sharply defined than in the results from sideband subtraction. There is also evidence of a shoulder to the distribution occurring in the range close to 1.65 GeV/c^2.

Similar distributions to Figures 12.3 and 12.4 are observed in Figures 12.8 and 12.9 this time for sWeighted distributions, rather than for sideband subtracted data. Contribution to the structure around 1.3 GeV/c^2 is again dominated by events at lower t and beam energy. Middle values of t are more biased towards outcomes with higher values of $\omega\pi\pi$ mass in comparison to low t. The range of $\omega\pi\pi$ mass accessible is also still highly correlated with beam energy.

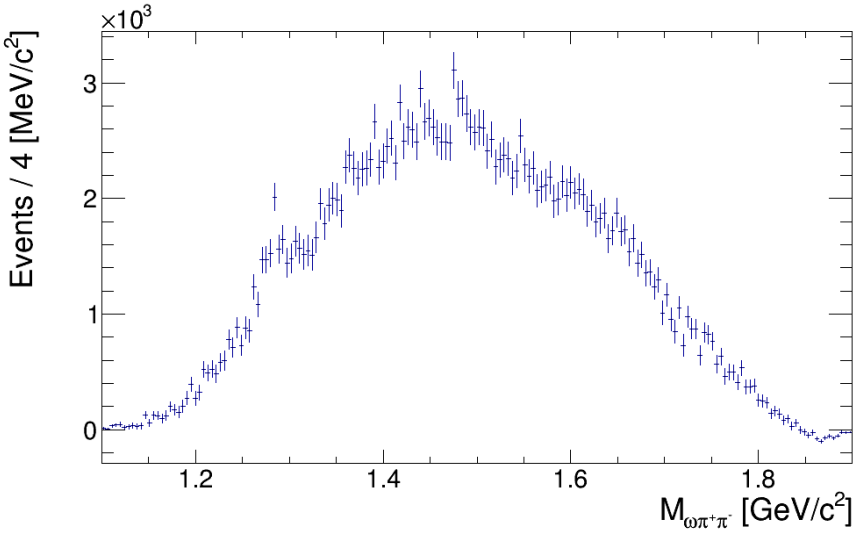

Figure 12.7 *The separated signal Mass($\omega\pi\pi$) after sWeights are applied. Note the enhancement around 1.3 GeV/c^2 and the shoulder around 1.65 GeV/c^2.*

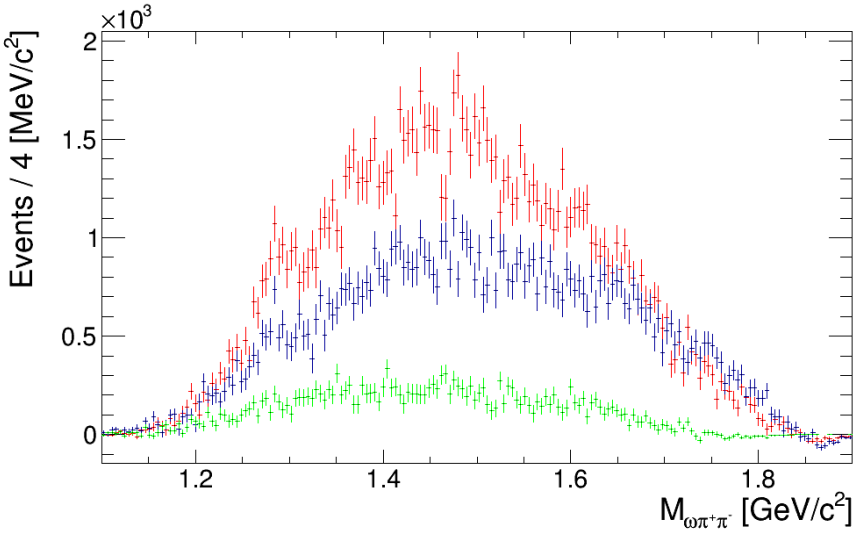

Figure 12.8 *Comparison of Mass($\omega\pi\pi$) after sWeights are applied for 3 ranges of t: [0-1] GeV^2/c^4 (red), [1-2] GeV^2/c^4 (blue), and [3-5] GeV^2/c^4 (green) GeV^2/c^4 values of t.*

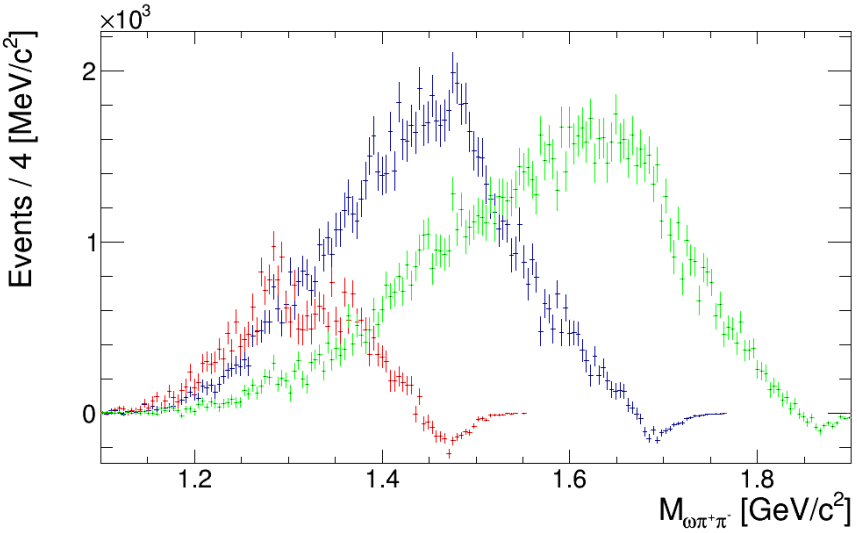

Figure 12.9 *Comparison of Mass($\omega\pi\pi$) after sWeights are applied for three ranges of beam energy: 1.5-2.7(red), 2.7-3.3(blue), and 3.3-3.9(green) GeV.*

12.1.3 Comparing Mass($\omega\pi\pi$) for the two methods of background subtraction

The signal portion of the dataset, after sWeights are applied, is shown in comparison to the sideband subtracted result

The mass of the $\omega\pi\pi$ system for sideband subtracted and sWeighted data are compared in Figure 12.10. The two methodologies extract very similar yields, $\sim 239k$ for the sideband subtracted data and $\sim 238k$ for the sWeighted dataset.

Between 1.1 and 1.28 GeV/c^2 the distributions agree well, within statistical errors. Both also have significant structure occurring around 1.3 GeV/c^2. However, in the sWeighted dataset there is no dip, simply a shoulder in the dataset after the rapid rise. This disagreement is in a significant region, around where resonant contributions as a result of the $a_2(1320)$ are expected to occur.

Between 1.4 and 1.7 GeV/c^2 the datasets follow similar trends, although the sideband subtracted dataset is around 10% higher than the sWeighted data. Both also have a shoulder in the region of interest around 1.65 GeV/c^2, where multiple resonances are expected to be significant. Beyond 1.7 GeV/c^2, the sideband subtracted dataset becomes more unreliable, as phase space limitations start to significantly impact the shape of the distribution, culminating in the negative values observed above 1.8 GeV/c^2.

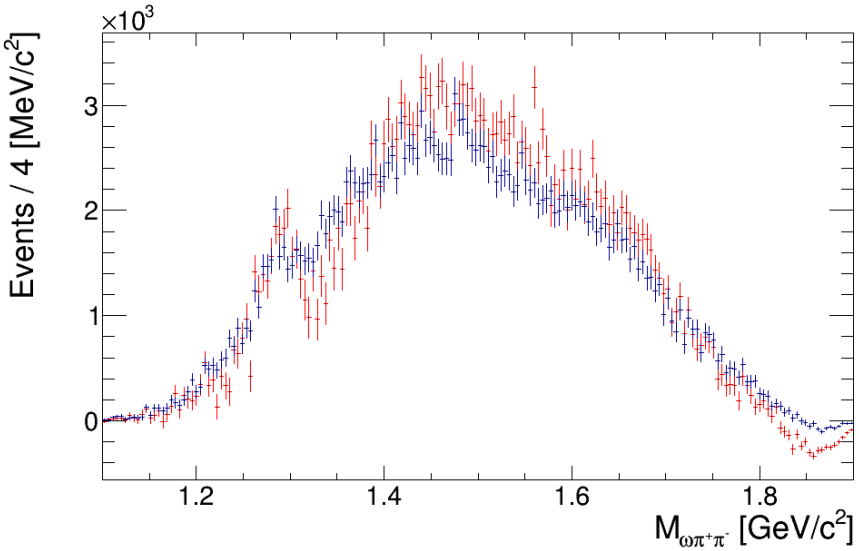

Figure 12.10 *Comparison between the distribution of Mass($\omega\pi\pi$) after sideband subtraction (red) and with sWeights applied (blue). The datasets follow similar trends with significant divergences around 1.3 GeV/c^2 and around 1.8-1.9 GeV/c^2. Detailed analysis in Section 12.1.3.*

12.2 Exploring the structure around 1.3 GeV/c^2 in the mass of $\omega\pi\pi$

To better understand the $a_2(1320)$ candidate peak for the reconstructed $\omega\pi\pi$, Figure 12.2, a Monte Carlo simulation was carried out for events decaying from a $a_2(1320)$ to $\omega\pi\pi$. A million events were generated, passed through the reconstruction of CLAS and the analysis code, in the same manner as for the phase space simulations. The sideband subtraction carried out on this dataset, reconstructed $\omega\pi\pi$ to produce a clean $a_2(1320)$ peak, with a mass of 1318 ± 7 MeV/c^2 and a FWHM width of 75 ± 2 MeV/c^2 FWHM. This is right on the expected mass for the particle, however the width is narrower than the 107 ± 5 MeV/c^2 listed by PDG [5]. The narrower width seems to be due to over-subtraction on the right side of the peak, as the distribution falls away rapidly in this region, in comparison to the generated Monte Carlo. This may provide an explanation to the shape of the $\omega\pi\pi$ distribution in this region observed in Figure 12.10, because an unexpectedly narrow peak is also observed in the sideband subtracted dataset.

Figure 12.11 shows the generated mass distribution before reconstruction and

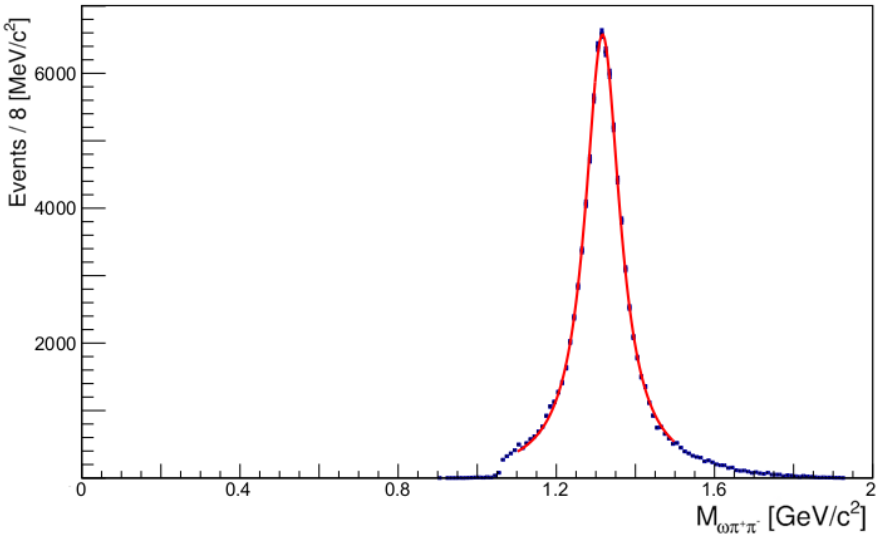

Figure 12.11 *The generated Mass($\omega\pi\pi$) for $a_2(1320)$ from the Monte Carlo data before being passed through the reconstruction of CLAS.*

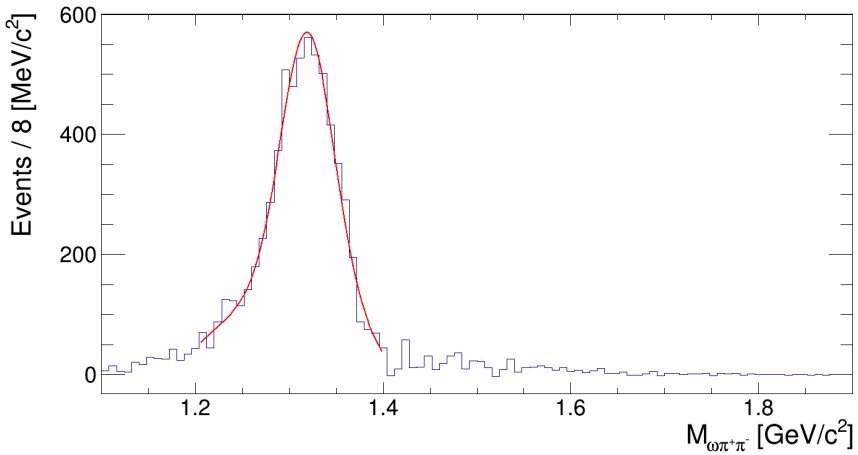

Figure 12.12 *Mass($\omega\pi\pi$) after sideband subtraction for the reconstructed $a_2(1320)$ Monte Carlo dataset after passing through the analysis framework. A clear peak at the $a_2(1320)$ mass is recovered, however it is narrower than the input from the generated dataset.*

Figure 12.12 shows the $\omega\pi\pi$ distribution after passing through the reconstruction code and analysis software.

It should be noted that, in comparison to the dataset, the signal to background ratio in this simulation was very large, with only a limited background, resulting from the resolution of the CLAS detector and limitations in reconstruction. This does not discount the possible effect of the background subtraction methodology. However, systematic studies of the method indicated that this structure is not only a result of a particular set of parameters for the background subtraction, but a consistent peak in the dataset.

12.3 Study of the $\eta(1295)$ Background

Sideband subtraction assumes that the contribution of background channels is a continuous function across the signal region. However, if a structure is significant in only one sideband, it may cause distortions to the signal region after subtraction. These background induced artefacts can lead to misleading results.

To study this situation further and to gain additional insight into the peak observed around 1.3 GeV/c^2 in the $\omega\pi\pi$ spectrum, a Monte Carlo simulation was conducted of 600k events of the process:

$$\gamma p \rightarrow \eta(1295)p \rightarrow \eta\pi^+\pi^- p \rightarrow \pi^+\pi^-\pi^0\pi^+\pi^- p \tag{12.2}$$

This process has the same final state as the dataset used in this analysis, but it should be excluded by the selection of $\pi^+\pi^-\pi^0$ around the mass of ω and the subsequent background subtraction.

The events were generated and passed through the simulation of CLAS, before passing through the same filtering, corrections and analysis process as the real data. Figure 12.13 shows the reconstruction of the missing mass for the final state with $p\pi^+\pi^-$ detected and $\pi^+\pi^-\pi^0$ missing. The figure shows a clear peak at the mass of η, with low and high energy tails. These are caused by a combination of detector resolution and pion combinatorial background, resulting from selecting a pair of pions that did not both decay from the η. Significantly, the high energy tail extends beyond the region of the mass of an ω, indicating that results from

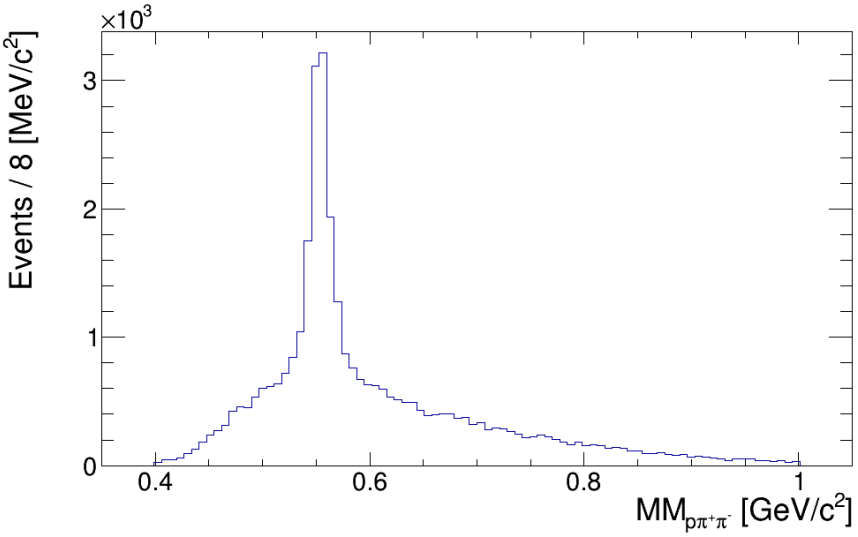

Figure 12.13 *Missing mass spread of simulated $\eta(1295)$ decays to $\eta\pi\pi$ after passing through CLAS, and reconstruction of the decays. A dominant η peak is prominent over a misidentified multi-pion background. The tail of the background extends to high energies, crossing the ω mass region.*

this decay channel could contribute to the main dataset used in this analysis.

The simulated results are processed through the analysis code, selecting events as if they were pions produced from ω decays. If the tail of the distribution would allow the $\eta(1295)$ to be reconstructed, a peak would be observed at its mass in the distribution of $\pi^+\pi^-(\eta)$. The analysis code is not able to differentiate directly between the tail of the missing η and a missing ω. It relies on background subtraction to suppress this contribution.

The results from analysing the $\eta(1295)$ pseudo-events with the $\omega\pi\pi$ analysis code are shown in Figure 12.14. Before sideband subtraction, the distribution is heavily weighted towards lower energies, peaking at around 1.3 GeV/c^2. However, after subtraction there is only a very minimal sample of events remaining, with no clear structure appearing around 1.3 GeV/c^2. Within the limits of the statistics available, this provides some further evidence that sideband subtraction can deal with the effect of background tails extending into the ω mass region. This also limits the likelihood that the peak seen at 1.3 GeV/c^2 in the $\omega\pi\pi$ spectrum is due to an artefact such as this.

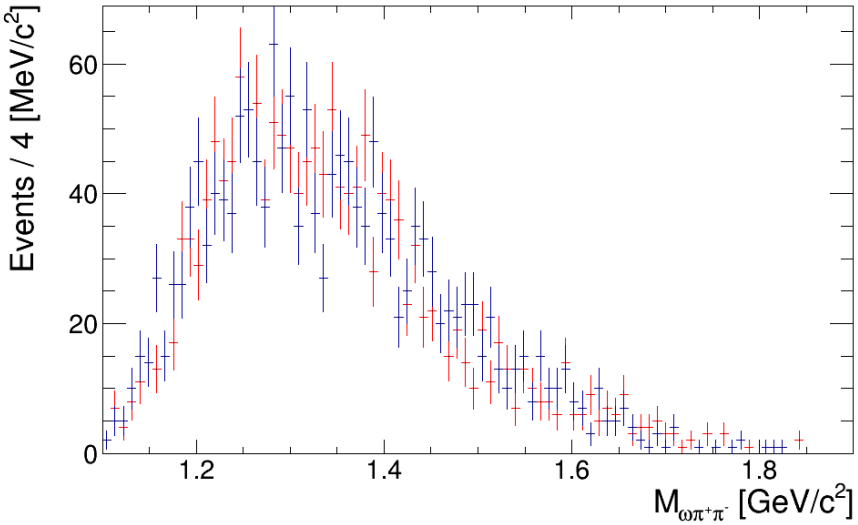

Figure 12.14 *Mass of misidentified $\omega\pi\pi$ from the high energy tail of $\eta\pi\pi$, from Monte Carlo of $\eta(1295)$. The signal region distribution is shown in red, sideband in blue. Results are near identical within errors, therefore any significant contribution from this channel should be removed through sideband subtraction.*

12.4 Searching for the $b_1(1235)$

From the resonant channels of interest, $\omega(1420)$, $\pi_1(1600)$, $\omega_3(1670)$ and $\pi_2(1670)$ can all decay to $b_1(1235)\pi$, which decays dominantly to $\omega\pi\pi$. Observing an enhancement around the mass of $b_1(1235)$ would be interesting on its own and also provide a indication of the four higher energy resonances mentioned at the beginning of this paragraph. To investigate this, the mass of a reconstructed $\omega\pi$ for both π^+ and π^- has been constructed.

There is strong agreement between the mass distributions of $\omega\pi^+$ for both methods of background subtraction, shown in Figure 12.15. However, there is greater disparity between the results for $\omega\pi^-$, with a relative bias towards a higher mass range in the sideband subtracted dataset, when compared to the sWeighted data. For both methods, the distribution of $\omega\pi^-$ has many more events in the $b_1(1235)$ mass range, providing greater potential for observing states decaying via this channel, as shown in Figure 12.16. The asymmetry in the distributions of $\omega\pi^+$ and $\omega\pi^-$ is primarily an acceptance effect as a result of the polarity of the magnetic field during g11a. In the configuration used, negatively charged pions would typically require a higher momentum, or a wider production angle, to be detected than positively charged pions. The reaction selection requiring

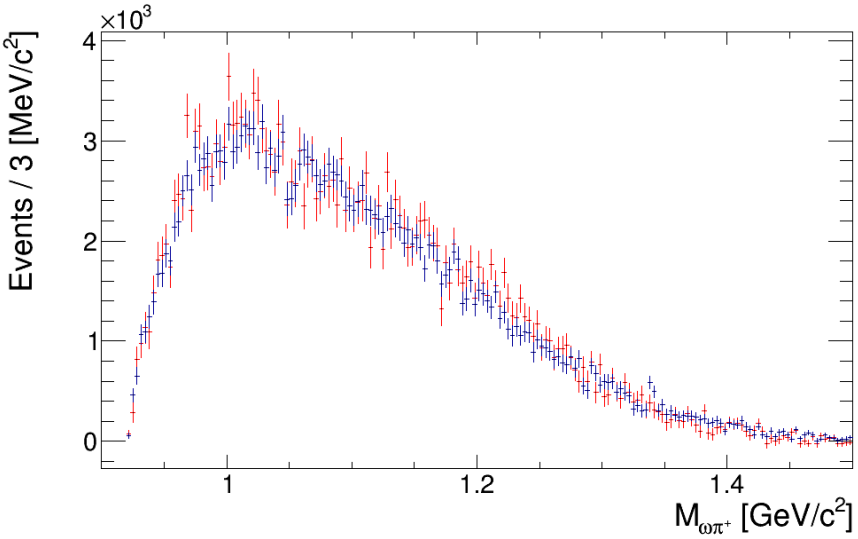

Figure 12.15 *Plots of $\omega\pi^+$ combinations of both Sideband Subtracted data (red), and sWeighted data (blue), looking for resonance contributions from the $b_1(1235)$. There is strong correlation between both the sWeighted and Sideband Subtracted datasets. Minimal structure is observed around the mass of the $b_1(1235)$*

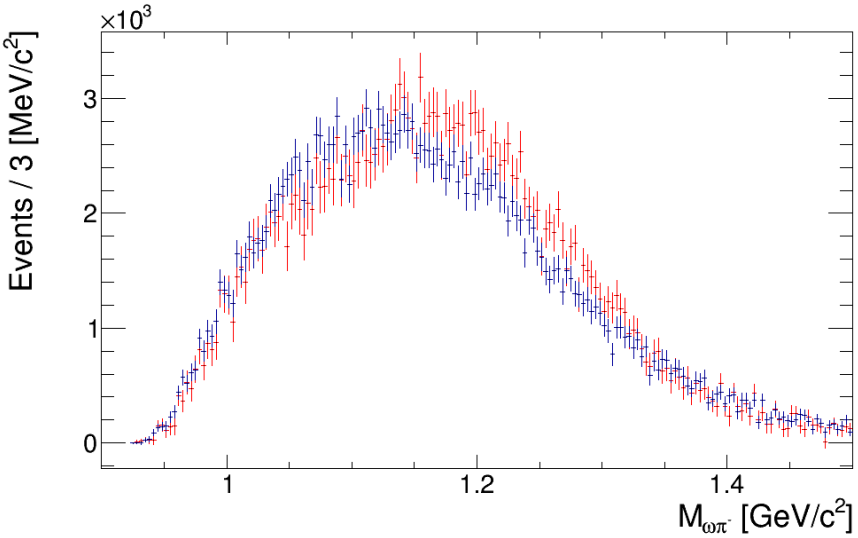

Figure 12.16 *Plots of $\omega\pi^-$ combinations looking for resonance contributions from the $b_1(1235)$. There is a much greater divergence between the two methods in comparison to Figure 12.15. The sWeighted data (red) trends above the Sideband Subtracted data (blue) between 1.00 and 1.15 GeV/c^2, and the reverse is true between 1.15 and 1.35 GeV/c^2. There is also significantly more data in the $b_1(1235)$ mass region for $\omega\pi^-$.*

the detection of only one π^+ and one π^- biased the distribution of detected π^- to higher momentums and wider production angles. In the energy range of this dataset, the $\omega\pi^-$ combinations are more likely to have enough energy allow the possibility of a decay from $b_1(1235)$. Therefore, this selection was chosen for assessing the significance of any contribution to the shape of the $\omega\pi\pi$ distribution.

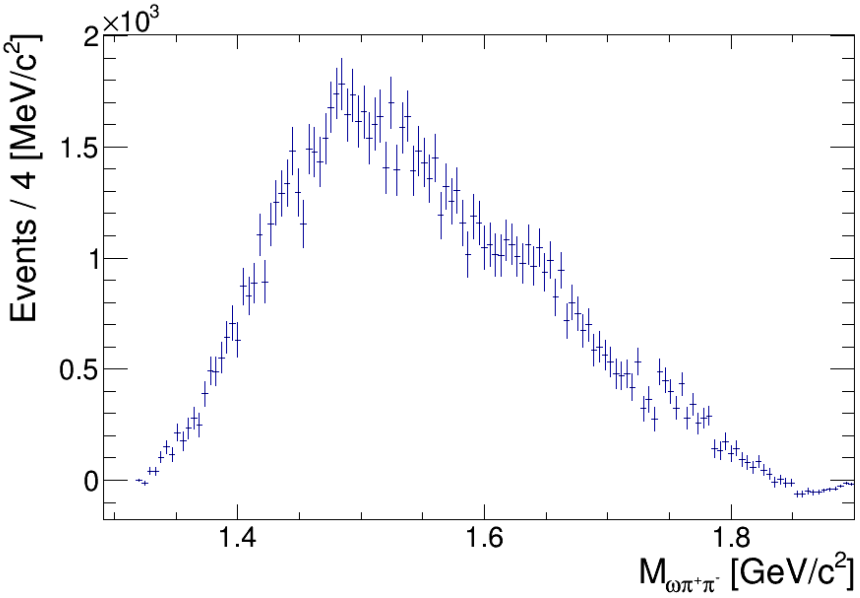

Figure 12.17 *The mass of $\omega\pi^-\pi^+$ with a selection cut around the $b_1(1235)$ mass in $\omega\pi^-$, 100 MeV/c^2 wide, looking to enhance resonances that decay via this channel. The selection significantly enhances the shoulder in the distribution around 1.65 GeV/c^2 in comparison Figure 12.7. This region corresponds to the mass range of $\pi_1(1600)$, $\omega_3(1670)$ and $\pi_2(1670)$, that can all decay via $b_1(1235)\pi$.*

In order to select $b_1(1235)$ events and enhance resonances that decay to this state in the $\omega\pi\pi$ spectra, a cut was placed around the mass and width of the $b_1(1235)$ in $\omega\pi^-$, 100 MeV/c^2 wide. The mass of $\omega\pi\pi$ for this selection was then plotted as shown in Figure 12.17. The kinematic range for this plot starts at the $b_1(1235)\pi$ threshold and extends up to higher energies. A significant structure is observed in the distribution between 1.62-1.68 GeV/c^2 where the distribution flattens, resulting in a shoulder in this energy range. A fit with a background polynomial and a gaussian to the enhancement shows a contribution centered around 1.65 GeV/c^2. This is very close to the centre of the mass range of $\pi_1(1600)$, $\omega_3(1670)$ and $\pi_2(1670)$, which all decay via $b_1(1235)\pi$; if they were present, we would expect such a shift in the distribution with these cuts. To determine which one of these, if any, is responsible for this structure would require a high level partial wave analysis to disentangle the magnitude of each contribution.

12.5 ρ cuts

As discussed in the introduction to this analysis, five mesons with masses around 1.65 GeV/c^2 are expected to decay via $\omega\pi\pi$ to the 5π final state analysed in this dataset. All of these are expected to be broad resonances typically 200-300 MeV/c^2 wide, but little is known about these decays, with significant uncertainty over their masses and cross sections. With each resonance being broad, with a similar mass, disentangling the decays from one another is challenging. However, only the $\pi_2(1670)$ decays via $\omega\rho \to \omega\pi\pi$ and a cut on $M(\pi\pi)$ around the mass of ρ can provide a selection to accentuate this decay mode.

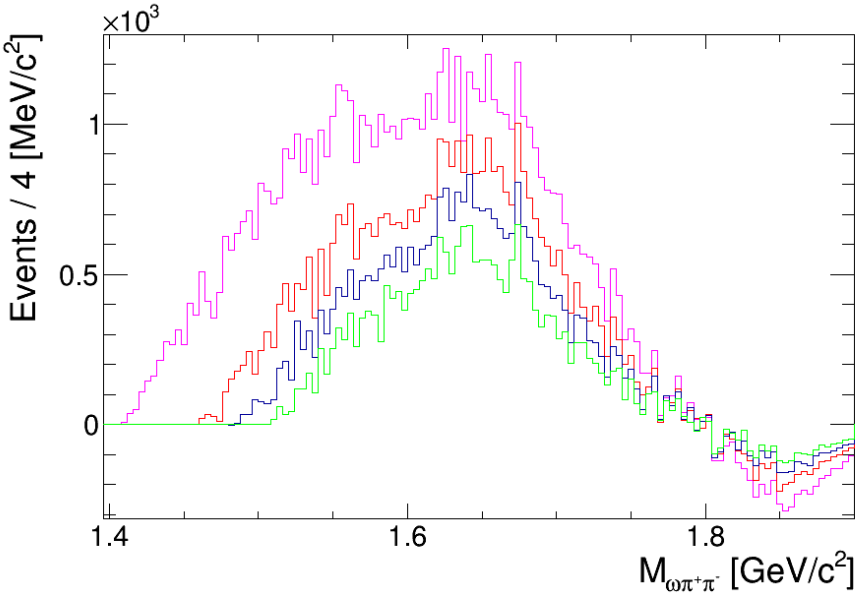

Figure 12.18 *Mass($\omega\pi\pi$) with a selection around the mass of ρ with varying widths in the combined detected $\pi\pi$. An enhancement is observed, centred around 1.68 GeV/c^2, with cuts close to the width of the ρ meson, 146.2 ± 0.7 [5]. 110 MeV/c^2 (green), 150 MeV/c^2 (blue), 200 MeV/c^2 (red), 300 MeV/c^2 (pink). Wider or narrower selections dilute this enhancement, indicating a contribution from decays via $\omega\rho$, a clear signal of the $\pi_2(1670)$ meson.*

The mass of $\omega\pi\pi$ with a cut on $M(\pi\pi)$ around the mass of ρ with varying widths is shown in Figure 12.18. If the $\pi_2(1670)$ resonance is present, cuts closer to the width of ρ, around 150 MeV/c^2, should produce an enhancement in the $\omega\pi\pi$ spectra around 1670 MeV/c^2. Cuts narrower or wider than this should reduce the significance of this, by diluting the relative significance of $\pi_2(1670)$ events. The cuts of width 150 and 200 MeV/c^2 peak at around 1.65 GeV/c^2 with a clearer enhancement around this mass than the wider or narrower cuts. This provides

an indication of the presence of the $\pi_2(1670)$ events in the spectrum.

It should be noted that at higher energies, nearer the limit of the phase space, there is a tendency for sideband subtraction to over subtract the signal region due to the increased phase space available to the upper sideband. Also at this point, statistics are more limited and the phase space of the spectrum will be cut off due to energy conservation considerations. If there was a broad resonance peaked around 1.65 GeV/c^2, the shoulder of this at higher energies would be diminished simply due to limitations in the available energy. Repeating this analysis with access to a dataset encompassing reactions at higher energies, such as those available in CLAS12, would allow access to these regions without these phase space limitations.

12.6 Detector Acceptance

A further study was carried out on 10 million phase space $\gamma p \rightarrow \omega\pi\pi p$ Monte Carlo events, in order to better understand the origins of any structure in the dataset. The generated ω peak is narrow, with a width ~ 8 MeV/c^2, significantly lower than the ~ 20 MeV/c^2 resolution of CLAS. After reconstruction, selecting only the $\gamma p \rightarrow (\omega)\pi\pi p$ events, the signal peak broadened significantly. The ratio of events in the region considered 'signal (for sideband subtraction) to those in the sidebands also reduces significantly. Adjusting for region width, before reconstruction the ratio is $\sim 21:1$ signal to sideband. After reconstruction it is just over 2:1. These changes are a consequence of factors such as CLAS resolution, the selection of pions which decayed from the ω instead of the spectator pions, and beam spreading, where events that originated in one energy bin end up being resolved in another. The effect of these changes to the distribution are more clearly seen in Figure 12.19. This show the distribution of the Monte Carlo data and the reconstructed events for the mass of ω against the mass of $\omega\pi\pi$.

This analysis is focused on the distribution of the mass of $\omega\pi\pi$; in order to better understand this, the acceptance of the detector system also needs to be considered. Figure 12.20 [Upper] shows the $\omega\pi\pi$ mass distribution present in the Monte Carlo for the left and right sideband regions. Slightly more events are observed in the right sideband, and the distributions follow a similar trend, with limited differences observed, apart from at the low mass region in the right sideband, where kinematics restricts events.

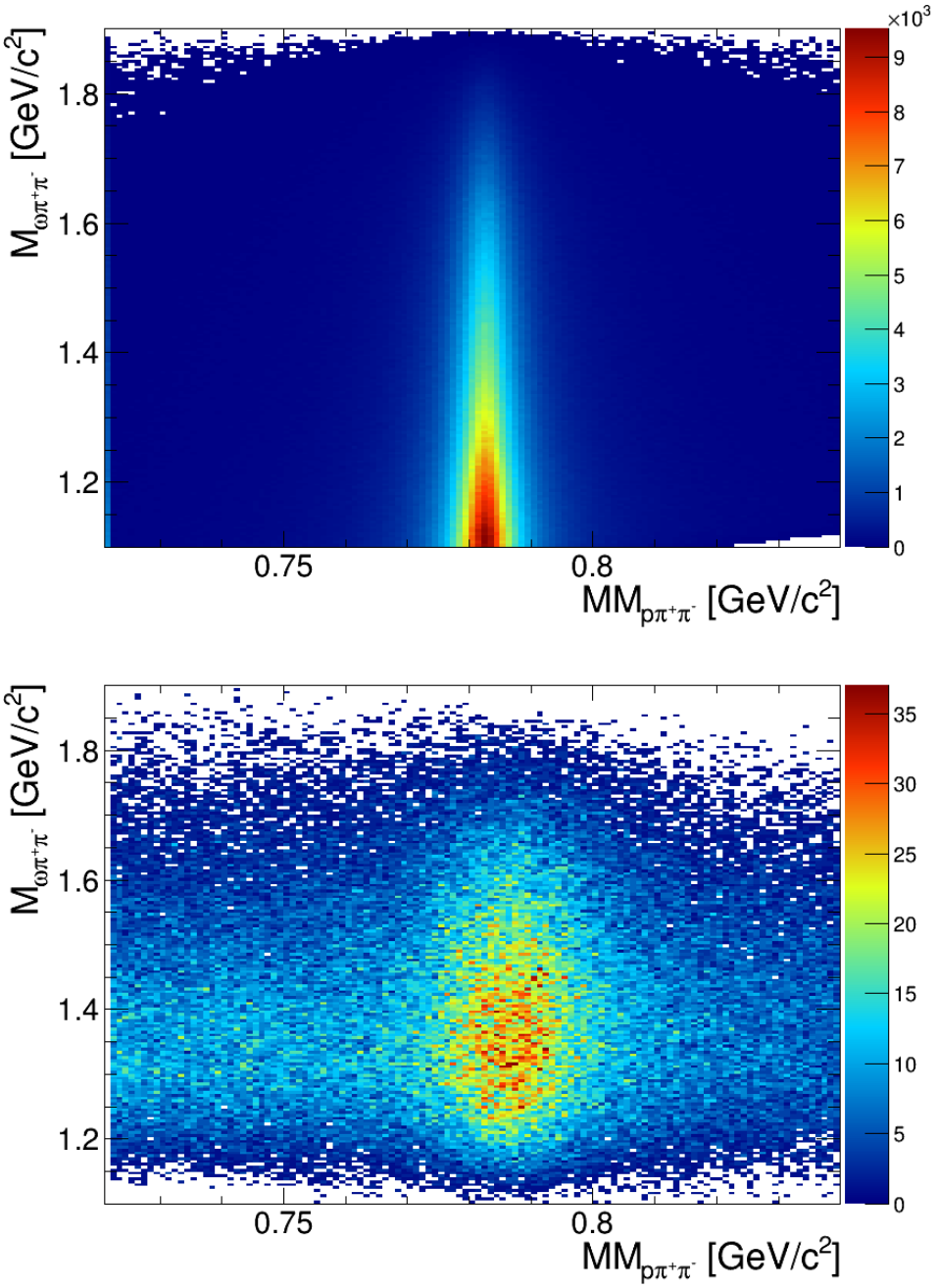

Figure 12.19 *Missing Mass($p\pi\pi$) vs Mass($\omega\pi\pi$) for generated Monte Carlo [Upper] and the reconstructed Monte Carlo data [Lower] after passing through CLAS. The generated data shows a narrow ω peak as would be expected. The reconstructed data shows significant broadening of the ω peak range, along with significant background away from the peak from misidentified final state pions. In addition, the figure demonstrates low acceptance for low momentum pions, with the mass of the reconstructed $\omega\pi\pi$ peaking around 1.35 GeV/c^2 in Mass($\omega\pi\pi$) compared to 1.1 GeV/c^2 for the generated data.*

Figure 12.20 [Lower] shows the $\omega\pi\pi$ distribution for the reconstructed Monte Carlo data. Both the reconstructed distributions show significantly reduced acceptance in the lower mass range. The reconstructed mass distributions peak between 1.3 and 1.4 GeV/c^2, whereas the original datasets peak at the low energy 1.1-1.2 GeV/c^2 range, which is a minimum for the reconstructed data. Low momentum pions may struggle to be reconstructed by CLAS if they fail to pass through the drift chambers, Cherenkov and ToF systems. They can also be more likely to miss the detector system entirely (e.g. low momentum π^-s are likely to be bent towards the beamline because of the polarity of the magnetic field during the run).

Also significant is that the relative number of events in each sideband has shifted, with more events in the left sideband after reconstruction; the reverse was true in the Monte Carlo generated events. A study on the pre and post reconstruction values of $\omega\pi\pi$ indicated that a significant fraction of this effect is due to beam migration, with a greater number of events bleeding into the left sideband from the signal region than to the right. This effect is greatly amplified in a Monte Carlo study that includes only $\omega\pi\pi$ events, rather than the full range of processes present in a real dataset.

Finally, and potentially significant for the structure of the $\omega\pi\pi$ distributions (see Section 12.1), there is a significant structure observed in the reconstructed left sideband dataset just above 1.3 GeV/c^2, which is not prominent in either the right sideband or signal region of the dataset and is not observed in the un-reconstructed data. For comparison, the signal region before and after reconstruction in shown in Figure 12.21. The statistics are not large, but this indicates an asymmetry in the left sideband region, due to an acceptance effect that could significantly alter the region of interest close to the expected mass of the $a_2(1320)$.

To see whether potential acceptance effects are also significant in the real dataset, the same distributions of data need to be studied. Figure 12.22 [Upper] shows the distribution of the experimental data across the signal and sideband regions against the the mass of $\omega\pi\pi$. The ω signal peak is clearly visible at the centre of the distribution. Figure 12.22 [Lower] shows a projection of this figure onto the mass of $\omega\pi\pi$ for the signal region of the dataset. This can be seen to follow a pattern close to a normal distribution, but with a slight kink in the distribution observed just below 1.3 GeV/c^2. Figure 12.23 [Upper] shows the same projection, but for the left sideband region. This distribution follows a similar trend, but

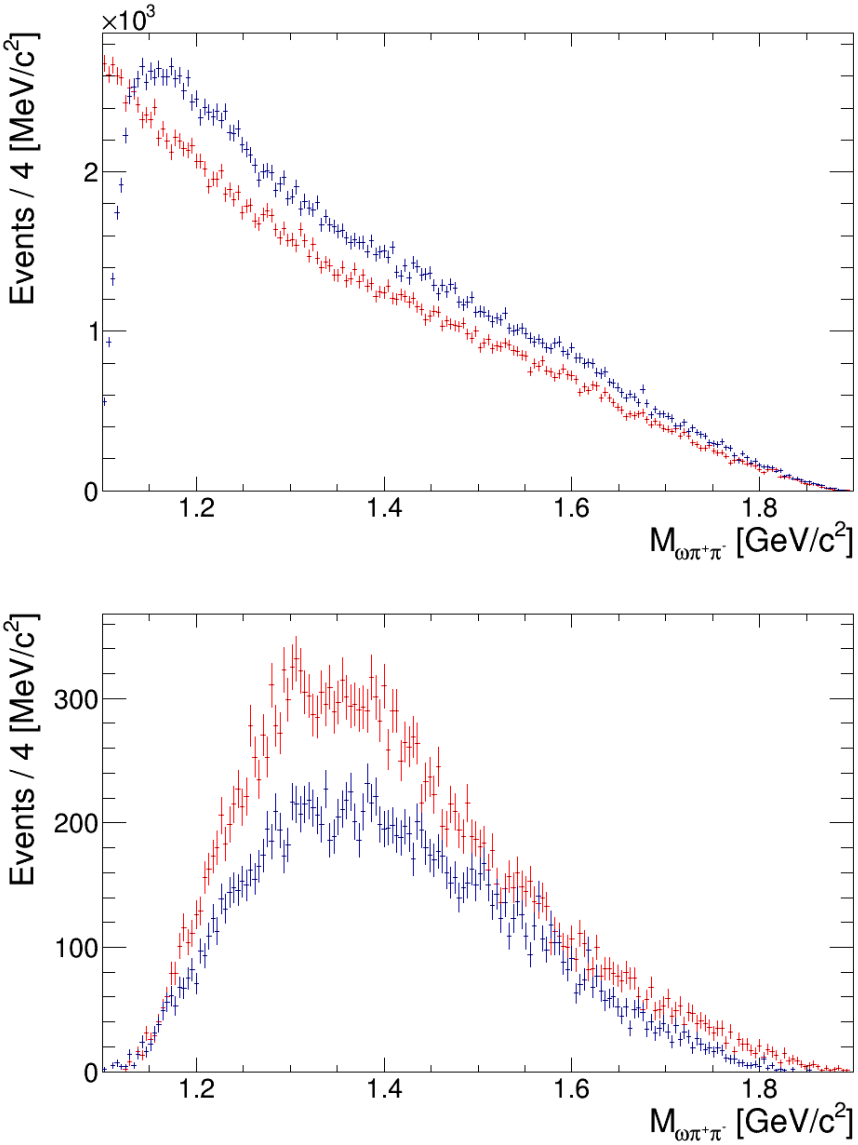

Figure 12.20 *Mass($\omega\pi\pi$) for the generated Monte Carlo data [Upper] and the reconstructed dataset [Lower], present in the left and right sideband regions. Comparing the two plots, very few of the low energy particles, 1.1-1.3 GeV/c^2 in the generated data are reconstructed by CLAS. The generated datasets show more events present in the right sideband (blue) compared to the left (red). After reconstruction, the situation has reversed and significantly more events are found in the left sideband, in comparison to the right. A significant fraction of this effect is due to beam migration with more events, originally present in the signal region, 'bleeding' into the left sideband than the right.*

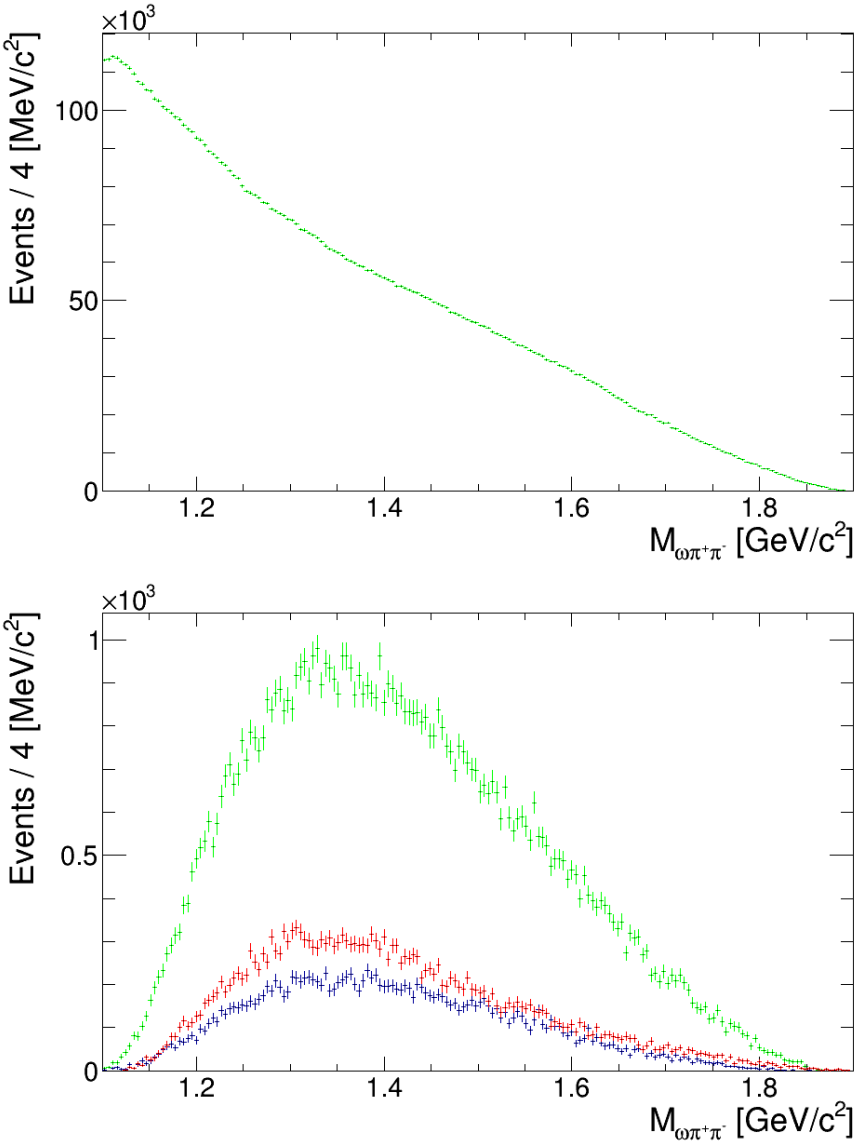

Figure 12.21 *Mass($\omega\pi\pi$) for the generated Monte Carlo data present in the signal region [Upper] and the reconstructed dataset for the signal and both sidebands [Lower]. In the lower plot a significant structure is observed in the left sideband (red) just above 1.3 GeV/c^2, which is not seen in the signal (green) or right (blue) sideband regions of the dataset. This indicates an asymmetry in the acceptance of the detector, close to the region of interest for the $a_2(1320)$ meson.*

there is a much more abrupt kink just above 1.3 GeV/c^2; this is in the same mass range as that in which the structure was observed in Figure 12.20 [Lower] for the reconstructed Monte Carlo dataset. The projection for the right sideband is shown in Figure 12.23 [Lower]. Again this follows a similar but more continuous distribution, without such obvious structure.

The structures observed in Figure 12.20 [Lower] and 12.23 [Upper] may indicate that there is an acceptance effect occurring in the left sideband, which would cause an over-subtraction from the distribution of $\omega\pi\pi$, in the region just above 1.3 GeV/c^2. This artefact may account for the larger 'dip' observed in the sideband subtracted distribution shown in Figure 12.10 in the same mass range. This is the mass range in which there was significant disagreement between the two methods of background subtraction. If this is due to acceptance, then the method of sWeighting has been less strongly affected by the artefact, and the results from it can be interpreted with greater confidence.

In order to resolve this uncertainty, the next step is to apply a full acceptance correction to the dataset. This would need to be done using Monte Carlo simulation with very high statistics, making sure that the dataset was represented properly, binning in variables such as t and beam energy. However, the 10 million events that are currently available are just a small fraction of the events necessary to undertake such a correction, without introducing large statistical uncertainties. I estimate that I would need at least a 100 fold increase in statistics to be able to apply a reliable acceptance correction to the data. These simulations will take more than a month to complete with available computational power. The simulations have been initiated, and I will correct the results before publication, but within the time limits available to this thesis the results will have to remain in their current state.

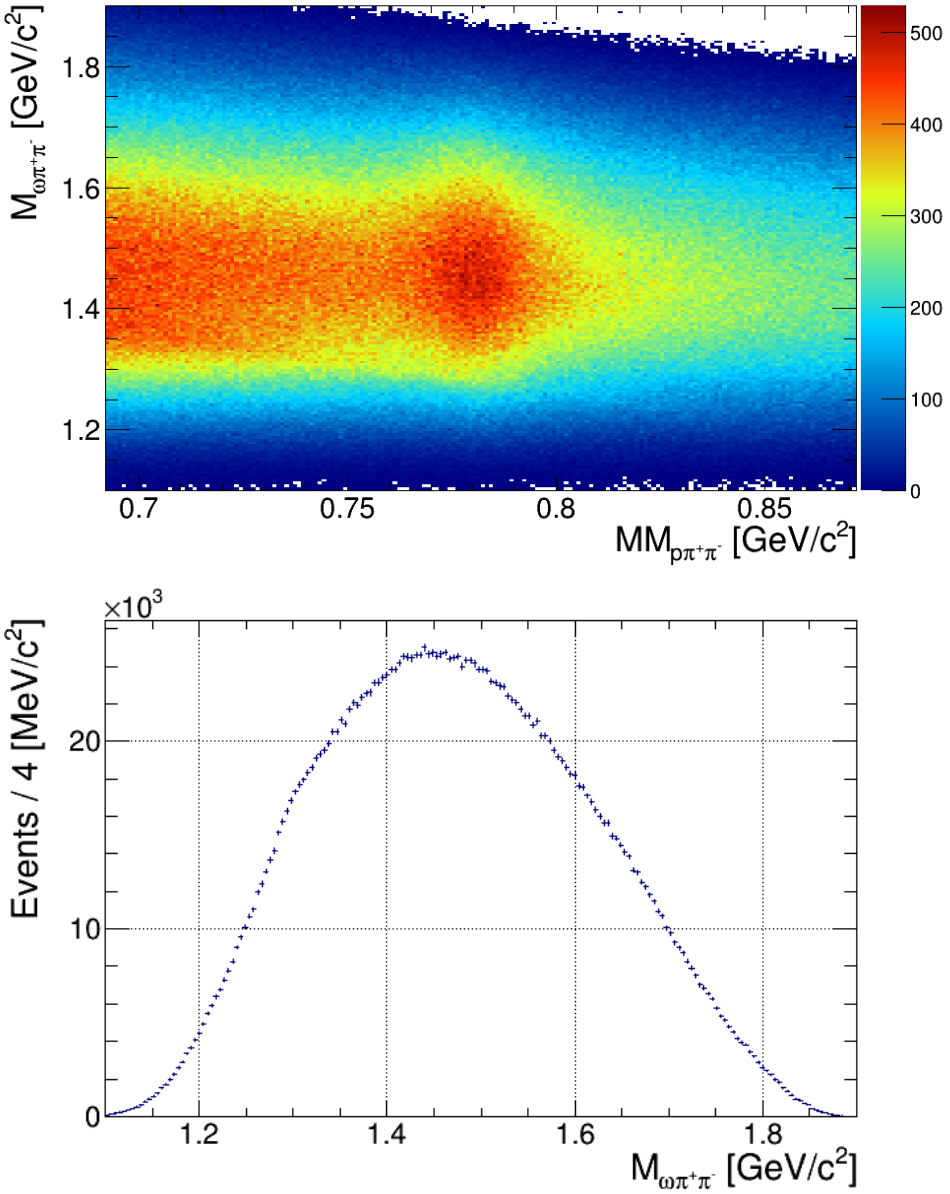

Figure 12.22 *Missing Mass($p\pi\pi$) vs mass($\omega\pi\pi$) for the experimental dataset [Upper] and a projection of the signal region onto the y-axis between 0.752 and 0.812 GeV/c^2 [Lower]. In the upper plot a clear peak is observed about the mass of the ω meson, along with a band of background stretching across the range covered on the x-axis. The projection of the signal region onto the y-axis, shows a close to normal distribution with a limited 'kink' in the dataset around 1.3 GeV/c^2.*

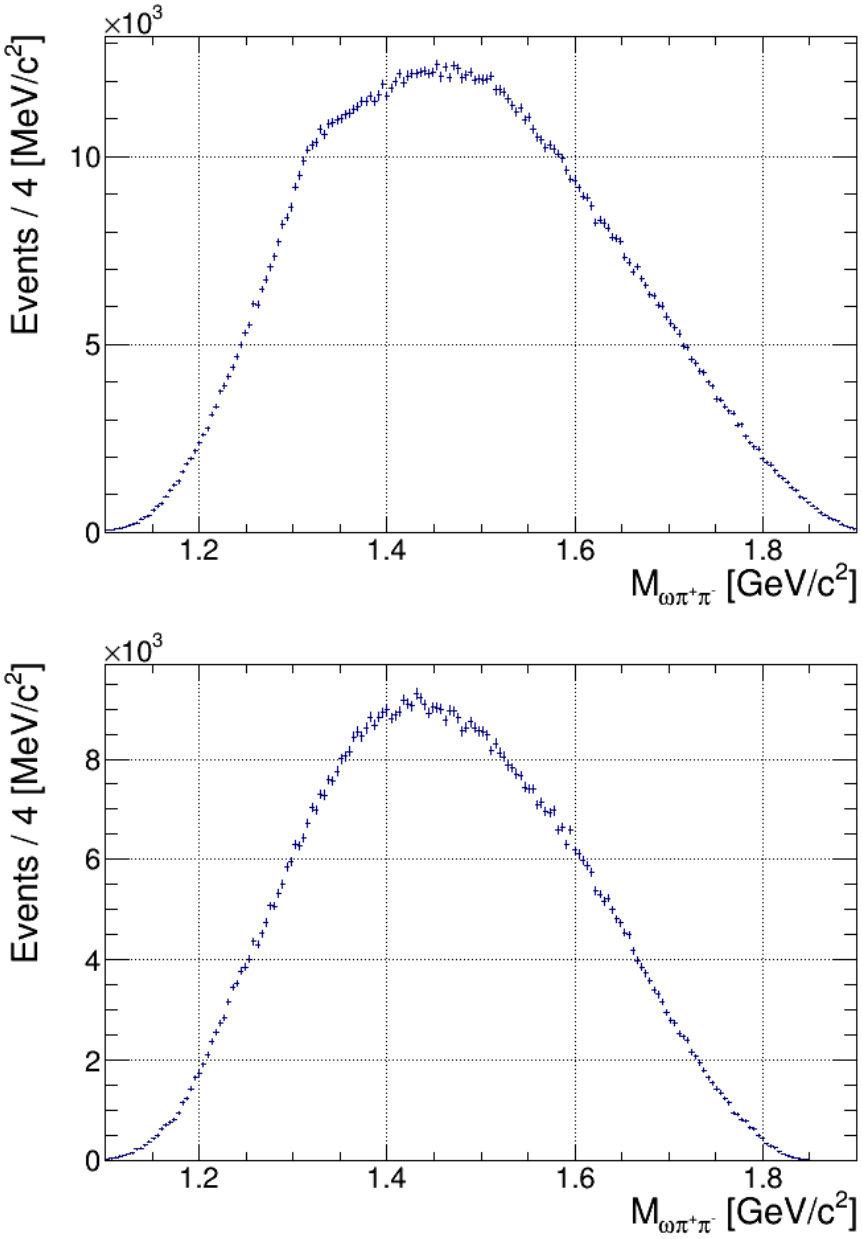

Figure 12.23 *[Upper] A projection onto the y-axis of the left sideband between 0.722 and 0.752 GeV/c^2 in Figure 12.22 [Upper] and also the corresponding right sideband between 0.812 and 0.842 GeV/c^2 [Lower]. A pronouced 'kink' is observed around 1.3 GeV/c^2 in the left sideband projection [Upper] with none in the right sideband [Lower] at the same energy.*

12.7 Van Hove Plots

Van Hove Plots or, as they are also known, Longitudinal Phase Space (LPS) Plots, separate reactions based on the kinematics of the particles involved. The technique separates reactions into sectors, based on whether each individual particle is travelling forwards or backwards in the frame of reference of the reaction. For $\omega\pi\pi p$ this results in 14 possible sectors, with different combinations of particles propagating either forward or backwards in the reaction frame.

Sector	Forward	Backward
0	$\omega\pi^+\pi^-$	p
1	$\omega\pi^+p$	π^-
2	$\omega\pi^-p$	π^+
3	$\pi^+\pi^-p$	ω
4	$\omega\pi^+$	π^-p
5	$\omega\pi^-$	π^+p
6	ωp	$\pi^+\pi^-$
7	$\pi^+\pi^-$	ωp
8	π^+p	$\omega\pi^-$
9	π^-p	$\omega\pi^+$
10	ω	$\pi^+\pi^-p$
11	π^+	$\omega\pi^-p$
12	π^-	$\omega\pi^+p$
13	p	$\omega\pi^+\pi^-$

Table 12.1 *The combinations of particles propagating forward and backward in the centre of mass frame of the $\omega\pi^+\pi^-p$ final state. This defines the numbering of the LPS sectors used in this analysis.*

This technique attempts to isolate reactions that favour certain kinematics over others. For example, it may separate s-channel N* resonances from more t-channel favoured meson resonances. In the case of $\gamma p \to \omega\pi\pi p$, it may be possible to enhance resonant contributions, by selecting in sectors where the three mesons are travelling in the same direction and the proton is travelling away from them, as would be the case in a $\gamma p \to a_2(1320)p$ reaction. Sectors where two mesons are travelling in the same direction may also show enhancements, as limits of the resolution and reconstruction of the detector leads to some bleeding between sectors.

The improved selection comes at the cost of statistics, particularly for reactions with a greater number of final state particles. For a 3 particles final state, such

as $\gamma p \to \pi\pi$, there are only 6 combinations. For a 4 particle final state, such as $\gamma p \to \omega\pi\pi p$, this rises to 14. If we were to consider a $5\pi p$ system or even the $4\pi p 2\gamma$, the final state of $\omega\pi\pi p$, the number of sectors would be 62 and 126 respectively. Splitting the data up into so many sectors greatly limits the statistics of each one, particularly as the split is not uniform and depends on the kinematics of the reaction. To illustrate this, the sector split for $\gamma p \to \omega\pi\pi p$ from the g11a dataset is shown in Figure 12.24. The kinematics of the different sectors for the $\omega\pi\pi p$ final state are shown in Table 12.1.

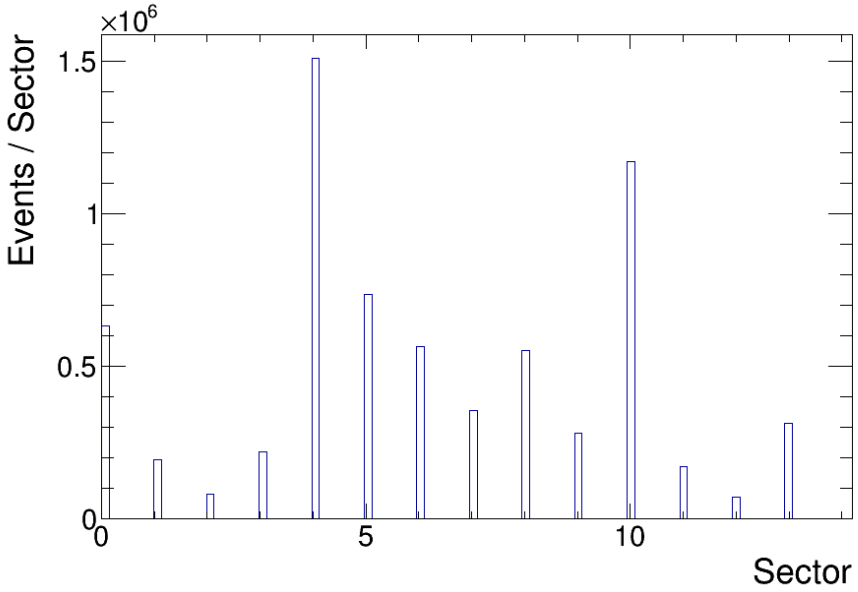

Figure 12.24 *The split of events into the different LPS sectors in the $\omega\pi^+\pi^- p$ final state. The sectors are defined in Table 12.1. Not all reaction kinematics are equally likely to be detected, with some combinations containing more than 30 times more events than others.*

Utilising Van Hove plots, when the particles used to determine sectors are not the detected final state particles(e.g ω), relies on accurate reconstruction of the intermediate states. In addition, when not all final state particles are detected, reconstruction can lead to misidentified background slipping into sectors. As a final layer of complexity, in the reaction studied $\gamma p \to (\omega)\pi\pi p$, where $\omega \to \pi^+\pi^-\pi^0$ there is an additional problem of multiple combinations of final state pions, making it difficult to select only those that decayed from an ω. Inevitably, some combinatorial background enters the system, leading to some results being allocated to the wrong sector. Despite all these issues, the technique has potential to extract resonant contributions based on the variation in kinematics of reactions.

For this study, only sWeighted datasets were used because the event by event

background subtraction greatly reduced the complexity of creating longitudinal phase space plots. An example of a set of longitudinal sectors is shown in Figure 12.26, in this case for values of $\omega\pi\pi$ against $\omega\pi^-$. Structure in the appropriate sectors in this dataset could indicate signs of resonant states decaying via $b_1(1235)\pi$ to $\omega\pi\pi$. Sector 0, where all 3 mesons are travelling forward, is the most likely sector to enhance this type of resonant contribution; mass distributions for $\omega\pi\pi$ and $\omega\pi^-$ are shown in Figures 12.25 and 12.27 respectively.

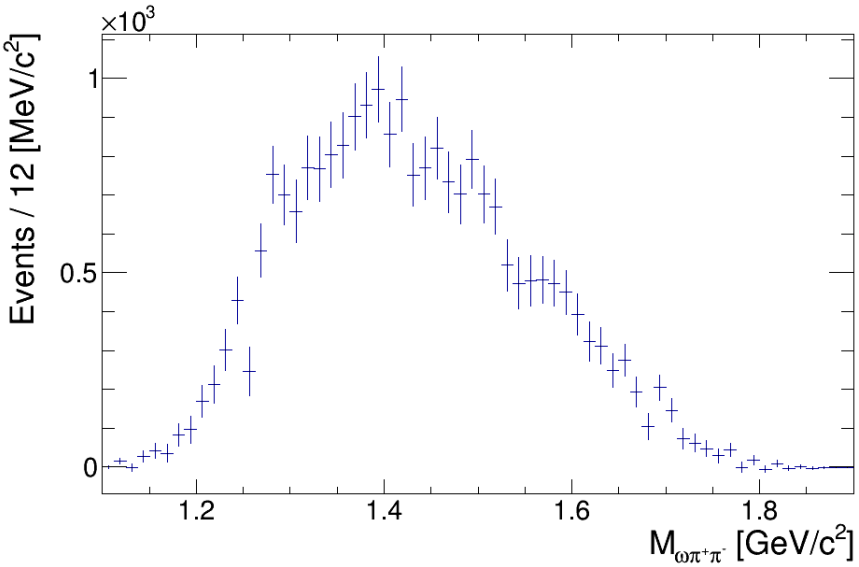

Figure 12.25 *LPS mass of $\omega\pi\pi$. Sector 0 with 3 mesons travelling forward and the proton travelling backwards. There is interesting structure present in this sector with a sharp rise observed at 1.25-1.3 GeV/c^2 and two shoulders visible around 1.5 and 1.6 GeV/c^2. The structures may be due to resonances or may simply be statistical fluctuations. Greater statistics are required to make a more definite conclusion.*

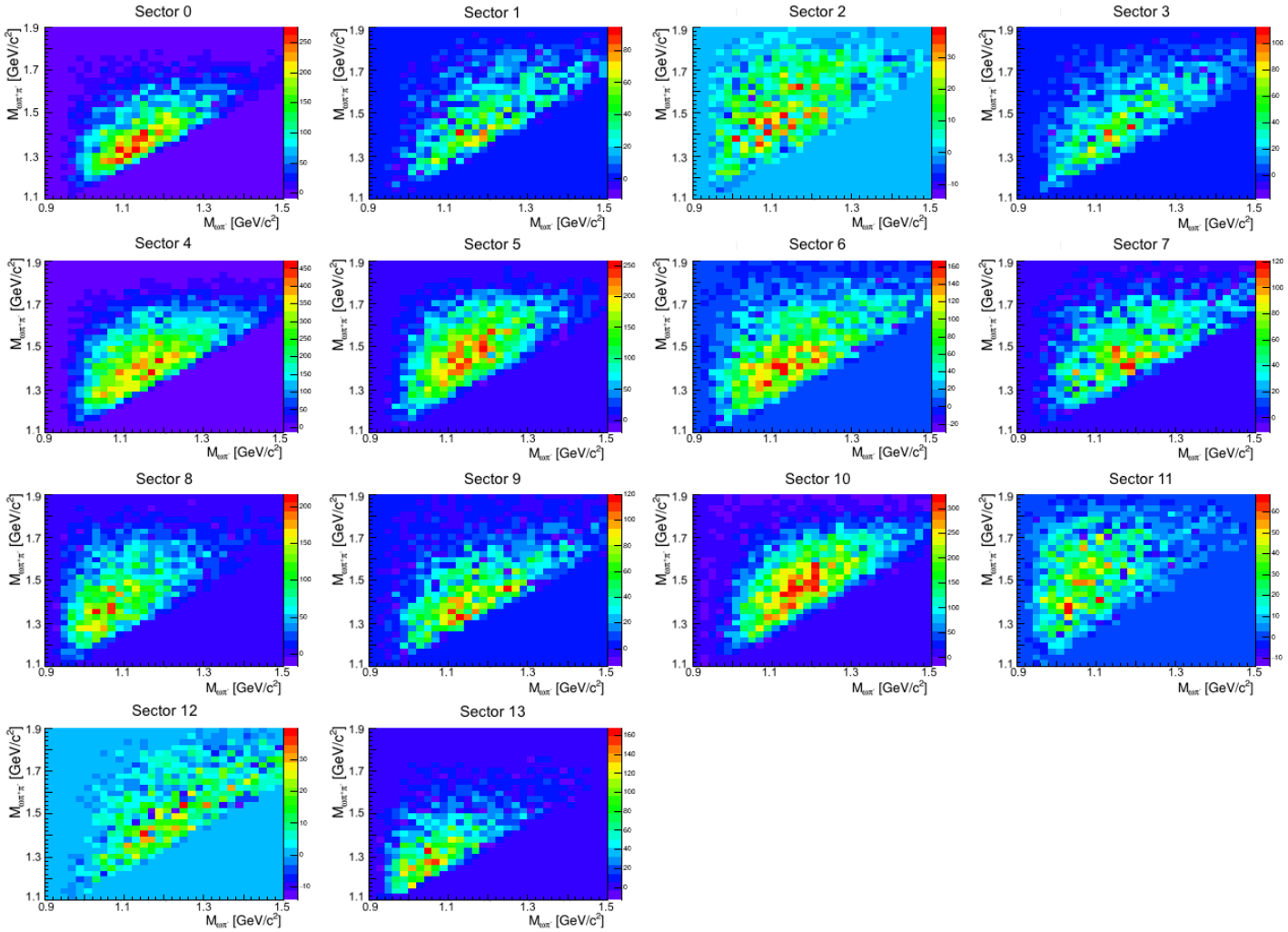

Figure 12.26 *An example of the differing structure of LPS bins for the decay to $\omega\pi^+\pi^-p$. The figures show mass of $\omega\pi^-$ vs the mass of $\omega\pi\pi$ for all 14 sectors of the final state, listed in Table 12.1 (All masses measured in GeV/c^2). Splitting events into these kinematic ranges helps to isolate the contribution of different reaction processes.*

Figure 12.25 has several interesting structures in its distribution, with a sharp rise observed at 1.25-1.3 GeV/c^2 and two shoulders visible around 1.5 and 1.6 GeV/c^2. In Figure 12.27, there is a peak observed just above 1.2 GeV/c^2, in the correct region for a $b_1(1235)$. Unfortunately, sector 0 includes only a relatively small fraction of the dataset, $\sim 7\%$, less than half the statistics available to sectors 4 and 10. This makes drawing further conclusions about any structure difficult, as statistical fluctuations become very significant. When considering analysis of this channel in CLAS12, this technique shows great promise; with the increased energy and luminosity available, the statistical limitations of the approach can be overcome.

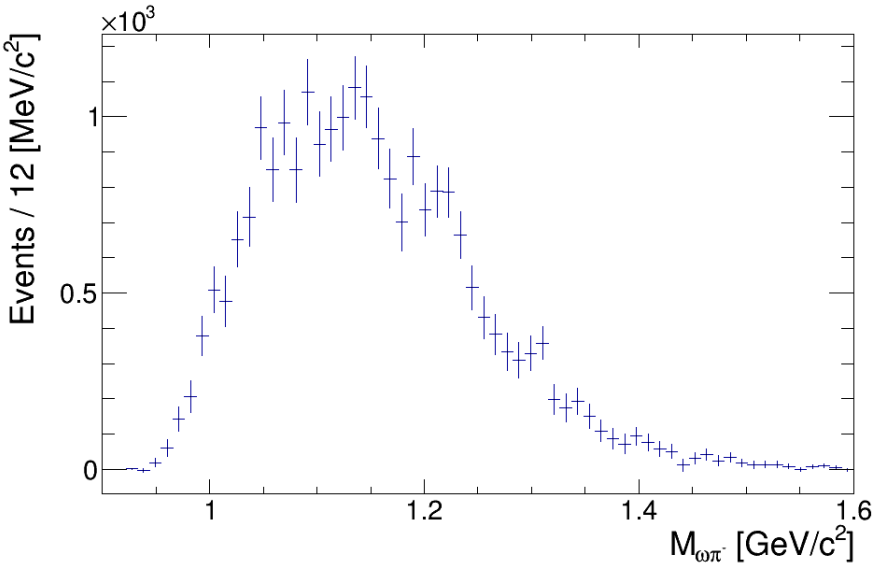

Figure 12.27 *LPS mass of $\omega\pi^-$ sector 0 with 3 mesons travelling forward and the proton travelling backwards. An enhancement is observed just above 1.2 GeV/c^2 in the correct region for a $b_1(1235)$ meson. However, the uncertainty in the value of the points is significant and further data is required to determine the significance of the structure.*

12.8 Summary

The results of a first analysis of the $\gamma p \rightarrow \omega\pi\pi p$ decay channel are covered in this chapter. The focus of this has been resonances decaying to $\omega\pi\pi$ in the energy range available to the g11a dataset. The results show evidence for structure around the mass of $a_2(1320)$, with both sideband subtraction and the sPlot methods. Although there is some disagreement between the methods in

this region, these may be partly due to a detector acceptance effect. There is also evidence for decays via the $b_1(1235)\pi$, with a significant enhancement observed in the mass of $\omega\pi\pi$ at around 1650 MeV/c^2, close to the mass of 3 broad resonances in this channel, $\pi_1(1600)$, $\omega_3(1670)$ and $\pi_2(1670)$. An enhancement is also observed at the mass of the $\pi_2(1670)$ with a selection on the $\omega\rho$ decay mode of this resonance. Finally a study on using Longitudinal Phase Space Plots has been conducted, in order to separate the different kinematic contributions to the reaction. However, the statistics available at CLAS6 energies limit the significance of the results obtained; in CLAS12 this should no longer be a problem. A full acceptance correction to the dataset is being prepared before any results are published. This will allow cross sections for the reaction to be determined and ready the dataset for a full partial wave analysis.

A summary of the resonant states which are thought to decay to $\omega\pi\pi$ in the energy range of the dataset, Table 9.2, are shown in Figure 12.28, placed under the sWeighted mass of $\omega\pi\pi$ from the dataset. The resonances are normalised to have the same integrated area, therefore the narrower resonances are shown with higher peaks.

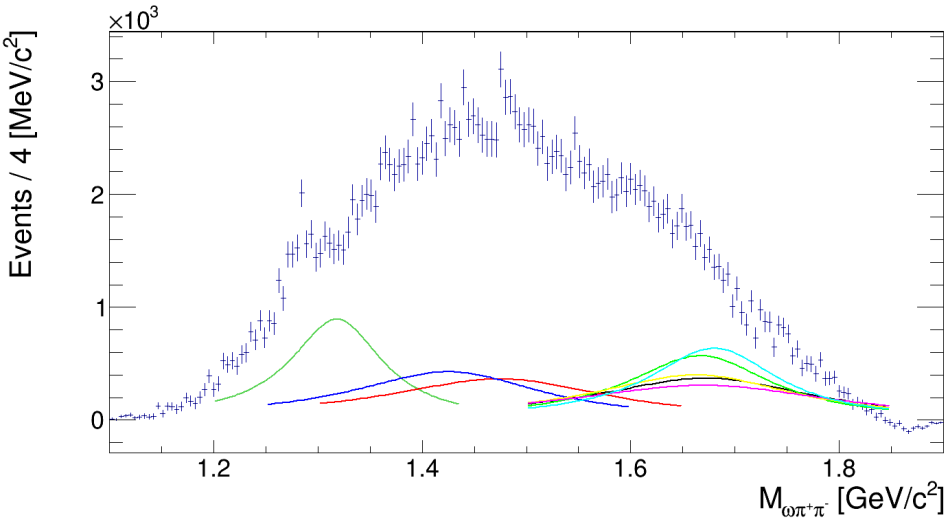

Figure 12.28 *Projections of $\omega\pi\pi$ resonances predicted to exist in the mass range listed in Table 9.2. Each is normalised to the same integrated area, for a Breit-Wigner distribution covering the literature width of the resonance. Resonances with narrower widths will produce higher peaks by this method. To be clear, these are not extracted from the dataset, but are meant to highlight the regions of interest for possible resonant contributions to the dataset. Meson resonances with colours: $a_2(1320)$ (dark green), $\omega(1420)$ (blue), $a_0(1450)$ (red), $\pi_1(1600)$ (yellow), $\omega(1650)$ (pink), $\omega_3(1670)$ (bright green), $\pi_2(1670)$ (black), $\Phi(1680)$ (teal).*

Chapter 13

Conclusions

The design, development and construction of a new Forward Tagging Hodoscope which will be installed as part of the 12 GeV upgrade to CLAS at Jefferson Lab has been presented. The detector is designed to differentiate between photons and electrons with sub nanosecond timing resolution and forms an integral part of the new forward tagger system for photoproduction experiments in CLAS12. This system opens up a whole new research programme in CLAS12 using a tagged and polarised almost real photon beam.

The Hodoscope is based around a segmented array of plastic scintillator tiles, connected to wavelength shifting fibres, which transport signals away to be read out by silicon photomultipliers. To achieve the necessary level of timing resolution for its role in photon tagging in CLAS12, simulations estimated an output of 55 photons per event were required. Currently, the Forward Tagger is producing an average of over 100 photons per event, with further optimisation of the detector still to be completed.

Hardware development of the detector is complete, with all channels in the detector performing above design requirements. Software work developing the controls to operate the detector for tagging and analysis is still ongoing. The Hodoscope, along with the calorimeter and tracker elements of the Forward Tagger, will be installed into Hall B at Jefferson lab in July 2017, with the first test beamtime scheduled for September 2017. Full commissioning and optimisation of the detector can then begin, ready for experimental runs starting in 2018. The new system will be critical for future experiments in CLAS12, searching for exotic hadronic states such as hybrid mesons or tetraquarks, and a range of other

hadron spectroscopy programmes.

Also presented is the first measurement of the $\gamma p \to \omega\pi\pi p$ decay channel, using data from the g11a run at CLAS with energies up to 5 GeV. The ω predominantly decays to $\pi^+\pi^-\pi^0$ before reaching the detector, resulting in a 6 particle final state with multiple π^+ and π^-. The ω needs to be reconstructed from its decay pions; however, because of the complexity of the final state, there is inherent combinatorial background. To help manage the background in the channel, the analysis utilised two different methods of background subtraction, sideband and sPlot, to provide complementary results, with further information on their significance.

The results of the analysis have primarily focused on evidence of resonances that decay to $\omega\pi\pi$, either directly or via $b_1(1235)\pi$. Clear evidence is found for structure in the distribution of the reconstructed mass of $\omega\pi\pi$ around the mass of the $a_2(1320)$ (with both sideband subtraction and the sPlot method). Significant structure is also observed for decays via the $b_1(1235)$ at around 1.65 GeV/c^2, just below the expected mass of the $\pi_1(1600)$, $\omega_3(1670)$ and $\pi_2(1670)$. Finally, evidence is also presented for an enhancement due to $\pi_2(1670)$ decaying via $\omega\rho$.

The first study of $\omega\pi\pi$ from photoproduction suggests $\omega\pi\pi$ may be a very useful channel for meson spectroscopy. Indications of excited meson states are already evident in simple analysis. To follow on from this analysis a partial wave analysis of acceptance corrected data is necessary. I am planning to complete this full acceptance correction to the dataset in the coming months. It would then be ready for a full partial wave analysis, to extract the contribution of different resonances decaying to $\omega\pi\pi$.

Bibliography

[1] M. Gell-Mann, "A schematic model of baryons and mesons," *Physics Letters*, vol. 8, no. 3, pp. 214–215, 1964.

[2] G. Zweig, "An su (3) model for strong interaction symmetry and its breaking. version 1," *Developments in the Quark Theory of Hadrons*, 1964.

[3] E. D. Bloom, D. Coward, H. DeStaebler, J. Drees, G. Miller, L. W. Mo, R. E. Taylor, M. Breidenbach, J. I. Friedman, G. C. Hartmann, *et al.*, "High-energy inelastic e- p scattering at 6 and 10," *Physical Review Letters*, vol. 23, no. 16, p. 930, 1969.

[4] M. Breidenbach, J. I. Friedman, H. W. Kendall, E. D. Bloom, D. Coward, H. DeStaebler, J. Drees, L. W. Mo, and R. E. Taylor, "Observed behavior of highly inelastic electron-proton scattering," *Physical Review Letters*, vol. 23, no. 16, p. 935, 1969.

[5] C. Patrignani, P. D. Group, *et al.*, "Review of particle physics," *Chinese physics C*, vol. 40, no. 10, p. 100001, 2016.

[6] D. Griffiths, *Introduction to Elementary Particles*. John Wiley & Sons, Inc, 1987.

[7] G. Bali, K. Schilling, A. Hulsebos, A. Irving, C. Michael, P. Stephenson, U. Collaboration, *et al.*, "A comprehensive lattice study of su (3) glueballs," *Physics Letters B*, vol. 309, no. 3, pp. 378–384, 1993.

[8] B. R. Martin and G. Shaw, *Particle physics*. John Wiley & Sons, 2016.

[9] B. Lab, "Quark confinement." `http://particleadventure.org/quark_confinement.html`. Accessed: 17/05/2017.

[10] D. J. Gross and F. Wilczek, "Ultraviolet behavior of non-abelian gauge theories," *Physical Review Letters*, vol. 30, no. 26, p. 1343, 1973.

[11] H. D. Politzer, "Reliable perturbative results for strong interactions?," *Physical Review Letters*, vol. 30, no. 26, p. 1346, 1973.

[12] S. Bethke, "Experimental tests of asymptotic freedom," *Progress in Particle and Nuclear Physics*, vol. 58, no. 2, pp. 351–386, 2007.

[13] N. Bohr, "On the constitution of atoms and molecules," in *Niels Bohr, 1913-2013*, pp. 13–33, Springer, 2016.

[14] Venny85, "Baryon octet." `https://en.wikipedia.org/wiki/File:Baryon_octet_w_mass.png`. Accessed: 23/10/2016.

[15] E2m, "Meson nonet." `https://commons.wikimedia.org/wiki/File:Meson_nonet_-_spin_0.svg`. Accessed: 23/10/2016.

[16] R. Jaffe and K. Johnson, "Unconventional states of confined quarks and gluons," *Physics Letters B*, vol. 60, no. 2, pp. 201–204, 1976.

[17] R. Jaffe, "Multiquark hadrons. i. phenomenology of q 2 q 2 mesons," *Physical Review D*, vol. 15, no. 1, p. 267, 1977.

[18] T. Barnes and F. E. Close, "A light exotic qqg hermaphrodite meson?," *Physics Letters B*, vol. 116, no. 5, pp. 365–368, 1982.

[19] N. Isgur and J. Paton, "Flux-tube model for hadrons in qcd," *Physical Review D*, vol. 31, no. 11, p. 2910, 1985.

[20] N. Isgur, R. Kokoski, and J. Paton, "Gluonic excitations of mesons: Why they are missing and where to find them," *Physical Review Letters*, vol. 54, no. 9, p. 869, 1985.

[21] P. Guo, A. P. Szczepaniak, G. Galata, A. Vassallo, and E. Santopinto, "Heavy quarkonium hybrids from coulomb gauge qcd," *Physical Review D*, vol. 78, no. 5, p. 056003, 2008.

[22] V. D. Burkert, "Meson production and baryon resonances at clas," *International Journal of Modern Physics A*, vol. 26, no. 03n04, pp. 493–498, 2011.

[23] J. J. Dudek, R. G. Edwards, M. J. Peardon, D. G. Richards, C. E. Thomas, H. S. Collaboration, *et al.*, "Highly excited and exotic meson spectrum from dynamical lattice qcd," *Physical review letters*, vol. 103, no. 26, p. 262001, 2009.

[24] J. J. Dudek, R. G. Edwards, M. J. Peardon, D. G. Richards, C. E. Thomas, H. S. Collaboration, *et al.*, "Toward the excited meson spectrum of dynamical qcd," *Physical Review D*, vol. 82, no. 3, p. 034508, 2010.

[25] J. J. Dudek, R. G. Edwards, K. Orginos, and D. G. Richards, "Lattice qcd and the jefferson lab program," in *Journal of Physics: Conference Series*, vol. 299, p. 012007, IOP Publishing, 2011.

[26] A. P. Szczepaniak and M. Swat, "Role of photoproduction in exotic meson searches," *Physics Letters B*, vol. 516, no. 1, pp. 72–76, 2001.

[27] R. Aaij, B. Adeva, M. Adinolfi, A. Affolder, Z. Ajaltouni, S. Akar, J. Albrecht, F. Alessio, M. Alexander, S. Ali, *et al.*, "Observation of j/ψ p resonances consistent with pentaquark states in λ b 0 j/ψ k- p decays," *Physical review letters*, vol. 115, no. 7, p. 072001, 2015.

[28] R. Aaij, B. Adeva, M. Adinolfi, Z. Ajaltouni, S. Akar, J. Albrecht, F. Alessio, M. Alexander, S. Ali, G. Alkhazov, *et al.*, "Observation of j/$\psi\phi$ structures consistent with exotic states from amplitude analysis of $b^+ \to j/\psi\phi k^+$ decays," *arXiv preprint arXiv:1606.07895*, 2016.

[29] D. Diakonov, "Foundations of the constitutent quark model," *Progress in Particle and Nuclear Physics*, vol. 36, pp. 1–17, 1996.

[30] D. Lichtenberg, L. Tassie, and P. Keleman, "Quark-diquark model of baryons and su (6)," *Physical Review*, vol. 167, no. 5, p. 1535, 1968.

[31] E. Santopinto and J. Ferretti, "Strange and nonstrange baryon spectra in the relativistic interacting quark-diquark model with a gürsey and radicati-inspired exchange interaction," *Physical Review C*, vol. 92, no. 2, p. 025202, 2015.

[32] T. DeGrand, Z. Liu, and S. Schaefer, "Diquark effects in light baryon correlators from lattice qcd," *Physical Review D*, vol. 77, no. 3, p. 034505, 2008.

[33] C. Barrel, "Baryon spectroscopy." `https://www1.cb.uni-bonn.de/index.php?id=3`. Accessed: 16/05/2017.

[34] P. Hasenfratz and J. Kuti, "The quark bag model," *Physics Reports*, vol. 40, no. 2, pp. 75–179, 1978.

[35] K. Johnson, "The mit bag model," *Acta Physica Polonica. Series B*, vol. 6, no. 6, pp. 865–892, 1975.

[36] R. Goldflam and L. Wilets, "Soliton bag model," *Physical Review D*, vol. 25, no. 7, p. 1951, 1982.

[37] A. W. Thomas, S. Theberge, and G. A. Miller, "Cloudy bag model of the nucleon," *Physical Review D*, vol. 24, no. 1, p. 216, 1981.

[38] T. DeGrand, R. Jaffe, K. Johnson, and J. Kiskis, "Masses and other parameters of the light hadrons," *Physical Review D*, vol. 12, no. 7, p. 2060, 1975.

[39] R. Gupta, "Introduction to lattice qcd," *arXiv preprint hep-lat/9807028*, 1998.

[40] S. Dürr, Z. Fodor, J. Frison, C. Hoelbling, R. Hoffmann, S. Katz, S. Krieg, T. Kurth, L. Lellouch, T. Lippert, *et al.*, "Ab initio determination of light hadron masses," *Science*, vol. 322, no. 5905, pp. 1224–1227, 2008.

[41] C. W. Leemann, D. R. Douglas, and G. A. Krafft, "The continuous electron beam accelerator facility: Cebaf at the jefferson laboratory," *Annual Review of Nuclear and Particle Science*, vol. 51, no. 1, pp. 413–450, 2001.

[42] J. Alcorn, B. Anderson, K. Aniol, J. Annand, L. Auerbach, J. Arrington, T. Averett, F. Baker, M. Baylac, E. Beise, *et al.*, "Basic instrumentation for hall a at jefferson lab," *Nuclear Instruments and Methods in Physics Research Section A: Accelerators, Spectrometers, Detectors and Associated Equipment*, vol. 522, no. 3, pp. 294–346, 2004.

[43] B. A. Mecking, G. Adams, S. Ahmad, E. Anciant, M. Anghinolfi, B. Asavapibhop, G. Asryan, G. Audit, T. Auger, H. Avakian, *et al.*, "The cebaf large acceptance spectrometer (clas)," *Nuclear Instruments and Methods in Physics Research Section A: Accelerators, Spectrometers, Detectors and Associated Equipment*, vol. 503, no. 3, pp. 513–553, 2003.

[44] T. J. L. H. C. Collaboration, Y. Liang, V. Tvaskis, M. Christy, A. Ahmidouch, C. Armstrong, J. Arrington, R. Asaturyan, S. Avery, O. Baker, *et al.*, "Measurement of r= sigma_l/sigma_t and the separated longitudinal and transverse structure functions in the nucleon resonance region," *arXiv preprint nucl-ex/0410027*, 2004.

[45] D. Androic, D. Armstrong, A. Asaturyan, T. Averett, J. Balewski, J. Beaufait, R. Beminiwattha, J. Benesch, F. Benmokhtar, J. Birchall, *et al.*, "First determination of the weak charge of the proton," *Physical review letters*, vol. 111, no. 14, p. 141803, 2013.

[46] Y. Qiang, S. Collaboration, *et al.*, "Detector development for jefferson labs 12gev upgrade," *Nuclear Instruments and Methods in Physics Research Section B: Beam Interactions with Materials and Atoms*, vol. 350, pp. 71–76, 2015.

[47] JLab, "Jlab picture exchange." `http://www1.jlab.org/ul/jpix`.

[48] M. Mestayer, D. Carman, B. Asavapibhop, F. Barbosa, P. Bonneau, S. Christo, G. Dodge, T. Dooling, W. Duncan, S. Dytman, *et al.*, "The clas drift chamber system," *Nuclear Instruments and Methods in Physics Research Section A: Accelerators, Spectrometers, Detectors and Associated Equipment*, vol. 449, no. 1, pp. 81–111, 2000.

[49] G. Adams, V. Burkert, R. Carl, T. Carstens, V. Frolov, L. Houghtlin, G. Jacobs, M. Kossov, M. Klusman, B. Kross, *et al.*, "The clas cherenkov detector," *Nuclear Instruments and Methods in Physics Research Section A: Accelerators, Spectrometers, Detectors and Associated Equipment*, vol. 465, no. 2, pp. 414–427, 2001.

[50] E. Smith, T. Carstens, J. Distelbrink, M. Eckhause, H. Egiyan, L. Elouadrhiri, J. Ficenec, M. Guidal, A. Hancock, F. Hersman, *et al.*, "The time-of-flight system for clas," *Nuclear Instruments and Methods in Physics*

Research Section A: Accelerators, Spectrometers, Detectors and Associated Equipment, vol. 432, no. 2, pp. 265–298, 1999.

[51] M. Amarian, G. Asryan, K. Beard, W. Brooks, V. Burkert, T. Carstens, A. Coleman, R. Demirchyan, Y. Efremenko, H. Egiyan, *et al.*, "The clas forward electromagnetic calorimeter," *Nuclear Instruments and Methods in Physics Research Section A: Accelerators, Spectrometers, Detectors and Associated Equipment*, vol. 460, no. 2, pp. 239–265, 2001.

[52] M. Anghinolfi, M. Battaglieri, P. Corvisiero, R. De Vita, E. Golovach, A. Longhi, V. Mokeev, G. Ricco, M. Ripani, V. Sapunenko, *et al.*, "Response to cosmic rays of the large-angle electromagnetic shower calorimeter of the clas detector," *Nuclear Instruments and Methods in Physics Research Section A: Accelerators, Spectrometers, Detectors and Associated Equipment*, vol. 447, no. 3, pp. 424–431, 2000.

[53] S. Taylor, S. Ahmad, J. Distelbrink, G. Mutchler, E. Smith, and T. Smith, "The clas start counter," *Nuclear Instruments and Methods in Physics Research Section A: Accelerators, Spectrometers, Detectors and Associated Equipment*, vol. 462, no. 3, pp. 484–493, 2001.

[54] D. Sober, H. Crannell, A. Longhi, S. Matthews, J. O'Brien, B. Berman, W. Briscoe, P. L. Cole, J. Connelly, W. Dodge, *et al.*, "The bremsstrahlung tagged photon beam in hall b at jlab," *Nuclear Instruments and Methods in Physics Research Section A: Accelerators, Spectrometers, Detectors and Associated Equipment*, vol. 440, no. 2, pp. 263–284, 2000.

[55] J. O'Meara, J. Alcorn, P. Brindza, M.-S. Chew, G. Doolittle, M. Fowler, B. Mecking, C. Riggs, D. Tilles, and W. Tuzel, "A superconducting toroidal magnet for the cebaf large acceptance spectrometer," *IEEE Transactions on Magnetics*, vol. 25, no. 2, pp. 1902–1905, 1989.

[56] A. J. Street, J. S. Ross, S. M. Harrison, D. M. Jenkins, M. F. Mason, R. J. Riggs, K. D. Smith, J. M. Wiatrzyk, J. E. O'Meara, W. Tuzel, *et al.*, "Final site assembly and testing of the superconducting toroidal magnet for the cebaf large acceptance spectrometer (clas)," tech. rep., Thomas Jefferson National Accelerator Facility, 1996.

[57] D. Carman, S. Dytman, R. Magahiz, M. Mestayer, R. Miskimen, J. Mueller, R. Schumacher, D. Tedeschi, R. Thompson, and G. Wilkin, "The region one drift chamber for the clas spectrometer," *Nuclear Instruments and Methods in Physics Research Section A: Accelerators, Spectrometers, Detectors and Associated Equipment*, vol. 419, no. 2, pp. 315–319, 1998.

[58] L. Qin, B. Raue, G. Dodge, C. Hyde-Wright, A. Klein, S. Kuhn, T. Pyron, K. Vansyoc, L. Weinstein, and J. Yun, "Prototype studies and design considerations for the clas region 2 drift chambers," *Nuclear Instruments and Methods in Physics Research Section A: Accelerators, Spectrometers, Detectors and Associated Equipment*, vol. 411, no. 2-3, pp. 265–274, 1998.

[59] V. D. Burkert, "Clas12 and its initial science program at the jefferson lab upgrade," *arXiv preprint arXiv:0810.4718*, 2008.

[60] M. Contalbrigo, E. Cisbani, and P. Rossi, "The clas12 large area rich detector," *Nuclear Instruments and Methods in Physics Research Section A: Accelerators, Spectrometers, Detectors and Associated Equipment*, vol. 639, no. 1, pp. 302–306, 2011.

[61] F. T. Collaboration, "Clas12 forward tagger technical design report, v2.0," tech. rep., Jefferson Laboratory, December 2012.

[62] R. D. Vita, D. Armstrong, V. Burkert, J.-P. Chen, W. Detmold, J. Dudek, W. Melnitchouk, and D. Richards, "Meson spectroscopy at clas and clas12: the present and the future," in *AIP Conference Proceedings*, vol. 1374, pp. 55–60, AIP, 2011.

[63] S. Chekanov, M. Derrick, D. Krakauer, S. Magill, B. Musgrave, A. Pellegrino, J. Repond, R. Yoshida, M. Mattingly, P. Antonioli, *et al.*, "Measurement of the photon–proton total cross section at a center-of-mass energy of 209 gev at hera," *Nuclear Physics B*, vol. 627, no. 1, pp. 3–28, 2002.

[64] E. Ageev, V. Y. Alexakhin, Y. Alexandrov, G. Alexeev, A. Amoroso, B. Badelek, F. Balestra, J. Ball, G. Baum, Y. Bedfer, *et al.*, "Gluon polarization in the nucleon from quasi-real photoproduction of high-pt hadron pairs," *Physics Letters B*, vol. 633, no. 1, pp. 25–32, 2006.

[65] D. Zhou, A. collaboration, *et al.*, "Phos, the alice-photon spectrometer," *Journal of Physics G: Nuclear and Particle Physics*, vol. 34, no. 8, p. S719, 2007.

[66] W. Erni, I. Keshelashvili, B. Krusche, M. Steinacher, Y. Heng, Z. Liu, H. Liu, X. Shen, O. Wang, H. Xu, *et al.*, "Technical design report for panda electromagnetic calorimeter (emc)," *arXiv preprint arXiv:0810.1216*, 2008.

[67] S. Stepanyan *et al.*, "Clas note 2009-019; s. stepanyan et. al," in *2008 IEEE nuclear Science Symposium and Medical imaging Conference*, 2008.

[68] G. Charpak, J. Derre, Y. Giomataris, and P. Rebourgeard, "Micromegas, a multipurpose gaseous detector," *Nuclear Instruments and Methods in Physics Research Section A: Accelerators, Spectrometers, Detectors and Associated Equipment*, vol. 478, no. 1, pp. 26–36, 2002.

[69] Eljen, "Ej-204 plastic scintillator." `https://www.southernscientific.co.uk/data/file/7/6/EJ204%20data%20sheet.1438855729.pdf`. Accessed: 30/05/2017.

[70] Kuraray, "Kuraray wavelength shifting fibres." `http://kuraraypsf.jp/psf/ws.html`. Accessed: 21/05/2017.

[71] Hamamatsu, "Mppcs for precision measurement s13360 series." http://www.hamamatsu.com/resources/pdf/ssd/s13360_series_kapd1052e.pdf. Accessed: 30/05/2017.

[72] Kuraray, "Kuraray clear fibres." http://kuraraypsf.jp/psf/cf.html. Accessed: 21/05/2017.

[73] A. Dyshkant, D. Beznosko, G. Blazey, E. Fisk, E. Hahn, V. Rykalin, M. Wayne, and V. Zutshi, "Quality control studies of wavelength shifting fibers for a scintillator-based tail catcher muon tracker for linear collider prototype detector," *IEEE transactions on nuclear science*, vol. 53, no. 6, pp. 3944–3948, 2006.

[74] A. Artikov, J. Budagov, I. Chirikov-Zorin, D. Chokheli, V. Kolomoets, M. Lyablin, O. Pukhov, A. Sissakian, G. Bellettini, A. Menzione, *et al.*, "New-generation large-area muon scintillation counters with wavelength shifter fiber readout for cdf ii," *Physics of Particles and Nuclei Letters*, vol. 3, no. 3, pp. 188–200, 2006.

[75] P. Degtiarenko, A. Fassò, G. Kharashvili, and A. Somov, "Calculation of radiation damage to silicon photomultipliers in gluex experiment," 2011.

[76] S. Barsuk, I. Korolko, S. Malyshev, V. Y. Rusinov, V. Kirichenko, E. Tarkovski, and A. Golutvin, "Radiation damage of lhcb electromagnetic calorimeter," tech. rep., 2000.

[77] S. Han, L. Hu, N. Liu, H. Mao, H. Shi, Y. Tan, G. Wang, C. Zhang, G. Zhang, L. Zhang, *et al.*, "Radiation hardness tests of scintillating tile/wls fiber calorimeter modules," *Nuclear Instruments and Methods in Physics Research Section A: Accelerators, Spectrometers, Detectors and Associated Equipment*, vol. 365, no. 2-3, pp. 337–351, 1995.

[78] G. Mazzitelli, A. Ghigo, F. Sannibale, P. Valente, and G. Vignola, "Commissioning of the daϕne beam test facility," *Nuclear Instruments and Methods in Physics Research Section A: Accelerators, Spectrometers, Detectors and Associated Equipment*, vol. 515, no. 3, pp. 524–542, 2003.

[79] M. Janecek, "Reflectivity spectra for commonly used reflectors," *IEEE Transactions on Nuclear Science*, vol. 59, no. 3, pp. 490–497, 2012.

[80] M. Janecek and W. W. Moses, "Optical reflectance measurements for commonly used reflectors," *IEEE Transactions on Nuclear Science*, vol. 55, no. 4, pp. 2432–2437, 2008.

[81] SaintGobain, "Bc-620 reflector paint for plastic scintillators." http://www.crystals.saint-gobain.com/sites/imdf.crystals.com/files/documents/sgc-bc620-data-sheet_69725.pdf. Accessed: 31/05/2017.

[82] C. Joram and T. Schneider, "Mirroring of fibre ends for the lhcb scifi project," tech. rep., 2014.

[83] AdvanSiD, "Introduction to sipms," September 2014. Accessed: 15-09-2016.

[84] A. Gola, A. Tarolli, and C. Piemonte, "Sipm cross-talk amplification due to scintillator crystal: effects on timing performance," in *Nuclear Science Symposium and Medical Imaging Conference (NSS/MIC), 2012 IEEE*, pp. 421–423, IEEE, 2012.

[85] F. Barbosa, J. McKisson, J. McKisson, Y. Qiang, E. Smith, C. Zorn, G. Collaboration, *et al.*, "Silicon photomultiplier characterization for the gluex barrel calorimeter," *Nuclear Instruments and Methods in Physics Research Section A: Accelerators, Spectrometers, Detectors and Associated Equipment*, vol. 695, pp. 100–104, 2012.

[86] P. Lightfoot, G. J. Barker, K. Mavrokoridis, Y. Ramachers, and N. Spooner, "Characterisation of a silicon photomultiplier device for applications in liquid argon based neutrino physics and dark matter searches," *Journal of Instrumentation*, vol. 3, no. 10, p. P10001, 2008.

[87] J. Fleming, *First Measurement of the E Double-polarisation Observable for $\gamma n \rightarrow K^{+}\Sigma$ with CLAS and a New Forward Tagging Hodoscope for CLAS12.* PhD thesis, The University of Edinburgh, 2016.

[88] E. Gallas and J. Li, "Polishing optical fibers for the d0 icd in run ii," tech. rep., FNAL-TM-2062, 1998.

[89] Epotek, "Epotek 310-2 data sheet." `http://www.epotek.com/site/administrator/components/com_products/assets/files/Style_Uploads/301-2RevXII.pdf`. Accessed: 31/05/2017.

[90] P. Hanlet, M. Marcus, and E. Gallas, "Comparison of fiber polishing techniques," 1999.

[91] MySearch, "Mandelstam variables." `http://www.mysearch.org.uk/website1/html/610.Mandelstam.html`. Accessed: 31/05/2017.

[92] C. Defoix, L. Dobrzynski, P. Espigat, A. Nascimente, J. O'Neall, P. Rivet, and J. Siaud, "Evidence for an ω $\pi+$ π- decay mode of the a 2 via an ω $\pi\pm$resonance at 1040 mev and for an ω $\pi+$ π- effect near 1400 mev," *Physics Letters B*, vol. 43, no. 2, pp. 141–145, 1973.

[93] V. Chaloupka, L. Dobrzynski, A. Ferrando, M. J. Losty, L. Montanet, E. Paul, D. Yaffe, and A. Zieminski, "A measurement of the branching ratios of the a 2- meson produced in 3.9 gev/cπ- interactions," *Physics Letters B*, vol. 44, no. 2, pp. 211–216, 1973.

[94] U. Karshon, G. Mikenberg, S. Pitluck, Y. Eisenberg, E. Ronat, A. Shapira, and G. Yekutieli, "Structure in the ω π π system at the a 2 mass region," *Physical Review Letters*, vol. 32, no. 15, p. 852, 1974.

[95] J. Diaz, F. DiBianca, W. Fickinger, J. Malko, D. Robinson, C. Sullivan, J. Anderson, A. Engler, R. Kraemer, S. Toaff, *et al.*, "Evidence for the ω π π decay modes of the a 2 and ω (1675)," *Physical Review Letters*, vol. 32, no. 5, p. 260, 1974.

[96] M. Alekseev, V. Y. Alexakhin, Y. Alexandrov, G. Alexeev, A. Amoroso, A. Austregesilo, B. Badełek, F. Balestra, J. Ball, J. Barth, *et al.*, "Observation of a j pc= 1-+ exotic resonance in diffractive dissociation of 190 gev/c π- into π- π- π+," *Physical review letters*, vol. 104, no. 24, p. 241803, 2010.

[97] V. Aulchenko, M. Achasov, A. Y. Barnyakov, K. Beloborodov, A. Berdyugin, A. Bogdanchikov, A. Botov, A. Vasilev, V. Golubev, T. Dimova, *et al.*, "Study of the e+ e– π+ π–π0 process in the energy range 1.05–2.00 gev," *Journal of Experimental and Theoretical Physics*, vol. 121, no. 1, pp. 27–34, 2015.

[98] A. Abele, S. Bischoff, P. Blüm, N. Djaoshvili, D. Engelhardt, A. Herbstrith, C. Holtzhaußen, M. Tischhäuser, J. Adomeit, B. Kämmle, *et al.*, "p^- p annihilation at rest into k l k$\pm\pi$," *Physical Review D*, vol. 57, no. 7, p. 3860, 1998.

[99] M. Lu, G. Adams, T. Adams, Z. Bar-Yam, J. Bishop, V. Bodyagin, D. Brown, N. Cason, S. Chung, J. Cummings, *et al.*, "Exotic meson decay to ω π 0 π-," *Physical review letters*, vol. 94, no. 3, p. 032002, 2005.

[100] D. Amelin, E. Berdnikov, S. Bityukov, G. Borisov, V. Dorofeev, R. Dzhelyadin, Y. Gouz, I. Kachaev, A. Karyukhin, Y. A. Khokhlov, *et al.*, "Partial-wave analysis of the reaction π- p π+ π- π 0 n at," *Zeitschrift für Physik C Particles and Fields*, vol. 70, no. 1, pp. 71–75, 1996.

[101] C. Shen, C. Yuan, P. Wang, X. Wang, I. Adachi, H. Aihara, K. Arinstein, V. Aulchenko, A. Bakich, E. Barberio, *et al.*, "Observation of the ϕ (1680) and the y (2175) in e+ e- ϕ π+ π-," *Physical Review D*, vol. 80, no. 3, p. 031101, 2009.

[102] M. B. et al., "Spectroscopy of excited baryons with clas: Search for the ground and first excited states." CLAS Analysis Proposal PR04-021.

[103] M. Williams, *Measurement of Differential Cross Sections and Spin Density Matrix Elements along with a Partial Wave Analysis for $\gamma p \to p\omega$ using CLAS at Jefferson Lab.* PhD thesis, Carnegie Mellon University, 2007.

[104] R. D. V. M. Ungaro and L. Elouadrhiri, "g11 data processing," Tech. Rep. CLAS Note 2005-014, Jefferson Laboratory, 2005.

[105] E. Pasyuk, "Energy loss corrections for charged particles in clas," Tech. Rep. CLAS Note 2007-16, Jefferson Laboratory, 2007.

[106] D. A. M. Williams and C. Meyer., "Determining momentum and energy corrections for g1c using kinematic fitting.," Tech. Rep. CLAS Note 2004-17, Jefferson Laboratory, 2004.

[107] D. A. et al., "The tagger energy scale: Interpreting the cmu kinematic fitting results.," Tech. Rep. CLAS Note 2004-19, Jefferson Laboratory, 2004.

[108] E. Santopinto, M. Battaglieri, A. Celentano, R. De Vita, S. Fegan, V. Mathieu, A. Szczepaniak, A. Filippi, A. D'Angelo, A. Rizzo, *et al.*, "Haspect: Hadron spectroscopy center," in *Journal of Physics: Conference Series*, vol. 527, IOP Publishing, 2014.

[109] R. Brun and F. Rademakers, "Rootan object oriented data analysis framework," *Nuclear Instruments and Methods in Physics Research Section A: Accelerators, Spectrometers, Detectors and Associated Equipment*, vol. 389, no. 1-2, pp. 81–86, 1997.

[110] M. Ballintijn, R. Brun, F. Rademakers, and G. Roland, "The proof distributed parallel analysis framework based on root," *arXiv preprint physics/0306110*, 2003.

[111] L. Moneta, K. Belasco, K. Cranmer, S. Kreiss, A. Lazzaro, D. Piparo, G. Schott, W. Verkerke, and M. Wolf, "The roostats project," *arXiv preprint arXiv:1009.1003*, 2010.

[112] L. Zana, "Edgen event generator." `http://www.ph.ed.ac.uk/nuclear-physics/research-activities/nuclear-and-hadron-physics/edgen-event-generator`. Accessed: 31/05/2017.

[113] R. Brun, F. Bruyant, M. Maire, A. McPherson, and P. Zanarini, "Geant3 users guide," tech. rep., CERN DD/EE/84-1, 1987.

[114] E. Wolin, "Gsim user's guide version 1.1." `https://www.jlab.org/Hall-B/document/gsim/userguide.html`. Accessed: 31/05/2017.

[115] M. Pivk and F. R. Le Diberder, ": A statistical tool to unfold data distributions," *Nuclear Instruments and Methods in Physics Research Section A: Accelerators, Spectrometers, Detectors and Associated Equipment*, vol. 555, no. 1, pp. 356–369, 2005.